

**FIRST PRINCIPLES STUDY OF ELECTRONIC AND  
VIBRATIONAL PROPERTIES OF WIDE BAND GAP  
OXIDE AND NITRIDE SEMICONDUCTORS**

by

**AMOL RATNAPARKHE**

Submitted in partial fulfillment of the requirements

for the degree of Doctor of Philosophy

Department of Physics

CASE WESTERN RESERVE UNIVERSITY

May, 2021

**CASE WESTERN RESERVE UNIVERSITY**  
**SCHOOL OF GRADUATE STUDIES**

We hereby approve the dissertation of

**Amol Ratnaparkhe**

candidate for the degree of **Doctor of Philosophy\***.

Committee Chair

**Dr. Walter R. L. Lambrecht**

Committee Member

**Dr. Harsh Mathur**

Committee Member

**Dr. Kathleen Kash**

Committee Member

**Dr. Alp Sehirlioglu**

Date of Defense

**April 06, 2021**

\*We also certify that written approval has been obtained  
for any proprietary material contained therein.

# Contents

List of Tables	iv
List of Figures	vii
Acknowledgments	xiii
Abstract	xv
<b>1 Introduction</b>	<b>1</b>
1.1 $\beta$ -Ga <sub>2</sub> O <sub>3</sub> and (Al <sub>x</sub> Ga <sub>1-x</sub> ) <sub>2</sub> O <sub>3</sub> alloys . . . . .	1
1.2 II-IV nitride: ZnGeGa <sub>2</sub> N <sub>4</sub> . . . . .	7
1.3 Transition metal oxide: MoO <sub>3</sub> . . . . .	11
<b>2 Computational Methods</b>	<b>12</b>
2.1 Density Functional Theory . . . . .	12
2.1.1 FP-LMTO Method . . . . .	16
2.2 QSGW Method . . . . .	19
2.3 Density Functional Perturbation Theory . . . . .	24
<b>3 QSGW study of <math>\beta</math>-Ga<sub>2</sub>O<sub>3</sub></b>	<b>29</b>
3.1 Introduction . . . . .	29
3.2 Computational Method . . . . .	30
3.3 Results . . . . .	32

3.3.1	Lattice polarization analysis . . . . .	34
3.3.2	Absorption onset . . . . .	35
3.4	Conclusions . . . . .	38
<b>4</b>	<b>QSGW study of <math>(\text{Al}_x\text{Ga}_{1-x})_2\text{O}_3</math> alloys</b>	<b>39</b>
4.1	Introduction . . . . .	39
4.2	Computational method . . . . .	40
4.3	Modeling of disorder . . . . .	41
4.4	Results . . . . .	42
4.4.1	Lattice constants . . . . .	42
4.4.2	Energy of formation . . . . .	43
4.4.3	Band gaps . . . . .	48
<b>5</b>	<b>Vibrational properties of <math>\text{ZnGeGa}_2\text{N}_4</math></b>	<b>53</b>
5.1	Introduction . . . . .	53
5.2	Computational method . . . . .	54
5.3	Results . . . . .	55
5.3.1	Group theoretical analysis and crystal structure . . . . .	55
5.3.2	Phonon frequencies and related results . . . . .	58
5.3.3	Infrared spectra . . . . .	59
5.3.4	Raman spectra . . . . .	73
5.3.5	Phonon dispersion and density of states . . . . .	81
5.4	Conclusions . . . . .	84
<b>6</b>	<b>Vibrational properties of <math>\alpha\text{-MoO}_3</math></b>	<b>86</b>
6.1	Introduction . . . . .	86
6.2	Computational Method . . . . .	86
6.3	Results . . . . .	87
6.3.1	Crystal structure and group theoretical analysis . . . . .	87

---

6.3.2	Phonon frequencies and related results. . . . .	90
6.3.3	Infrared spectra and associated quantities. . . . .	93
6.3.4	Raman spectra . . . . .	99
6.4	Conclusions . . . . .	104
<b>7</b>	<b>Conclusions</b>	<b>106</b>
<b>A</b>	<b>Appendix</b>	<b>109</b>
A.1	Supplemental material for $\text{ZnGeGa}_2\text{N}_4$ . . . . .	109

# List of Tables

3.1	Band gaps in $\beta$ -Ga <sub>2</sub> O <sub>3</sub> in different approximations. . . . .	31
3.2	Character table of $C_{2h}$ . . . . .	33
3.3	Energy levels at $\Gamma$ near the VBM and CBM in 0.8 $\Sigma$ +LPC approximation, and their irreducible representation. . . . .	37
4.1	Energy of formation per formula unit and band gaps in different configurations as function of concentration in (Al <sub>x</sub> Ga <sub>1-x</sub> ) <sub>2</sub> O <sub>3</sub> alloys. In the monoclinic structure the configuration is specified by which atoms go in the octahedral (o) and tetrahedral (t) sites In the corundum structure, the sites are all octahedral but we can still distinguish the corner (c) and middle (m) sites in the structure. . . . .	46
5.1	Lattice constant (in Å) and reduced coordinates. The Wyckoff positions are indicated with each atom type. . . . .	56
5.2	Character table of $C_{2v}$ . . . . .	56
5.3	Phonon frequencies in $Pmn2_1$ ZnGeGa <sub>2</sub> N <sub>4</sub> in cm <sup>-1</sup> labeled by irreducible representation in the column heading. . . . .	59
5.4	Born effective charge tensor elements ( in units $ e $ ) for the atom of each type given in Table 5.1, indicated by the column. These local tensor elements transform between symmetry related atoms as indicated by the irreducible representation label. . . . .	60

5.5	Oscillator strength tensor elements for each mode of a given symmetry in order of increasing frequency and in atomic units, $e^2/m_e$ . For each irreducible representation given in parenthesis, only the indicated diagonal component of $S_{n,\alpha\alpha}$ defined in Eq. 5.4, is non-zero as indicated in the column heading. . . . .	62
5.6	High-frequency and static dielectric tensor components. . . . .	63
5.7	The indices of refraction. . . . .	63
5.8	Raman tensor components. . . . .	74
6.1	Reduced coordinates and lattice constants in $\alpha$ -MoO <sub>3</sub> in the $Pnma$ spacegroup. . . . .	89
6.2	Character table of $D_{2h}$ . . . . .	90
6.3	Phonon frequencies of $\alpha$ -MoO <sub>3</sub> in $\text{cm}^{-1}$ . Experimental values from Seguin <i>et al.</i> [28]. $\sigma$ is the error of the calc. compared to expt. in %	94
6.4	Born effective charge tensor elements for the atoms listed in Table 6.1. By symmetry all $Z_{xy}^*$ , $Z_{yx}^*$ , $Z_{xz}^*$ , $Z_{zx}^*$ are zero. . . . .	95
6.5	Oscillator strength tensors. . . . .	96
6.6	High-frequency and static dielectric tensor components. . . . .	97
6.7	The indices of refraction. . . . .	97
6.8	Raman tensor components. . . . .	101

---

A.1	Reduced coordinates of atoms in the cell and the symmetry elements linking them to the first atom of each type. Note that $2_{1z}$ is a two fold screw axis along $z$ with translation in the $z$ direction by $c/2$ and placed at $x = 0$ $y = -b/3$ and is thus accompanied by an additional translation of $y = b/3$ , $m_x$ is an ordinary reflection but with translation $x = a/2$ because it is placed at $x = a/4$ , $n_y$ is a glide mirror plane with translations $x = a/2$ , $z = c/2$ and an additional $y = b/3$ because of its placement at $y = b/6$ . . . . .	110
A.2	Sign changes of displacements between symmetry related atoms 1-4 for Wyckoff $4a$ and 1-2 for Wyckoff $2b$ atom ordered as in Table A.1. . .	111

# List of Figures

1.1	Breakdown field vs Bandgap [1] . . . . .	3
1.2	$\beta$ -Ga <sub>2</sub> O <sub>3</sub> primitive unit cell . . . . .	3
1.3	$\alpha$ -Al <sub>2</sub> O <sub>3</sub> primitive unit cell . . . . .	6
1.4	Octet-rule preserving ZnGeGa <sub>2</sub> N <sub>4</sub> structures and their relation to ZnGeN <sub>2</sub> with (a) <i>Pbn</i> 2 <sub>1</sub> , (b) <i>Pmc</i> 2 <sub>1</sub> , (c) <i>Pmn</i> 2 <sub>1</sub> , and (d) <i>P1n</i> 1. Image taken from [25]. . . . .	10
1.5	Non-octet-rule-preserving ZnGeGa <sub>2</sub> N <sub>4</sub> structures: (a) [100] <sub>1/2</sub> and (b) [001] <sub>1/2</sub> superlattices, based on the <i>Pbn</i> 21 ZnGeN <sub>2</sub> structure. Image taken from [25]. . . . .	10
2.1	<i>QSGW</i> (blue) and <i>LDA</i> (red) optical dielectric constant $\epsilon_\infty$ compared to experiment[55]. . . . .	23
3.1	Band structure of $\beta$ -Ga <sub>2</sub> O <sub>3</sub> in the 0.8 $\Sigma$ <i>QSGW</i> approximation plus lattice polarization correction. The <b>k</b> -point labels are named as in Ref. [10]. . . . .	32
3.2	Calculated imaginary part of the optical dielectric function, for different polarizations in $\beta$ -Ga <sub>2</sub> O <sub>3</sub> . The <i>z</i> direction is perpendicular to the <i>ab</i> -plane, close to but not exactly along <b>c</b> because <b>c</b> makes an angle $\beta = 103.82^\circ$ with the <b>a</b> axis. . . . .	36

4.1	Pseudocubic lattice parameter of $(\text{Al}_x\text{Ga}_{1-x})_2\text{O}_3$ as function of $x$ for both crystal structures. . . . .	43
4.2	Energy of formation per formula unit for the alloys in the two structures across compositions. Solid data points show Al atoms occupying the octahedral positions while the higher energy hollow data points show the energies for configurations with increasing number of Al occupying tetrahedral sites. The $\times$ and $*$ show the average formation energies assuming random probability of the different configurations. The dotted lines show the corresponding interpolation while the solid lines assume the minimum energy configuration at each composition. . . . .	44
4.3	Direct band gap for the alloys as function of composition for each of the crystal structures. The solid symbols correspond to the lowest energy structure. The lines are a fit to these points with the parabolic equation defining the bowing coefficient. The open symbols to different configurations as detailed in Table 4.1. . . . .	48
4.4	Brillouin zones representing the high-symmetry points for $(\text{Al}_x\text{Ga}_{1-x})_2\text{O}_3$ in (a) monoclinic( $\beta$ -phase) [10], and (b) rhombohedral( $\alpha$ -phase) “© IOP Publishing. Reproduced with permission. All rights reserved.” [84]. . . . .	49
4.5	Band structures of $(\text{Al}_x\text{Ga}_{1-x})_2\text{O}_3$ for 0% Al concentration in: (a) $\alpha$ -phase and (b) $\beta$ -phase. . . . .	49
4.6	Band structures of $(\text{Al}_x\text{Ga}_{1-x})_2\text{O}_3$ for 25% Al concentration in: (a) $\alpha$ -phase and (b) $\beta$ -phase. . . . .	50
4.7	Band structures of $(\text{Al}_x\text{Ga}_{1-x})_2\text{O}_3$ for 50% Al concentration in: (a) $\alpha$ -phase and (b) $\beta$ -phase. . . . .	50
4.8	Band structures of $(\text{Al}_x\text{Ga}_{1-x})_2\text{O}_3$ for 75% Al concentration in: (a) $\alpha$ -phase and (b) $\beta$ -phase. . . . .	50

4.9	Band structures of $(\text{Al}_x\text{Ga}_{1-x})_2\text{O}_3$ for 100% Al concentration in: (a) $\alpha$ -phase and (b) $\beta$ -phase. . . . .	51
5.1	Crystal structure of $\text{ZnGeGa}_2\text{N}_4$ in the $Pmn2_1$ spacegroup. . . . .	55
5.2	IR spectra for (a) $a_1$ modes, (b) $b_1$ modes and (c) $b_2$ modes. . . . .	65
5.3	IR spectrum of $b_1$ modes with very small $\Gamma_n = 10^{-5} \text{ cm}^{-1}$ broadening zoomed in on region $500 < \omega < 640 \text{ cm}^{-1}$ focused on modes 6-8. The $y$ -scales have been arbitrary adjusted. . . . .	66
5.4	Raman spectra for $a_{1T}$ modes for $\bar{y}(xx)y$ , $\bar{x}(yy)x$ and $\bar{x}(zz)x$ scattering geometries. . . . .	75
5.5	Raman spectra for $a_{1L}$ modes for $\bar{z}(xx)z$ , $\bar{z}(yy)z$ scattering geometries. . . . .	75
5.6	Raman spectra for $\bar{z}(xy)z$ scattering geometry, giving the $a_2$ modes with $d$ tensor component. . . . .	76
5.7	Raman spectra for $\bar{y}(xz)y$ showing only $b_{1T}$ modes and for $y(xz)x$ scattering geometry, giving $b_{1T} + b_{1L}$ modes. . . . .	76
5.8	Raman spectra for $\bar{x}(yz)x$ showing only $b_{2T}$ modes and for $x(yz)y$ scattering geometry, giving $b_{2T} + b_{2L}$ modes. . . . .	77
5.9	Polar plot for mode $a_{1L}^7$ as function of angle $\phi$ of $\mathbf{e}_i$ with respect to $x$ -axis (crystallographic $\mathbf{a}$ -direction) $\mathbf{e}_o \parallel \mathbf{e}_i$ and $\mathbf{k}_{i/o}$ along $z$ or $\mathbf{c}$ are assumed. . . . .	79
5.10	Polar plot for mode $a_{1L}^{11}$ as function of angle $\phi$ of $\mathbf{e}_i$ with respect to $x$ -axis (crystallographic $\mathbf{a}$ -direction) $\mathbf{e}_o \parallel \mathbf{e}_i$ and $\mathbf{k}_{i/o}$ along $z$ or $\mathbf{c}$ are assumed. . . . .	79
5.11	Polar plot shapes for all $a_{1L}$ modes as function of azimuthal angle (about the $c$ -axis) in the $xy$ -plane with $x$ horizontal, . . . . .	80
5.12	Polar plot shapes for all $a_{1T}$ modes as function of azimuthal angle (about the $b$ -axis) in the $xz$ -plane with $x$ horizontal, . . . . .	80

5.13	Polar plot shapes for $a_{1T}$ modes as function of azimuthal angle (about the $a$ -axis) in the $yz$ -plane with $y$ horizontal. In each case the plots correspond to the modes in order of increasing frequency as given in Table 5.3. Note that the size of each plot relative to the others is arbitrary, only the shape's aspect ratio has meaning. . . . .	80
5.14	Phonon total and atom resolved partial densities of states of $\text{ZnGeGa}_2\text{N}_4$ compared with those for GaN and $\text{ZnGeN}_2$ , the latter two from Materials Project. The dashed lines in the high frequency region for Zn, Ga and Ge were multiplied by a factor 5 for easier viewing of their relative contribution. . . . .	83
5.15	Phonon band structure of $\text{ZnGeGa}_2\text{N}_4$ . $X, Y, Z, U, R, S$ correspond to $\mathbf{b}_1/2, \mathbf{b}_2/2, \mathbf{b}_2/2, (\mathbf{b}_1 + \mathbf{b}_3)/2, (\mathbf{b}_1 + \mathbf{b}_2 + \mathbf{b}_3)/2$ and $(\mathbf{b}_1 + \mathbf{b}_2)/2$ . . . . .	84
6.1	Crystal structure of $\alpha$ - $\text{MoO}_3$ in the $Pm\bar{c}n$ spacegroup setting. Viewed in terms of pyramidal or distorted octahedral units. The small red spheres are O atoms, the larger grey spheres hidden under the polyhedra are the Mo atoms. In the view on the left, the longest Mo-O bond in the vertical direction is omitted from the nearest neighbor polyhedron. . . . .	89
6.2	Eigendisplacement pattern for (a) $B_{1uT}^1$ mode and (b) $B_{2uT}^1$ modes. . . . .	92
6.3	Eigendisplacement pattern for (a) $A_g^1$ mode and (b) $B_{3g}^1$ mode. . . . .	92
6.4	Eigendisplacement pattern for (a) $A_g^7$ mode and (b) $A_g^8$ mode. . . . .	93
6.5	IR and Raman spectra of $o$ - $\text{MoO}_3$ . The Raman spectrum below 500 $\text{cm}^{-1}$ is amplified by a factor of 5. Image taken from [28]. . . . .	98
6.6	IR spectra for $B_{3u}$ modes. . . . .	99
6.7	IR spectra for $B_{2u}$ modes. . . . .	100
6.8	IR spectra for $B_{1u}$ modes. . . . .	100
6.9	Raman spectra for $A_g$ modes. . . . .	102
6.10	Raman spectrum for $B_{1g}$ modes, scattering geometry $z(xy)z$ . . . . .	103

6.11	Raman spectrum for $B_{2g}$ modes, scattering geometry $y(xz)y$ . . . . .	103
6.12	Raman spectrum for $B_{3g}$ modes, scattering geometry $x(yz)x$ . . . . .	104
A.1	$Pmn2_1$ structure of $ZnGeGa_2N_4$ projected along c-axis indicating symmetry elements. Image taken from [25]. . . . .	110
A.2	$a_1^n$ modes eigendisplacements (a) LO (b) TO for $n = 1$ . . . . .	111
A.3	$a_1^n$ modes eigendisplacements (a) LO (b) TO for $n = 2$ . . . . .	111
A.4	$a_1^n$ modes eigendisplacements (a) LO (b) TO for $n = 3$ . . . . .	112
A.5	$a_1^n$ modes eigendisplacements (a) LO (b) TO for $n = 4$ . . . . .	112
A.6	$a_1^n$ modes eigendisplacements (a) LO (b) TO for $n = 5$ . . . . .	112
A.7	$a_1^n$ modes eigendisplacements (a) LO (b) TO for $n = 6$ . . . . .	113
A.8	$a_1^n$ modes eigendisplacements (a) LO (b) TO for $n = 7$ . . . . .	113
A.9	$a_1^n$ modes eigendisplacements (a) LO (b) TO for $n = 8$ . . . . .	113
A.10	$a_1^n$ modes eigendisplacements (a) LO (b) TO for $n = 9$ . . . . .	114
A.11	$a_1^n$ modes eigendisplacements (a) LO (b) TO for $n = 10$ . . . . .	114
A.12	$a_1^n$ modes eigendisplacements (a) LO (b) TO for $n = 11$ . . . . .	114
A.13	$a_1^n$ modes eigendisplacements (a) LO (b) TO for $n = 12$ . . . . .	115
A.14	$a_1^n$ modes eigendisplacements (a) LO (b) TO for $n = 13$ . . . . .	115
A.15	$b_1^n$ modes eigendisplacements (a) LO (b) TO for $n = 1$ . . . . .	116
A.16	$b_1^n$ modes eigendisplacements (a) LO (b) TO for $n = 2$ . . . . .	116
A.17	$b_1^n$ modes eigendisplacements (a) LO (b) TO for $n = 3$ . . . . .	116
A.18	$b_1^n$ modes eigendisplacements (a) LO (b) TO for $n = 4$ . . . . .	117
A.19	$b_1^n$ modes eigendisplacements (a) LO (b) TO for $n = 5$ . . . . .	117
A.20	$b_1^n$ modes eigendisplacements (a) LO (b) TO for $n = 6$ . . . . .	117
A.21	$b_1^n$ modes eigendisplacements (a) LO (b) TO for $n = 7$ . . . . .	118
A.22	$b_1^n$ modes eigendisplacements (a) LO (b) TO for $n = 8$ . . . . .	118
A.23	$b_1^n$ modes eigendisplacements (a) LO (b) TO for $n = 9$ . . . . .	118
A.24	$b_2^n$ modes eigendisplacements (a) LO (b) TO for $n = 1$ . . . . .	119

---

A.25 $b_2^n$ modes eigendisplacements (a) LO (b) TO for $n = 2$ . . . . .	119
A.26 $b_2^n$ modes eigendisplacements (a) LO (b) TO for $n = 3$ . . . . .	119
A.27 $b_2^n$ modes eigendisplacements (a) LO (b) TO for $n = 4$ . . . . .	120
A.28 $b_2^n$ modes eigendisplacements (a) LO (b) TO for $n = 5$ . . . . .	120
A.29 $b_2^n$ modes eigendisplacements (a) LO (b) TO for $n = 6$ . . . . .	120
A.30 $b_2^n$ modes eigendisplacements (a) LO (b) TO for $n = 7$ . . . . .	121
A.31 $b_2^n$ modes eigendisplacements (a) LO (b) TO for $n = 8$ . . . . .	121
A.32 $b_2^n$ modes eigendisplacements (a) LO (b) TO for $n = 9$ . . . . .	121
A.33 $b_2^n$ modes eigendisplacements (a) LO (b) TO for $n = 10$ . . . . .	122
A.34 $b_2^n$ modes eigendisplacements (a) LO (b) TO for $n = 11$ . . . . .	122
A.35 $b_2^n$ modes eigendisplacements (a) LO (b) TO for $n = 12$ . . . . .	122
A.36 $b_2^n$ modes eigendisplacements (a) LO (b) TO for $n = 13$ . . . . .	123
A.37 $a_2^n$ mode eigendisplacements for (a) $n = 1$ (b) $n = 2$ . . . . .	124
A.38 $a_2^n$ mode eigendisplacements for (a) $n = 3$ (b) $n = 4$ . . . . .	124
A.39 $a_2^n$ mode eigendisplacements for (a) $n = 5$ (b) $n = 6$ . . . . .	124
A.40 $a_2^n$ mode eigendisplacements for (a) $n = 7$ (b) $n = 8$ . . . . .	125
A.41 $a_2^n$ mode eigendisplacements (a) $n = 9$ and (b) $n = 10$ . . . . .	125

# Acknowledgments

I would like to begin by expressing my gratitude towards my research advisor, Professor Walter R. L. Lambrecht for accepting me as a student in his group. His experience and guidance certainly has played a key role in my journey. I would also like to thank my group members, in particular, former members Dr. Sai Lyu and Dr. Skachkov for their useful suggestions and countless discussions. I would like to thank the thesis committee members Professor Kathleen Kash, Professor Harsh Mathur and Professor Alp Sehirlioglu. I would also like to thank Professor Harsh Mathur for all those discussions we had over coffee. He certainly introduced me to lots of coffee shops nearby. Then, I would like to thank our department assistant, Mrs. Betty Gaffney and our lab director, Dr. Diana Driscoll. They have been like a family to me here and I cannot thank them enough for their love and affection. During all these years at Case, I made some wonderful friends. I would like to thank them all, especially Saurabh Kumar and Mingdong Fan for their friendship and good food.

This journey has been an exciting yet painfully difficult one for me. With the passing of my mother, late Mrs. Abha Ratnaparkhe, I was unsure of what lied ahead of me. The support of my father, Mr. Arun Ratnaparkhe, my best friends, Mrinal Shekhar and Prashant Mishra, and my family throughout this period has been the reason why I have been able to make it this far. While it's hard to express my gratitude towards them in words, I sincerely thank them all for supporting me.

I'd also like to acknowledge the financial support throughout this journey. The

work on wide band-gap semiconductors  $\beta$ -Ga<sub>2</sub>O<sub>3</sub> as well as the (Al<sub>x</sub>Ga<sub>1-x</sub>)<sub>2</sub>O<sub>3</sub> alloy system was supported by the National Science Foundation(NSF) under the grant number 1755479. The work on ZnGeGa<sub>2</sub>N<sub>4</sub> was supported by the grant number 1533957. The ongoing work on  $\alpha$ -MoO<sub>3</sub> is supported by AFOSR under the grant number FA9550-18-1-0030. For the first two years, I was supported by the department of Physics in the form of teaching assistantship(TA) and I'd like to thank the department chair(s) for their kind support.

FIRST PRINCIPLES STUDY OF ELECTRONIC AND  
VIBRATIONAL PROPERTIES OF WIDE BAND GAP OXIDE  
AND NITRIDE SEMICONDUCTORS

Abstract

by

AMOL RATNAPARKHE

The ever-increasing number of applications requiring semiconductor materials at their core is driving the need to understand certain oxide and nitride materials. In this thesis, we investigate two of such classes. The first of those is the class of wide band-gap oxides and includes materials like  $\beta$ -Ga<sub>2</sub>O<sub>3</sub> and the (Al<sub>x</sub>Ga<sub>1-x</sub>)<sub>2</sub>O<sub>3</sub> alloy system.  $\beta$ -Ga<sub>2</sub>O<sub>3</sub> is the most stable of the five phases in which Ga<sub>2</sub>O<sub>3</sub> is found to exist. With a significantly high experimentally measured band gap of 4.5-4.9 eV, it is touted to be an excellent material for high-power electronics and UV transparent optoelectronic applications. Using first-principles calculations, we study this material and present the electronic band structure calculations using the quasiparticle self-consistent GW method. Next, we extend this study to the alloy system (Al<sub>x</sub>Ga<sub>1-x</sub>)<sub>2</sub>O<sub>3</sub> in which Ga<sub>2</sub>O<sub>3</sub> is alloyed with an even higher band-gap material, Al<sub>2</sub>O<sub>3</sub>. We study the system in both the phases,  $\alpha$  and  $\beta$ , present the electronic band structures for varying compositions of Al ranging from 0% to 100%, and predict the most favorable composition and phase for such an alloy to exist.

The second class of materials in this thesis is the alloy system formed by the combination of group III- and II-IV nitrides, GaN and ZnGeN<sub>2</sub>, respectively. In particular, we study the vibrational properties of ZnGeGa<sub>2</sub>N<sub>4</sub>. ZnGeGa<sub>2</sub>N<sub>4</sub>, at 50% composition, is an octet-preserving and lowest energy superlattice of half a cell of ZnGeN<sub>2</sub> and half GaN along the **b**-axis of ZnGeN<sub>2</sub> in the *Pbn*2<sub>1</sub> structure. Using Density Functional perturbation theory implemented in ABINIT, the phonon modes at the zone center,  $\Gamma$  allow us to calculate longitudinal optical-transverse optical splittings using Born

effective charges. In addition, the IR and Raman spectra along with the phonon density of states, and the phonon band structure are presented. Lastly, we study the transition metal oxide,  $\text{MoO}_3$ . We present the vibrational properties of orthorhombic  $\alpha\text{-MoO}_3$  with an emphasis on the IR and Raman spectra. We find good agreement with experimental IR and Raman studies of this materials, obtain its Born effective charges and explain the nature of the complex vibrational modes.

# Chapter 1

## Introduction

There is a strong interest currently in wide band gap oxides and nitrides that is driven by the immense number of applications in semiconductor devices. The fundamental properties of such materials, such as the band structure and the vibrational properties can be studied using first-principles calculations. Here we study three distinct materials systems,  $\beta$ -Ga<sub>2</sub>O<sub>3</sub> and the (Al<sub>x</sub>Ga<sub>1-x</sub>)<sub>2</sub>O<sub>3</sub> alloy, ZnGeGa<sub>2</sub>N<sub>4</sub> and MoO<sub>3</sub>. For Ga<sub>2</sub>O<sub>3</sub> and its alloys, we are focussing on the electronic structure while the other two namely, ZnGeGa<sub>2</sub>N<sub>4</sub> and MoO<sub>3</sub>, we will study the phonons and other vibrational properties.

### 1.1 $\beta$ -Ga<sub>2</sub>O<sub>3</sub> and (Al<sub>x</sub>Ga<sub>1-x</sub>)<sub>2</sub>O<sub>3</sub> alloys

There has been a significant interest in the study of  $\beta$ -Ga<sub>2</sub>O<sub>3</sub> over the past decade or so. The primary reason behind this surge of interest in  $\beta$ -Ga<sub>2</sub>O<sub>3</sub> can be attributed to the fact that it is a wide band-gap semiconductor with many applications ranging from high power electronics [1, 2, 3, 4] to deep UV transparent conductive oxide(TCO) [5, 6]. Ga<sub>2</sub>O<sub>3</sub> naturally is found to exist in five different forms. Of the five, it is found to be in its most stable form in the  $\beta$  phase. Previously known semiconductors like GaAs and GaN have experimentally measured band-gaps at about 1.4 eV and 3.4

eV, respectively. Compared with those numbers,  $\beta$ -Ga<sub>2</sub>O<sub>3</sub> has a rather big band gap of 4.5 – 4.9 eV. Materials with such high band gaps are usually insulators with high resistance. However, it was found that Ga<sub>2</sub>O<sub>3</sub> has semiconducting behavior because even unintentionally it was found to be n-type doped thanks to the presence of Si impurities. It's still not entirely clear why it tends to be unintentionally n-doped. It may very well depend on the growth method. What is clearly known is that it is possible to carry out intentional n-type doping in  $\beta$ -Ga<sub>2</sub>O<sub>3</sub> using Si, Ge and Sn that can act as n-dopants with shallow donor levels [7]. An important parameter for high power transistors is the breakdown voltage. It is the highest voltage that can be applied to a dielectric before its breakdown in which case the conductivity suddenly increases. For example, in Zener breakdown, the electrons start tunneling from the VBM to the CBM across the region when the applied voltage crosses the threshold value. There is a trend people have observed in semiconductors with large band gaps and their respective breakdown voltages. As seen from Fig. 1.1, the breakdown voltage grows exponentially with the band gap. And, given the high value of about 4.9 eV for  $\beta$ -Ga<sub>2</sub>O<sub>3</sub>, if the trend holds for  $\beta$ -Ga<sub>2</sub>O<sub>3</sub> then, its breakdown voltage will be much larger than either of GaAs or GaN. It is predicted to be as high as 8 MV/cm based on Fig. 1.1 and in real devices, it has already reached the value of 3.8 MV/cm [8].

Thus, there is a huge potential in this material to be used in applications in the fields of high frequency and power electronics [9].  $\beta$ -Ga<sub>2</sub>O<sub>3</sub> is also found to be n-type doped. Conventional transparent conductive oxides like ITO and ZnO are opaque in the deep-UV region due to their small band gaps ( $\sim$  3.2 eV). With the band gap as large as 4.9 eV.,  $\beta$ -Ga<sub>2</sub>O<sub>3</sub> has a much higher band gap which allows for much deeper UV transparency thus, it can be used as a transparent conducting oxide in the applications of UV range optical devices [10, 11].

In this dissertation, we investigate the electronic and optical properties of  $\beta$ -

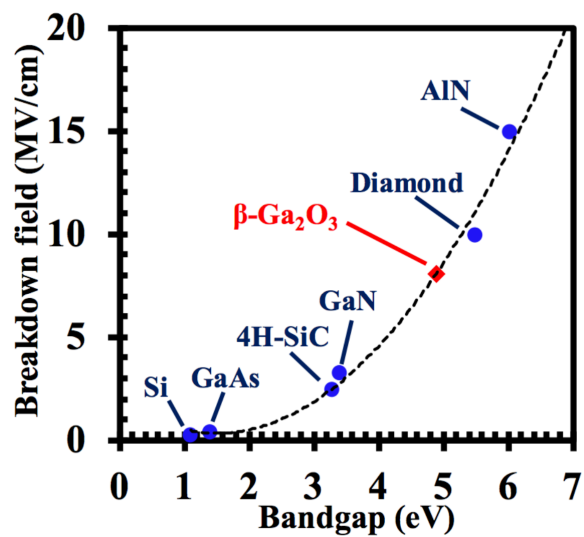


Figure 1.1: Breakdown field vs Bandgap [1]

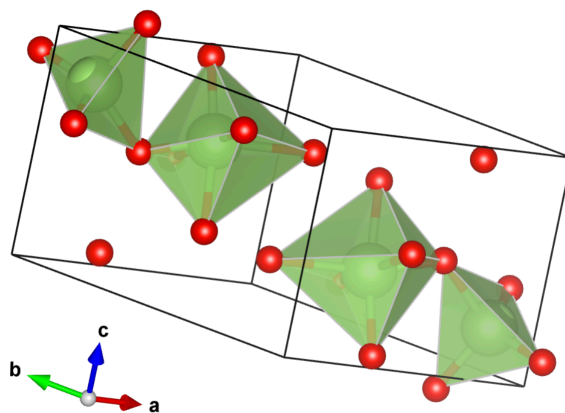


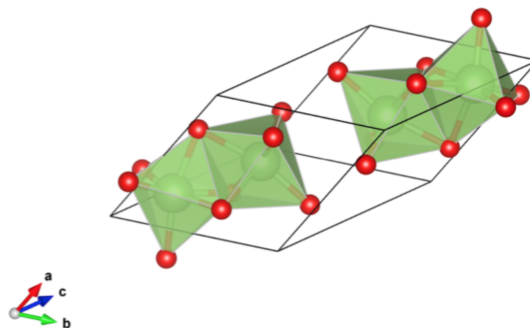
Figure 1.2:  $\beta$ -Ga<sub>2</sub>O<sub>3</sub> primitive unit cell

$\text{Ga}_2\text{O}_3$ . Since it is a somewhat novel material, the properties of this material are not yet fully understood. The band gap calculations, both theoretically and experimentally measured generally hover in the range 4.5-4.9 eV [10]. The conventional unit cell has 20 atoms. However, the primitive unit cell of the centered  $C2/m$  space group has half the number of atoms and is thus computationally more efficient to treat. The primitive unit cell is shown in Fig. 1.2. Our aim is to understand the electronic band structure of the material  $\beta\text{-Ga}_2\text{O}_3$  using the primitive unit cell as described by Geller [12]. It has a monoclinic crystal structure with the space group symmetry of  $C2/m$ . The cation sites are occupied by the Ga atoms which are equally divided among tetrahedral and octahedral coordinations. Our aim is to also understand the anisotropy in the absorption onset for the material by means of selection rules and the symmetry labels.

Self-trapping of holes in polarons has been found to occur in  $\beta\text{-Ga}_2\text{O}_3$  [6, 13]. Varley *et. al.* [13] investigated the role of self-trapped holes in the valence band region using hybrid functional calculations on  $\beta\text{-Ga}_2\text{O}_3$ . Self-trapping means that around a hole, even in the absence of an impurity or defect, there is a local distortion of the atoms around the hole which localizes the hole state. This creates a level in the gap for the self-trapped polaron. The conduction band is primarily derived from Ga s-orbitals while the valence bands come mainly from the O 2p orbitals. These orbitals are susceptible to the formation of polarons, *i.e.* holes trapped in a local potential well. They studied the stabilization of these self-trapped holes or STHs by calculating the energy differences between the STH and the delocalized holes and reported the optical absorption and emission energies associated with it. Based on the calculated emission line at 3.10 eV, they reported that their results are in excellent agreement with the experimentally observed emission lines in undoped single-crystal  $\text{Ga}_2\text{O}_3$  and concluded that the the UV luminescence exhibited by the material is indeed due to the presence of STHs. In a recent study of  $\beta\text{-Ga}_2\text{O}_3$ , Varley *et. al.* [14] explored the

luminescence of self-trapped holes and impurity-related acceptors. In the presence of acceptor impurities like  $\text{Mg}_{Ga}$ ,  $\text{Be}_{Ga}$ , the luminescence spectrum ranges from UV region to green but is often dominated by the ultraviolet band which is independent of the impurities present and is therefore associated with the ubiquitous self-trapped hole polarons.

Computationally, the band-gap has been calculated before by [10] using the Hybrid Density Functional Theory. They report a value of  $\sim 4.8$  eV by mixing about 35% of the exact Hartree-Fock non-local exchange with the conventional DFT exchange correlation potential. The 35% fraction of the exact exchange is chosen so as to match the calculations with the experimental results. The computations are carried out using the projector augmented wave(PAW) potentials implemented in the VASP code [15]. On the other hand, Bechstedt *et. al.* [16] used both, the standard DFT and Hedin's GW approximation in the single-shot approximation. They used the Generalized Gradient Approximation(GGA) for the DFT calculations implemented within the VASP code. Using a finer k-point mesh for their calculations, they reported the value of the indirect band-gap around 2.35 eV, significantly lower than the experimentally observed results. This result is expected as DFT is known for producing highly underestimated results and thus needs to be supplemented with additional tools to improve the results. In the GW single shot approximation starting from the above GGA result, they obtain a gap of 5.048 eV (direct) and 5.046 (indirect). In other words, they now predict that in GW the gap is direct and closer to the indirect gap and their value is somewhat larger than the experimental value. On the other hand, Mengle *et. al.* [17] performed the first-principles calculations of the near-edge optical properties of  $\beta\text{-Ga}_2\text{O}_3$ . Unlike [16] who reported direct band gaps, they reported indirect band-gap of 1.9 eV and 4.2 eV in LDA and LDA + GW, respectively using the Quantum Espresso code [18]. Experimentally, the band-gap has been measured using the methods of optical absorption onset [19]. Given the

Figure 1.3:  $\alpha$ - $\text{Al}_2\text{O}_3$  primitive unit cell

monoclinic crystal structure, the absorption spectra produced for polarization along the different axes vary and the results range from 4.9 eV for  $\mathbf{E} \parallel b$  to 4.54 eV for  $\mathbf{E} \parallel c$ .

$\text{Al}_2\text{O}_3$ , on the other hand is another oxide with a very high band-gap of about  $\sim 8.8$  eV. Commonly known as alumina,  $\alpha$ - $\text{Al}_2\text{O}_3$  is the most stable form of the many forms in which the oxide exists.  $\alpha$ - $\text{Al}_2\text{O}_3$  has been studied before and our aim in this dissertation is not really focussed on it but included in our study as the end member of alloys between  $\text{Ga}_2\text{O}_3$  and  $\text{Al}_2\text{O}_3$ . Many semiconductors related applications require that the band-gap be tailored with another material according to the needs of the device. This can be achieved by alloying the two oxides. Between the two stable oxides for Ga and Al, namely  $\beta$ - $\text{Ga}_2\text{O}_3$  and  $\alpha$ - $\text{Al}_2\text{O}_3$  there is a potential for an alloy system by changing the composition of the two cations,  $\text{Ga}^{3+}$  and  $\text{Al}^{3+}$ . This alloy system could potentially be used to tune the band gap as a function of the cation composition.  $\alpha$ - $\text{Al}_2\text{O}_3$  or the alpha phase exists in a crystal structure known as the corundum phase or  $R\bar{3}c$  whereas the  $\beta$ - $\text{Ga}_2\text{O}_3$  or the beta phase as we know, exists in the monoclinic crystal structure. The rhombohedral structure of  $\alpha$ - $\text{Al}_2\text{O}_3$  as seen in Fig. 1.3 also has an equal number of cation sites with all of them occupied by much smaller Al atoms. Unlike the  $\beta$  phase, all the cation sites are octahedrally coordinated to the neighboring O atoms. The question we want to address is which structure will

be adopted by an alloy or mixture of the two materials and over which range the  $\alpha$  or  $\beta$  structure has lower energy. The alloy  $(\text{Al}_x\text{Ga}_{1-x})_2\text{O}_3$  has already been grown and we intend to study this alloy in both of the  $\alpha$  and  $\beta$  structures to find out which one is lowest in energy as a function of the Al concentration,  $x$ . Later in the chapter on the Ga-Al alloy, we investigate in detail how the band gaps behave as function of concentration of Al and what the miscibility energy costs are.

## 1.2 II-IV nitride: $\text{ZnGeGa}_2\text{N}_4$

The second material we have studied in this thesis comes from the class of alloys formed by combining group III nitrides and the corresponding heterovalent II-IV-N<sub>2</sub> compounds. In particular, the compound under study is  $\text{ZnGeGa}_2\text{N}_4$ .  $\text{ZnGeN}_2$  can be viewed as obtained from GaN by replacing each Ga atom by either Zn or Ge in such a way that around each N, two of the neighbors are Zn and two are Ge instead of all four being Ga. This maintains the same average valence because Ga belongs in the column III of the periodic table and is thus trivalent while Zn and Ge are respectively divalent (II) and tetravalent (IV). Such II-IV-N<sub>2</sub> compounds are called heterovalent compounds. Often, just like their parent III-N compounds, these compounds tend to have similar properties such as the crystal structures, band gaps, and are thus of great interest.[20, 21, 22] They maintain the so-called octet rule of chemistry. By sharing the 3 valence electrons of Ga with 5 valence electrons of N, we maintain 8 electrons ( or a closed shell) around each atom. In other words, in the tetrahedral structure, where each atom has four neighbors, each bond will contain 2 electrons. The II-IV-N<sub>2</sub> have many similar properties compared to the corresponding III-N ones but provide additional flexibility in tuning the materials properties. And, the process of alloying these materials could help tune the properties for its applications. The two nitrides GaN and  $\text{ZnGeN}_2$  have similar crystal structure and the band gap is

roughly around 3.5 eV. The two are thus very similar in properties. However, there is a significant band offset between the two. The valence band offset is the energy difference between the valence band maximum between two materials when they are brought in contact with each other at an interface. It can depend on the interface orientation and the strain state of the two materials. For example, if one is in a thin film on top of a thick substrate, the film may be under compressive or tensile strain by the need to match the lattice constants in the plane. This strain itself affects the position and splitting of the VBM. The heterostructure of the two materials has the valence band maximum (VBM) in  $\text{ZnGeN}_2$  is about 1.1-1.4 eV above that of GaN at the junction [23, 24]. The origin of this band offset can be found in the fact that the Zn- $3d$  orbitals lie above the Ga- $3d$  orbitals and thus push the VBM with which the lower  $d$  states hybridize, to higher energy. Potentially, this band offset problem could present a way towards tuning the band gaps of the two materials. A natural way towards this solution is the formation of an alloy composed of these two nitrides.

Historically, alloys have been formed between various compounds in order to produce materials with desirable properties. Alloys help tune these properties to desired values and thus can be employed in numerous applications. Recently, mixed compounds of  $\text{ZnGeN}_2$  and GaN were studied by first-principles calculations [25]. Using the knowledge that the two nitrides have roughly the same crystal structure, at 50% composition, there are two possible pathways to creating a 16-atom unit cell for the alloy, with space groups  $Pmn2_1$  and  $P1n1$ . In order to preserve the octet rule in a mix of  $\text{ZnGeN}_2$  with GaN, one pair of ZnGe around each N needs to be transformed back to a pair of Ga atoms. Thus around each N we now need two Ga one Zn and one Ge. It turns out within the usual 16 atom cell, this can again be done in two ways. The lowest energy structure of this 50% compound with space groups  $Pmn2_1$  is a superlattice of half a cell of  $\text{ZnGeN}_2$  and half GaN along the  $\mathbf{b}$ -axis of  $\text{ZnGeN}_2$  in the  $Pbn2_1$  structure. The other octet rule preserving structure  $P1n1$  is formed

by starting with the 8-atom unit cell of  $\text{ZnGeN}_2$  in the  $Pmc2_1$  structure (this structure has a lower calculated band gap but high energy of formation in comparison with  $Pbn2_1$ ). From Fig 1.4, we can see how the different compositions of  $\text{ZnGeN}_2$  and GaN are realized in terms of the two phases of  $\text{ZnGeN}_2$ ,  $Pbn2_1$  and  $Pmc2_1$ . While both  $Pmn2_1$  and  $P1n1$  crystal structures satisfy the octet rule, and consequently, have a much lower energy of formation, there are two more possible superlattices with the stacking between half a cell of  $\text{ZnGeN}_2$  in  $Pbn2_1$  and half GaN along the **a**-axis or **c**-axis as seen in Fig 1.5. Both of these structures have local tetrahedra that break the octet rule. These structures are found to have high energy of formation and lower gap when compared to their octet rule preserving counterparts. The presence of the type II offset, where the VBM of  $\text{ZnGeN}_2$  lies above the one of GaN, while the CBM of GaN lies below that of  $\text{ZnGeN}_2$ , in principle, suggests that in a heterostructure composed of these two materials, the gap at the interface between the CBM of GaN and the VBM of  $\text{ZnGeN}_2$  could be lowered by about 1 eV thus, expecting the gap to be smaller than in either  $\text{ZnGeN}_2$  or GaN. However, contrary to the expectations, the calculations showed that the gap is actually slightly higher than both  $\text{ZnGeN}_2$  and GaN. This anomaly was explained by taking into account the size quantization effects in thin electrons quantum wells of GaN or hole quantum wells of  $\text{ZnGeN}_2$ . This effect effectively cancels the reduced gap due to the type - II band-offset causing this unexpectedly high band gap of about 3.82 eV [25].

The  $\text{ZnGeN}_2$ -GaN alloys were first synthesized using the technique of powder synthesis [26]. It lead to a disordered system having lower gap than its constituents. The initial idea behind the synthesis of this material was indeed to grow a material with a lower gap. However, the random distribution of the ions isn't an ideal property in such materials due to the higher energy of formation and failure to obey the octet rule. Overall, the goal is to grow a charge-neutral crystal. In case of local deviations in the cations, the compensating defects must form some locally positive and some

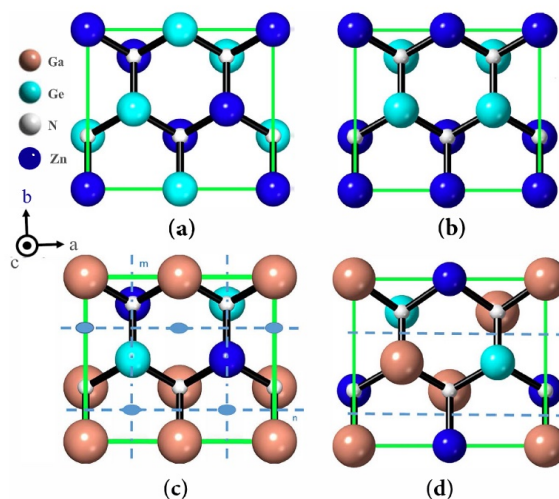


Figure 1.4: Octet-rule preserving  $\text{ZnGeGa}_2\text{N}_4$  structures and their relation to  $\text{ZnGeN}_2$  with (a)  $Pbn2_1$ , (b)  $Pmc2_1$ , (c)  $Pmn2_1$ , and (d)  $P1n1$ . Image taken from [25].

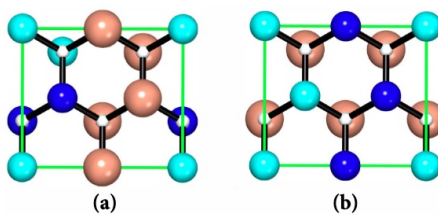


Figure 1.5: Non-octet-rule-preserving  $\text{ZnGeGa}_2\text{N}_4$  structures: (a)  $[100]_{1/2}$  and (b)  $[001]_{1/2}$  superlattices, based on the  $Pbn2_1$   $\text{ZnGeN}_2$  structure. Image taken from [25].

locally negative regions. This might then lead to strong charged defect scattering of carriers and lower mobility. Recently, the crystals of the 50% composition of  $\text{ZnGeN}_2$  and GaN were grown using the method of Metalorganic Chemical Vapor Deposition (MOCVD) [27].

### 1.3 Transition metal oxide: $\text{MoO}_3$

Another interesting material we investigate in this thesis is the layered transition metal oxide,  $\text{MoO}_3$ . The stable phase of  $\text{MoO}_3$  has an orthorhombic crystal structure and is known as the  $\alpha$ - $\text{MoO}_3$ . However, it's also known to exist in a metastable monoclinic phase [28].  $\text{MoO}_3$  has been found to have many applications in the fields of chemical sensing[29, 30], batteries[31], catalysis,[32]. Due to its very high electron affinity, it has applications as hole-extraction layer in organic photovoltaic cells.[33]  $\text{MoO}_3$  thin films have also been found to have high dielectric constant and were used as the gate oxide in thin film transistors.[34] Owing to its layered crystal structure and weak van der Waals force between the layers, it is touted to be an excellent candidate oxide for exfoliation to mono- or few-layer ultra-thin films [35].

Previous experimental results on the Raman and infrared spectra have been reported and can be found in [36, 37, 28, 38]. To the best of our knowledge, no prior first-principles calculations of the vibrational modes have been performed and only semi-empirical ball and spring constant models were used in the previous works to model these spectra. In this thesis, we present a first-principles calculation of the phonons in  $\alpha$ - $\text{MoO}_3$  including simulations of the Raman and infrared spectra. More details about the material, in particular, the crystal structure, the related symmetries and the results are provided in the subsequent chapters.

# Chapter 2

## Computational Methods

In this thesis, we apply several of the existing computational methods to understand the electronic, optical and vibrational properties of semiconductor materials. Among them are density functional theory(DFT), quasi-particle self consistent GW method (QSGW) and the density functional perturbation theory(DFPT). Density functional theory is the primary method used for calculating the ground state energies of materials. However, for the study of the excited states, the answers provided by DFT are not accurate enough. This gives rise to other improvements over DFT in the form of QSGW theory. And, for the study of vibrational properties, we have employed density functional perturbation theory within the ABINIT package[39].

### 2.1 Density Functional Theory

Density Functional Theory(DFT) has been the cornerstone of Solid State Physics since its inception. The foundations of DFT were first laid down by Hohenberg-Kohn in their 1964 paper [40]. The details of density functional theory can be found in many textbooks including the original papers of the founding authors. In this dissertation, I'll summarize chapters 6 and 7 of the book, *Electronic Structure* [41]. Density functional theory was formulated to be an exact theory of many-body systems. It

is a computational method used primarily to study the electronic structure (mainly, ground state properties) of the many-body systems. In order to calculate the properties of any many-body system, the Schrödinger equation for the many-body Hamiltonian has to be solved which in turn gives the wavefunction,  $\Psi$ . This wavefunction, essentially contains all the information regarding the system. The Hamiltonian for such a system can be written as

$$\begin{aligned} \hat{H} = & -\frac{\hbar^2}{2m_e} \sum_i \nabla_i^2 + \sum_{i,I} \frac{Z_I e^2}{|\mathbf{r}_i - \mathbf{R}_I|} + \frac{1}{2} \sum_{i \neq j} \frac{e^2}{|\mathbf{r}_i - \mathbf{r}_j|} \\ & - \sum_I \frac{\hbar^2}{2M_e} \sum_I \nabla_I^2 + \frac{1}{2} \sum_{I,J} \frac{Z_I Z_J e^2}{|\mathbf{R}_I - \mathbf{R}_J|} \end{aligned} \quad (2.1)$$

In this equation, the electrons and the nuclei are represented by indices  $(i, j)$  and  $(I, J)$ , respectively. The operator can be broken down into the electronic and nucleic kinetic energy terms, the nucleon-nucleon, electron-electron and the electron-nucleon interaction terms. Solving for such a system in the presence of complex interaction terms is nearly impossible due to the order of parameters involved, roughly equal to the Avogadro number. Thus, we employ approximations to make the equations simpler to solve. The Born-Oppenheimer approximation enables us to reduce the number of parameters involved. Using the fact that the electrons are much lighter than the nuclei, we assume the nuclei to remain fixed in their positions while the electrons move around them. The Born-Oppenheimer approximation decouples the nuclear and the electronic motion and thus the two can be solved independently. Reducing the complex Hamiltonian to a much simpler one looks like

$$\hat{H} = -\frac{\hbar^2}{2m_e} \sum_i \nabla_i^2 + \sum_i V_{ext}(\mathbf{r}_i) + \frac{1}{2} \sum_{i \neq j} \frac{e^2}{|\mathbf{r}_i - \mathbf{r}_j|} \quad (2.2)$$

Here, we're only considering the motion of electrons in a lattice of fixed nuclei. The Hamiltonian can be split into the kinetic energy, the electron-electron interaction

energy and the interaction term between the nuclei and the electrons in terms of  $V_{ext}(\mathbf{r})$ . This however, is still a  $3N$ - dimensional problem. In a nutshell, the goal of DFT is to reduce the complex problem of  $3N$  degrees of freedom to only 3.

The Hohenberg-Kohn theorem states that all the ground state properties can be exactly calculated from the ground state electron density of the many-body system. Except for a constant, there is a unique external potential that determines the ground state electron density. Solving for the Schrödinger equation gives us the many-body wavefunction and by extension, the properties as well. The second Hohenberg-Kohn theorem states that a universal energy functional  $E[n]$  can be defined as a function of the electron density,  $n(\mathbf{r})$  for any external potential,  $V_{ext}(\mathbf{r})$ . And, for any given external potential  $V_{ext}(\mathbf{r})$ , the energy surface,  $E[n]$  is then minimized to obtain the ground state energy and the argument,  $n(\mathbf{r})$  that minimizes the energy is the ground state electron density for the system. Thus, the existence of such a functional and the corresponding ground state energy is known. However, we still don't know about the construction of any such energy functional.

The solution to this problem was proposed by Kohn and Sham [42]. The Kohn-Sham approach was to consider an alternative system where the ground state electron density is exactly the same as the interacting many-body system. And, the interacting particles are replaced by non-interacting particles. This leads to independent-particle equations which are much easier to solve. The approximate energy functional now can be written in terms of the electron density as

$$E_{KS} = T[n] + E_{Hartree}[n] + E_{xc}[n]. \quad (2.3)$$

The Hartree term is written in terms of the density as

$$E_{Hartree}[n] = \frac{1}{2} \int d\mathbf{r} d\mathbf{r}' \frac{n(\mathbf{r})n(\mathbf{r}')}{|\mathbf{r} - \mathbf{r}'|} \quad (2.4)$$

The density itself is given by

$$n(\mathbf{r}) = \sum_i^N |\psi_i(\mathbf{r})|^2 \quad (2.5)$$

and, the wavefunctions  $\psi$  are the solutions to the one-particle Schrödinger equation

$$\left[ -\frac{1}{2}\nabla^2 + V_{eff}[n](\mathbf{r}) \right] \psi_n = \epsilon_n \psi_n. \quad (2.6)$$

Now, once we have these one-particle wavefunctions, we can express our kinetic energy in terms of the one-particle wavefunctions that constitute the density as

$$T = \sum_i^{occ} \int \psi_i^*(\mathbf{r}) \nabla^2 \psi_i(\mathbf{r}) d\mathbf{r} \quad (2.7)$$

$V_{eff}[n(\mathbf{r})]$  is a functional of the density. It is composed of three parts and is explicitly written as

$$\begin{aligned} V_{eff}[n](\mathbf{r}) &= V_{ext}(\mathbf{r}) + V_{Hartree}(\mathbf{r}) + V_{xc}(\mathbf{r}) \\ &= V_{ext}(\mathbf{r}) + \frac{\delta E_{Hartree}}{\delta n(\mathbf{r})} + \frac{\delta E_{xc}}{\delta n(\mathbf{r})} \end{aligned} \quad (2.8)$$

The first term  $V_{ext}(\mathbf{r})$  is the Coulomb potential felt by the electrons due to the nuclei. Second is the Hartree term which accounts for the electron-electron interactions and the last term is the exchange-correlation term. Since the electrons in this alternate system are assumed to be non-interacting, we have to account for the quantum effects like exchange and correlation interactions between the electrons owing to the fact that Pauli exclusion principle forbids the two electrons with the same spin from coming close thus keeping the electrons farther to lower the energy. We can think of the exchange-correlation term as a correction term which compensates for using the non-interacting system by incorporating all the exchange and correlation

effects. The two most common procedures for calculating  $E_{xc}$  that we have employed in this thesis are local density approximation(LDA) and generalized gradient approximation(GGA). In LDA, it can be expressed as

$$E_{xc}[n] = \int d\mathbf{r} n(\mathbf{r}) \epsilon_{xc}([n], \mathbf{r}) \quad (2.9)$$

where  $\epsilon_{xc}([n], \mathbf{r})$  is the energy per electron at position  $\mathbf{r}$  and it depends only on the density,  $n(\mathbf{r})$  in its neighborhood.

This set of equations (2.5, 2.6 and 2.7) can then be solved iteratively starting with a trial effective potential until we arrive at the lowest energy from eq. 2.3.

Finally, once we have the lowest energy for the fixed positions of the nuclei, the total energy of the system can be optimized as the nuclei move on the energy surface. This relaxation of the nuclei eventually leads to the ground state energy of the system.

### 2.1.1 FP-LMTO Method

For our purposes, we need to solve Eq. 2.6 for a periodic crystal. Using Bloch's theorem and the translational symmetry of the crystal in terms of the Bloch functions, it allows us to reduce the periodic lattice to a single unit cell. The Schrödinger equation is then solved using the variational principle. It is done by expanding the eigenstates of Eq. 2.6 in a basis set. The basis set could in principle, consist of plane waves or Bloch sums of atomic like wave functions around each atom. Since, it is the valence electrons that participate in bonding, the effective potential of the nuclei gets often replaced by pseudopotentials which describe the interactions with the core electrons and nuclei. For example, we use ABINIT for the study of the vibrational properties of the semiconductors. ABINIT uses the basis set of plane waves and treats only the valence electrons. In an all-electron method, one keeps all the electrons but typically describes core electrons separately and calculated with atomic boundary

conditions. However, the valence electrons are then required to be orthogonal to the core states. Nonetheless it has the advantage that the total density is used in the exchange correlation so that core-valence exchange is included. Comparing with the pseudopotentials, the all electron methods tend to be more accurate. Among the many variants out there, we use the full-potential LMTO or FP-LMTO method for our calculations.

FP-LMTO[43, 44] is an augmentation based method. It means the space is first divided in different regions, in this case a sphere around each atom and the interstitial space in between the spheres. The basis functions are then constructed from the solutions of the Schrödinger equation separately in each region at some fixed energies in the energy range of interest and stitched together. This process of stitching the solutions together is called augmentation. For example, in the interstitial region, the potential is approximately constant and for the purpose of constructing the basis set, it is assumed to be flat. Inside the spheres, the potentials are approximately spherically symmetric (dominated by the  $-Z/r$  nuclear potential) and again for the purpose of constructing the basis set, we assume it is spherical. Later on in the construction of the Hamiltonian, these approximations are relaxed and no longer imposed. This division of space is called the muffin-tin construction because of its resemblance to a muffin-tin, which is a pan to bake muffins in. The actual muffin-tin would be a two dimensional cross section of the potential as function of space in a plane. So far, we have talked about how the space is divided into the spherical and interstitial regions and the process of augmentation. Next, we need to talk about the construction of the basis set. In the oldest of the augmentation type methods, the augmented plane wave method (APW), the solutions inside the interstitial region are simply plane waves but, they are now expanded in spherical harmonics around each sphere and thereby matched in value and slope to the solutions of the radial Schrödinger equation in each sphere. To be able to match them in value and slope

one needs to use two functions inside, these are the radial functions at some chosen linearization energy and its energy derivative. This then turns it into the LAPW method with L standing for linearized. (In the original APW method one matches only the value but not the slope, so they still have kinks but are also still energy dependent. This leads to a more cumbersome method where the energy ultimately has to be chosen so as to make the kinks go away once linear combinations of these basis functions are used.) Now, in the LMTO method, instead of plane waves the interstitial choice of "envelope" functions are spherical waves centered around each atom. These are decaying Hankel functions times spherical harmonics if we choose the energy in this region to be slightly negative relative to the constant potential in the interstitial region, which is called the muffin-tin zero. In our actual method, these are replaced by slightly more sophisticated smoothed Hankel functions. But again they are now replaced inside each sphere, its own sphere around which it is centered and all other spheres in the system, by matching solutions inside the spheres by the above described augmentation procedure. So, this is possible because one knows how to expand a spherical harmonic times Hankel centered on one site about another one. This is described in terms of so-called structure constants. (With smoothed Hankel functions, they are actually expanded in polynomials in an approximate way instead of having analytical equations for the structure constants.) Once we have the basis functions defined, all one needs to do is calculate the expectation values of the Hamiltonian and the overlap matrix between all these basis functions and diagonalize the Hamiltonian matrix. This is done by applying the variational Rayleigh-Ritz method. It finds the right linear combinations of the basis functions which give the actual solutions of the full Hamiltonian of the system. For a crystal, first the basis functions are turned into Bloch sums so they are already Bloch functions but not yet solutions of the Hamiltonian but this then means that one has to diagonalize a Hamiltonian at each point  $k$  in the BZ. In the next section, we see how FP-LMTO

is implemented within the QSGW method to address the excited state energies to improve upon the performance of DFT.

## 2.2 QSGW Method

Density Functional Theory is a good approach when dealing with the ground state properties. However, the framework falls short when it comes to calculating excited state properties like the band structure. While the eigenvalues of the DFT Kohn-Sham equation for a periodic crystal are often called the band structure, within the DFT framework, these eigenvalues do not have the meaning of excitation energies, i.e. the energy for adding or removing a particle in that state from the N-particle system. They are just an intermediate result related to the fictitious non-interacting particle system used in the construction of the DFT total energy. The measurable band structure corresponds to the addition/removal energies and is an excited state property. To counter this problem, we use Quasi-particle self consistent GW (QSGW) method [45, 46, 47] to calculate all the excited state properties. QSGW is a perturbation theory based framework which improves upon Hedin's work [48, 49] on GW approximation. Before beginning with QSGW, it is useful to summarize the GW framework upon which it is built.

GW theory is a many-body-perturbation theory approach for calculating the one-particle excitation energies. These are the energies for adding or extracting a particle to the interacting N-electron system and they are called quasiparticle energies. All effects of the interactions in this theoretical framework beyond the Hartree term are described by an energy dependent ( or time-dependent) self-energy operator,  $\Sigma$ . The one particle excitations are described by the one-particle Green's function  $G$ . In the Hedin's theory, the self-energy is expanded in the screened as opposed to the bare electron electron interaction  $W$  and the first term in this series is schematically

$\Sigma = -iGW$  and hence it is called the GW approximation.

To illustrate it in a little more detail, we begin with the one-particle Hamiltonian

$$H^0 = -\frac{\nabla^2}{2m} + V^{eff}(\mathbf{r}, \mathbf{r}') \quad (2.10)$$

where  $V^{eff}(\mathbf{r}, \mathbf{r}')$  is the non-local potential operator used for the alternate system in the Kohn-Sham framework. This Hamiltonian,  $H^0$  determines the set of eigenvalues and eigenfunctions,  $\{\epsilon_i, \psi_i(\mathbf{r})\}$ . Once we have the set, we can construct the non-interacting Green's function  $G^0$  as

$$G^0(\mathbf{r}, \mathbf{r}', \omega) = \sum_i \frac{\psi_i(\mathbf{r})\psi_i^*(\mathbf{r}')}{\omega - \epsilon_i \pm i\delta} \quad (2.11)$$

where  $-i\delta$  and  $i\delta$  correspond to occupied and unoccupied states, respectively. We write the screened Coulomb interaction in the random phase approximation(RPA) as

$$W = \epsilon^{-1}v = (1 - v\Pi)^{-1}v \quad (2.12)$$

where  $\Pi = -iG^0 \times G^0$  is the polarization function and  $v(\mathbf{r}, \mathbf{r}')$  is the bare Coulomb interaction. Drawing similarities with the Kohn-Sham framework, here the self-energy operator will take care of all the interactions between the particles. In Hedin's framework, the self-energy is written as

$$\Sigma(1, 2) = iG^0(1, 2+)W(1, 2) \quad (2.13)$$

where the arguments for the self-energy, e.g., 1 refers to the position  $\mathbf{r}_1(\sigma_1, t_1)$ . The self-energy,  $\Sigma$  is dynamic and thus, it can be written in the time-dependent way. However, in practice, we do not use the time-dependent expression for the self-energy.

Instead, we perform a Fourier transformation over the energy,  $\omega$  giving

$$\Sigma(\mathbf{r}, \mathbf{r}', \omega) = \frac{i}{2\pi} \int d\omega' G(\mathbf{r}, \mathbf{r}', \omega - \omega') W(\mathbf{r}, \mathbf{r}', \omega') e^{-i\delta\omega'}. \quad (2.14)$$

The self energy,  $\Sigma$  is calculated by doing a convolution over the energy with a convergence factor of  $e^{-i\delta\omega}$ . Thus, the self-energy now is not only non-local but energy-dependent too. The one-body effective potential in GW approximation can thus be written in terms of this non-local but energy-dependent  $\Sigma$  as

$$V^{GW} = V^{ext} + v^{Hartree} + \Sigma \quad (2.15)$$

Thus, using Dyson's equation, we can construct the interacting one-body Green function as  $G = 1/[-\nabla^2/2m + V^{GW}]$ , it can be seen that the GWA maps the one-body  $V^{eff}$  from eq. (2.10) to  $V^{GW}$  in Eq. (2.14). In other words, the difference  $\Delta V = V^{GW} - V^{eff}$  can be thought of as the perturbative correction to the LDA Kohn-Sham energies. In the context of QSGW, this correction is regarded as the 1-shot GW and the results obtained are observed to be somewhat dependent upon the choice of the starting Hamiltonian,  $H^0$ .

QSGW formalism overcomes this dilemma to having to pick the suitable starting Hamiltonian by determining the effective potential,  $V^{eff}$  self-consistently. In other words, it attempts to find a self-consistent mapping procedure that determines  $V^{eff}$  by mapping  $V^{eff} \longrightarrow V^{GW} \longrightarrow V^{eff} \longrightarrow \dots$

Based on the quasiparticle picture, the fundamental equation for the excitations can be written as

$$\begin{aligned} & \left[ -\frac{1}{2m} \nabla^2 + V^{ext}(\mathbf{r}) + V^{Hartree}(\mathbf{r}) + V^{xc}(\mathbf{r}) \right] \Phi_n(\mathbf{r}) \\ & + \int d\mathbf{r}' [\Sigma(\mathbf{r}, \mathbf{r}', E_i) - V^{xc}(\mathbf{r})\delta(\mathbf{r} - \mathbf{r}')] \Phi_i(\mathbf{r}) = E_n \Phi_n(\mathbf{r}) \end{aligned} \quad (2.16)$$

The set of eigenvalues and eigenfunctions in the QP picture is  $\{E_i, \Phi_i\}$ . In QSGW, the perturbations are required to be small. Thus, the correction term  $\Sigma - V^{xc}$  is required to be as small as possible. Thus, to complete the self-consistent mapping, a mapping is constructed from  $V^{GW} \rightarrow V^{eff}$  as

$$V^{xc} = \frac{1}{2} \sum_{i,j} |\Psi_i\rangle [Re[\Sigma(\epsilon_i)]_{ij} + Re[\Sigma(\epsilon_j)]_{ij}] \langle \Psi_j| \quad (2.17)$$

under the approximation  $\{E_i, \Phi_i\} (\approx \{\epsilon_i, \Psi_i\})$ . Thus, we have constructed a mapping  $V^{eff} \rightarrow V^{GW} \rightarrow V^{eff}$ . For a given  $V^{eff}$ , we can calculate  $V^{xc}$  through  $\Sigma$  in the GW approximation. With this new  $V^{xc}$  together with  $V^{ext}$  and  $V^{Hartree}$ , we get a new  $V^{eff}$ . Thus, the QSGW method determines all the key components  $H^0, V^{eff}, W$ , and  $G$  self-consistently. The basis set for  $H^0$  is chosen to be the Bloch functions,  $\{\Psi_{\mathbf{k}n}(\mathbf{r})\}$  implemented in the full-potential LMTO method. The wavefunctions are restricted to the periodic unit-cell and the wavevector  $\mathbf{k}$  refers to the Brillouin zone while  $n$  represents the band index.

The QSGW method however, overestimates the GW corrections to the band gap typically by 20% of the self-energy correction. This overestimation was first observed in materials like GaAs and other semiconductors [47, 46]. The overestimation is actually caused in the calculation of  $W$  due to the overestimation in its screening and as seen from Eq. (2.13), gets passed along to the self-energy,  $\Sigma$ . In GW theory, the screening to the Coulomb potential is calculated from Eq. (2.12) and

$$\begin{aligned} \Pi_{I,J}(\mathbf{q}, \omega) = & \sum_{\mathbf{k}}^{BZ} \sum_n^{occ} \sum_{n'}^{unocc} \langle M_I^{\mathbf{q}} \Psi_{\mathbf{k}n} | \Psi_{\mathbf{q}+\mathbf{k}n'} \rangle \langle \Psi_{\mathbf{q}+\mathbf{k}n'} | \Psi_{\mathbf{k}n} M_J^{\mathbf{q}} \rangle \\ & \times \left( \frac{1}{\omega - \epsilon_{\mathbf{q}+\mathbf{k}n'} + \epsilon_{\mathbf{k}n} + i\delta} \right. \\ & \left. - \frac{1}{\omega + \epsilon_{\mathbf{q}+\mathbf{k}n'} - \epsilon_{\mathbf{k}n} - i\delta} \right), \end{aligned} \quad (2.18)$$

is the polarization propagator,  $\Pi$  [46].  $\Pi$  is expressed in the Fourier space in terms of

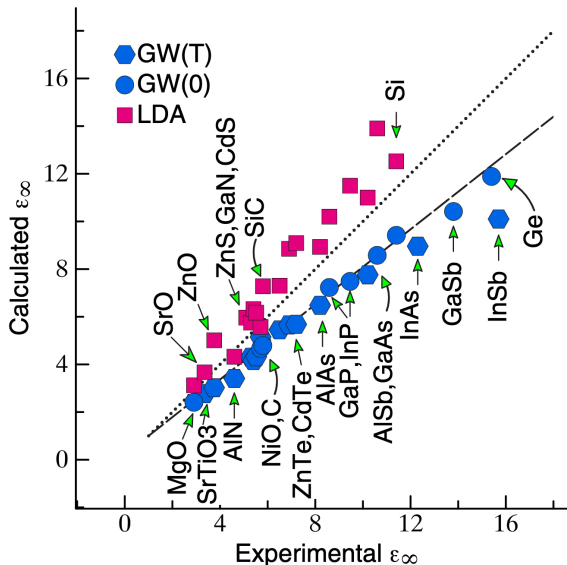


Figure 2.1:  $QSGW$ (blue) and  $LDA$ (red) optical dielectric constant  $\epsilon_\infty$  compared to experiment[55].

an auxiliary basis set  $M_I^q$ . These are Bloch functions and are a mix of plane waves and products of muffin-tin orbitals. In the calculation of the polarization however, only the bubble diagram contributions are considered while the more expensive ladder diagram contributions are not included. Thus, not considering the electron-hole contribution in the form of ladder diagrams leads to the underestimation in the calculation of the dielectric constant which, in turn, leads to the above mentioned factor of 20%. These corrections can now be done explicitly in Questaal [50] via the Bethe Salpeter equation(BSE) [51].

In practice, these calculations are very expensive to perform hence they have been performed only for a few materials with fewer atoms per cell. The alternative approach would be to find a simpler way of estimating how big these effects are. The idea of a 80% correction was first proposed by Chantis and Kotani [52, 53, 54].

An alternative approach by Shishkin *et. al.*[56] and later by Chen *et. al.*[57] proposed adding an exchange correlation kernel. Thus, replacing the polarization

propagator with a modified polarization,  $\tilde{\Pi}$  as

$$\tilde{\Pi} = [1 - (v + f_{xc})\Pi]^{-1}\Pi \quad (2.19)$$

where  $f_{xc}$  is an exchange-correlation kernel.

From Fig. 2.1, it can be seen that the agreement between the calculated(QSGW) and experimentally observed  $\epsilon_{\infty}$  is underestimated by about 20%. Bhandari *et. al*[55] compared the QSGW results with and without the exchange-correlation correction kernels and the ratio of the corrected self-energy contribution to the original QSGW gaps came out to be about 0.8 over all the materials studied. In conclusion, all of these studies indicate that for a wide range of materials, the additional computational work of incorporating the electron-hole effects in a better calculation of the screened potential,  $W$  led to the reduction of self-energy contribution to the band-gap by a universal factor of 0.2. This mixing of 0.8 factor of QSGW with 0.2 factor of LDA produces the results which present excellent agreement with the experiments.

## 2.3 Density Functional Perturbation Theory

The last method used in this thesis is the density functional perturbation theory. DFPT is a self-consistent perturbation theory built around the underlying density functional theory. It describes the response to a perturbation of the external potential to first order and is therefore sometimes also called linear response theory [58]. Such a perturbation of the external potential for example can arise from displacing an atom an infinitesimal amount and this theory then allows us to not only calculate the total energy and forces but also the corresponding force constants, which is what we will need to calculate phonons. The perturbation can also be an applied static electric field, in which case, the theory will allow us to calculate the electrical susceptibility. As discussed in the section on the DFT, the external potential and the electron density

are solved for in a self-consistent manner. In DFPT however, small perturbations in the system allow us to solve for the corrections in the DFT total energy where the first order changes in the external potential and the electron density are also solved for using the variational principle.

Starting with the Kohn-Sham orbitals as our wavefunctions, we can write our ground state electron density as

$$n(\mathbf{r}) = \sum_{\alpha}^{occ} \psi_{\alpha}^*(\mathbf{r})\psi_{\alpha}(\mathbf{r}) \quad (2.20)$$

Expanding the external perturbative potential  $v_{ext}(\lambda)$  in terms of the parameter  $\lambda$ , the first order response in the electron density,  $n^{(1)}(\mathbf{r})$  can be described as

$$n^{(1)}(\mathbf{r}) = \sum_{\alpha}^{occ} \psi_{\alpha}^{*(1)}(\mathbf{r})\psi_{\alpha}^{(0)}(\mathbf{r}) + \psi_{\alpha}^{*(0)}(\mathbf{r})\psi_{\alpha}^{(1)}(\mathbf{r}) \quad (2.21)$$

where  $\psi^{(1)}$  and  $\psi^{(0)}$  refer to the first and the zeroth order Kohn-Sham orbitals, respectively and the two are under the constraint

$$\langle \psi_{\alpha}^{(0)} | \psi_{\beta}^{(1)} \rangle \quad (2.22)$$

for all the occupied states  $\alpha$  and  $\beta$ . In eq. 2.21, we need the first order corrected wave functions which are obtained by solving the Sternheimer equations in a self-consistent manner. Using the variational approach, the first-order corrections to the wavefunctions are obtained from the Sternheimer equation

$$P_c(H^{(0)} - \epsilon_{\alpha}^{(0)})P_c |\psi_{\alpha}^{(1)}\rangle = -P_c H^{(1)} |\psi_{\alpha}^{(0)}\rangle, \quad (2.23)$$

where  $P_c$  is the projection operator acting on the empty or the conduction band

orbitals thus making sure that the orthogonality relation in Eq. (2.19) remain valid.

$$\begin{aligned}
 H^{(1)} = v_{ext}^{(1)} + v_{Hxc}^{(1)} = v_{ext}^{(1)} + \int \frac{\delta^2 E_{Hxc}}{\delta n(\mathbf{r}) \delta n(\mathbf{r}')} \Big|_{n^{(0)}} \mathbf{n}^{(0)}(\mathbf{r}') d\mathbf{r}' \\
 + \frac{d}{d\lambda} \frac{\delta E_{Hxc}}{\delta n(\mathbf{r})} \Big|_{n^{(0)}}
 \end{aligned}
 \tag{2.24}$$

The first-order perturbation  $H^{(1)}$  includes not only the bare external potential due to displacing an atom but also the self-consistent Hartree and exchange correlation potential from the first order corrected density of Eq. 2.21. Thus, again we need to solve a self-consistent set of equations. To be specific, we solve Eqs. 2.21, 2.23 , and 2.24.

Many physical properties can be efficiently calculated using the derivatives of the DFT total energy. In this thesis, we calculate the fundamental properties like the force constants. The  $(2n + 1)$  theorem states that using the  $n^{th}$  order corrections to the wavefunctions, we can calculate up to  $(2n + 1)^{th}$  order derivatives of the DFT total energy [59, 60]. The first-order corrected densities make second order errors in the density which lead to only  $4^{th}$  order errors in the total energy due to the variational principle underlying DFT. For example, for  $n = 1$ , we can potentially calculate the physical properties that involve up to  $3^{rd}$  order derivatives. Primarily, the two kinds of perturbations we are dealing with here are, the atomic displacements and a static external electric field.

In addition, DFPT allows us to calculate the mixed derivatives of the two perturbations as well. The force constants are the second order derivatives of the energy with respect to the atomic displacements that eventually lead to the dynamical matrices and the phonon frequencies over the Brillouin zone. The Born effective charges(BEC) on the other hand, are the mixed derivative of the total energy with respect to the displacements as well as the long range electric field. Born effective charges are required

to describe the long range dipole-dipole interactions in the polar materials. In addition, along with with the oscillator strength tensors, they provide the details about the LO-TO splittings in the  $q \rightarrow 0$  limit. The dielectric constants of the material are the second order derivative of the energy with respect to the electric field. The last quantity we investigate is the Raman tensor which can be described as  $3^{rd}$  order derivative of the total energy [61]. Namely, the Raman tensor involves the derivative of the susceptibility vs. atomic displacement. In other words, it involves two derivatives vs. electric field and one vs. atomic displacement. All the calculations using DFPT are performed using ABINIT. The underlying DFT has been implemented in the code in the basis of plane waves and pseudopotentials and unlike the FP-LMTO method, only the valence electrons interact with the ions.

An important advantage of DFPT is that for perturbations with a given wave vector, to linear order the response also has the same wavevector. For example, in a phonon mode a wave like displacement pattern is applied with a well defined wavevectors instead of displacing just a single atom in the crystal. What we then need is the corresponding perturbed first-order density response with the same wave vector, and from it the corresponding self-consistent potential which becomes part of the total first order perturbation. The DFPT theory can then be applied separately for each wave vector by working with the periodic parts of the Bloch functions and their corresponding Hamiltonian. Thus, the response can be worked out for wave like perturbations without the need for a supercell. All calculations can be done just using the primitive cell but they need to be done for each wavevector separately. Often we are interested only in the phonons at  $q = 0$  because they are the ones most easily measured with infrared or Raman spectroscopy. But even in this case, one is actually interested in the limit  $q \rightarrow 0$  which involves the above mentioned LO-TO splitting. But to obtain the full phonon band structure or phonon density of states, we need the dynamical matrix or force constants for several values of  $q$  in

the Brillouin zone. Additional details regarding the methods and the materials with specific crystal structures and symmetries , the IR and Raman spectra are provided in the subsequent chapters along with the results.

# Chapter 3

## QSGW study of $\beta$ -Ga<sub>2</sub>O<sub>3</sub>

### 3.1 Introduction

In the last few years  $\beta$ -Ga<sub>2</sub>O<sub>3</sub> has garnered a lot of interest mainly from an applied point of view because of its potential as an ultra-wide band gap semiconductor in high-frequency and power electronics. This has also led to a renewed interest in its fundamental properties, such as the electronic band structure, phonons among many others as can be seen in some of the recent work [62, 63, 64]. The band gap however, remains a property still somewhat uncertain among the practitioners (4.5-4.9 eV). The measurements of the band gap are based on the optical absorption onset. As expected for a material with monoclinic structure, the absorption onset shows anisotropy. The absorption onset was found to be larger for  $\mathbf{E} \parallel \mathbf{b}$  than for  $\mathbf{E} \perp \mathbf{b}$  but surprisingly, the energy difference between the two onsets is smaller at 77 K than at room temperature. The uncertainty in density functionals, even in hybrid functionals hasn't led to a complete first-principles understanding of the gap.

## 3.2 Computational Method

The QSGW framework has been explained in the chapter on computational methods. As discussed before, the GW method overestimates the band gap by about 20 %. This inconsistency is universal across semiconductors. This overestimate can be traced back to the underestimated screening of the screened Coulomb interaction,  $W$  by about 20 %. This underestimation is caused by the use of the random phase approximation (RPA) in the GW theory. In the calculation of the higher order corrections to the screened interaction,  $W$  the electron-hole interactions are not considered and this lack of additional ladder diagrams causes the underestimated screening. However, even including this 80% correction our initial QSGW calculations still seemed to overestimate the gap. We thus studied whether this can be due to electron-phonon coupling effects. Around the time this work was being completed, Botti and Marques [65] proposed that in polar materials, in addition to the electron-hole interactions, the lattice polarization corrections must also be included to account for the screening of  $W$ . In strongly ionic materials, these corrections can almost be of the order of 1 eV. We have included the lattice polarization effect in our calculations. The long range screened Coulomb interaction  $W(\mathbf{q} \rightarrow 0, \omega)$  must include the effects of the lattice relaxation on the dielectric response function  $\epsilon^{-1}$ . The Coulomb interaction diverges as  $\frac{1}{q^2}$  but in calculating the GW self-energy,  $\Sigma$  which involves a convolution over  $\mathbf{q}$ -space, this leads to an integrable divergence. Nonetheless, the  $\mathbf{q} = 0$  point and its neighborhood needs to be treated separately to treat this integrable divergence properly in evaluating its contribution to the self-energy. The behavior of the screened Coulomb energy in the limit  $\mathbf{q} \rightarrow 0$  involves the macroscopic inverse dielectric tensor or more precisely its projection along the direction unit vectors along which we approach  $\mathbf{q} = 0$ . In the usual GW method, this inverse dielectric tensor includes only the electronic screening. The simplest treatment for including the atomic displacements or lattice polarization, as proposed by Botti and Marques is then to replace  $\epsilon_{el}$

Table 3.1: Band gaps in  $\beta$ -Ga<sub>2</sub>O<sub>3</sub> in different approximations.

Approximation	LDA	QSGW	0.8 $\Sigma$	0.8 $\Sigma$ +LPC	0.8 $\Sigma$ LPC + ZPM
$E_g(\Gamma - \Gamma)$ (eV)	2.36	6.21	5.44	4.93	4.8 $\pm$ 0.1
$E_g(LI - \Gamma)$ (eV)	2.26	6.09	5.33	4.82	4.7 $\pm$ 0.1

by  $\epsilon_{total}$  in the neighborhood of  $\mathbf{q} \rightarrow 0$ . This change in macroscopic dielectric constant due to the lattice polarization can be related to the LO-TO splittings via the LST relation.

The Lydanne-Sachs-Teller(LST) relation reads as

$$\frac{\epsilon_{tot}^\alpha(\mathbf{q} \rightarrow 0, \omega)}{\epsilon_{el}^\alpha(\mathbf{q} \rightarrow 0, \omega)} = \prod_m \frac{(\omega_{LOm}^\alpha)^2 - \omega^2}{(\omega_{TOM}^\alpha)^2 - (\omega + i0^+)^2} \quad (3.1)$$

where the superscript  $\alpha$  corresponds to the direction along which  $\mathbf{q} \rightarrow 0$  and the product is over the modes for which there is an LO-TO splitting in that direction. The subscripts *tot* and *el* mean including lattice relaxation or purely electronic respectively. This lattice polarization correction (LPC) was recently implemented in the *GW* codes.[66, 50] It takes into account the anisotropy of the macroscopic dielectric tensor by means of the modified offset- $\Gamma$  method described in Kotani *et al.* [67] which itself is based on the approach by Friedrich *et al.* [68] It requires as input the LO and TO frequencies in the limit of  $\mathbf{q} \rightarrow 0$  for a few chosen directions. The phonon frequencies were taken from the recent first-principles density functional perturbation theory calculations of Liu *et al.* [69] For simplicity and because they were not available in this paper, we ignored the directional dependence of the LO phonon frequencies in the *ac* plane. Despite getting satisfactory results for  $\beta$ -Ga<sub>2</sub>O<sub>3</sub>, we will show in subsection 3.3.1 that this was somewhat fortuitous and did not give the right results for the right reasons.

The conventional unit cell consists of 20 atoms. However, it is advantageous to use the small, primitive unit cell. The lattice parameters for the cell were taken from

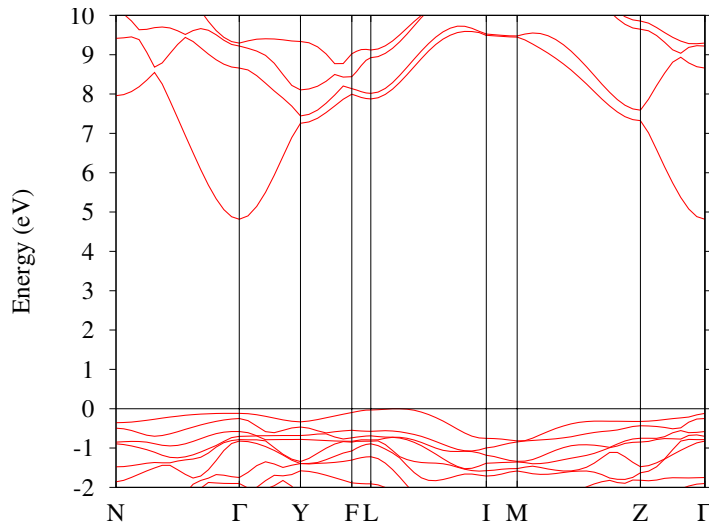


Figure 3.1: Band structure of  $\beta$ -Ga<sub>2</sub>O<sub>3</sub> in the  $0.8\Sigma$  QSGW approximation plus lattice polarization correction. The  $\mathbf{k}$ -point labels are named as in Ref. [10].

Geller [12]. The primitive unit cell of 10 atoms and the Brillouin-zone symmetry lines were constructed in the way described by Peelaers *et al.* [10] The Wyckoff positions of the atoms in the cell were relaxed using the density functional theory in the local density approximation using the FP-LMTO method.[43, 44] They agreed well with the values given in Peelaers *et al.* [10] A  $6 \times 6 \times 3$   $\mathbf{k}$ -point mesh was used for the self-consistency cycle in the DFT calculations. The band structure in the LDA agreed qualitatively with the hybrid functional results of Peelaers in that the gap is indirect, with a valence band maximum between  $L$  and  $I$  about 0.1 eV higher than at  $\Gamma$  and a conduction band minimum at  $\Gamma$ . Of course the gap in LDA is significantly underestimated.

### 3.3 Results

The band gaps at different levels of approximation are summarized in Table 3.1. A large basis set with two sets of smoothed Hankel function decays  $\kappa$  and smoothing radii was used:  $spdf - spd$  on both atoms for the QSGW calculations. A  $4 \times 4 \times 2$

$\mathbf{k}$ -point mesh was used. The interstitial plane-wave expansion used a cut-off of 3 Ry. Above 2.5 Ry the  $\Sigma(\omega)$  calculated up to  $\omega = 3$  Ry is approximated by an average diagonal matrix as explained in Ref. [46]. The Ga-4*d* states were treated as bands and the 3*d* as local orbital.[70] Alternatively, treating the Ga-3*d* as band with Ga-4*d* as local orbital and adding floating orbitals centered at interstitial sites gave a band gap of 6.12 eV in full QSGW and 5.36 eV in the 0.8 $\Sigma$  approach, in good agreement with the other calculation. Taking into account the 0.8 $\Sigma$  as well as the lattice-polarization correction, the direct gap at  $\Gamma$  is found to be 4.93 eV. The full band-structure near gap including the lattice-polarization and 0.8 $\Sigma$  corrections is shown in Fig. 3.1.

The zero-point motion correction to the gap was only recently implemented in first-principles calculations.[71, 72]

Here we only make a simple estimate of it based on the fact, which one can verify in Table III of Thewalt and Cardona[73], that the ZPM correction to the gap is proportional to the gap itself within a family of closely related semiconductors. Based on this observation and the ZPM correction of the gap of 0.15 eV in MgO, which has a somewhat larger gap of 7.8 eV, we estimate this correction to be of order 0.1-0.2 eV. With these corrections, the gap of  $\beta$ -Ga<sub>2</sub>O<sub>3</sub> is finally found to be 4.8 $\pm$ 0.1 eV in good agreement with experiment. The large lattice polarization effect of  $\sim$ 0.5 eV on the gap is indicative of strong polaronic effects, consistent with Varley *et al.*'s finding of a self-trapped hole-polaron.[13]

Table 3.2: Character table of  $C_{2h}$ .

irrep	$E$	$C_{2y}$	i	$\sigma_y$	
$\Gamma_{1+}$	$A_g$	1	1	1	s
$\Gamma_{2+}$	$B_g$	1	-1	1	-1
$\Gamma_{1-}$	$A_u$	1	1	-1	$y$
$\Gamma_{2-}$	$B_u$	1	-1	-1	$x, z$

### 3.3.1 Lattice polarization analysis

We briefly review the accuracy of the QSGW method and the above mentioned lattice-polarization correction for the band gap of  $\beta$ -Ga<sub>2</sub>O<sub>3</sub>. The above discussion based on our previous work [74] suggested that in order to obtain good agreement for the band gaps with experiment, both the electron-hole and lattice polarization or electron-phonon coupling effects were important. We had estimated the lattice polarization correction to the band gap to be as large as 0.5 eV. However, since then, new insights were gained. These findings were carried out in the study of (Al<sub>x</sub>Ga<sub>(1-x)</sub>)<sub>2</sub>O<sub>3</sub> alloys and thus led us to revisit the GW calculations for pure  $\beta$ -Ga<sub>2</sub>O<sub>3</sub>. And, contrary to the significant lattice polarization corrections reported in the original work, as we will see the LPC corrections actually turn out to be not so significant (< 0.1 eV).

The recent study [66] indicates that the previously implemented Botti-Marques approach is highly sensitive to the density of the  $\mathbf{q}$ -point mesh. The lattice polarization corrections are now understood to be applied only over a length scale set by the polaron length and they're specific to each band. This polaronic effect acts on the conduction band minimum (CBM) and the valence band maximum (VBM) separately and depends on the effective masses of the latter, which sets the polaron length scale over which the effect is active,  $a_P = \sqrt{\hbar/(2m_*\omega_L)}$ , where  $\omega_L$  is the longitudinal optical phonon. In principle, the contributions from all the phonons towards the calculation of  $a_P$  must be included. However, for a rough estimate of the upper limit of this effect, we pick the phonon with the highest frequency (as they have the shortest  $a_P$ ). Using a hole effective mass of  $2m_e$ , the polaron length scale for holes comes out to about  $8.5 a_0$ . The estimated effect on the VBM shift is then  $(e^2/4a_P)(\epsilon_\infty^{-1} - \epsilon_0^{-1})$  which amounts to about 0.07 eV with the factor  $(\epsilon_\infty^{-1} - \epsilon_0^{-1})$  being about 0.17. The corresponding shifts in the CBM are even smaller because the effective mass is much smaller ( $\sim 0.2$ - $0.3$ ) and the corresponding polaron length is about  $22 a_0$ . Thus, we estimate the total effect must be smaller than 0.1 eV because this assumed the highest

phonon fully contributed the maximal effect.

An alternative way for estimating this correction was developed based directly on polaron theory in the Fröhlich description of longitudinal optical phonon electron phonon interaction. We calculate the effect explicitly by adding a Lyddane-Sachs-Teller correction factor  $\epsilon_0/\epsilon_\infty$  to the macroscopic dielectric constant around the  $\mathbf{q} = 0$  point singularity of the screened Coulomb interaction. We apply this correction only to a region of  $\mathbf{q}$ -space of size  $1/a_P$ . The quantity,  $1/a_P$  (averaged over electrons and holes) gives a  $\mathbf{q}$ -point spacing of about  $0.04 a_0^{-1}$  and this amounts to about a  $10^{th}$  of the Brillouin zone in the  $ab$  plane.

We find that with a finer  $5 \times 5 \times 3$  mesh, adding this correction factor to the  $W$  at  $q = 0$  reduced the gap by 0.1 eV. It shows that in our previous work[74] where an insufficient  $\mathbf{k}$ -point sampling ( $4 \times 4 \times 2$ ) was used, the effect was overestimated. Thus, we conclude that we can safely neglect the electron-phonon effects on the gap but need a sufficiently fine  $GW$   $\mathbf{k}$ -point mesh. In fact, with a  $GW$   $\mathbf{k}$ -point mesh of  $5 \times 5 \times 3$  the gap was found to be 4.9 eV even without including any LPC. Thus the overestimate of the gap by QSGW in our first attempt was just a result of incompletely converged  $GW$  theory and not because of the need of a an additional LPC correction. Thus, these results for pure  $\beta$ -Ga<sub>2</sub>O<sub>3</sub> are in good agreement with experiment and no further corrections are needed for the alloys from this effect.

### 3.3.2 Absorption onset

We now turn to the origin of the anisotropy of the optical absorption. The absorption edge (shown in Fig. 3.2) is calculated from the band structures using the standard Adler-Wiser approach,[75, 76] neglecting local field or excitonic effects. For details of the implementation in the LMTO method and using the QSGW self-energy, see Ref. [77]. The optical absorption onset appears to behave as  $\propto E^2$  rather than  $\propto \sqrt{E}$ . This is because, except at the very onset, the band dispersion is nearly linear.

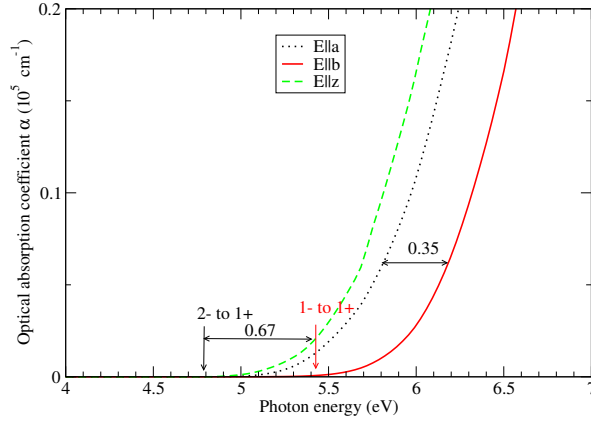


Figure 3.2: Calculated imaginary part of the optical dielectric function, for different polarizations in  $\beta$ -Ga<sub>2</sub>O<sub>3</sub>. The  $z$  direction is perpendicular to the  $ab$ -plane, close to but not exactly along  $\mathbf{c}$  because  $\mathbf{c}$  makes an angle  $\beta = 103.82^\circ$  with the  $\mathbf{a}$  axis.

The selection rules and symmetry labeling of the valence and conduction bands at the  $\Gamma$ -point is used to explain the absorption anisotropy. The space group of  $\beta$ -Ga<sub>2</sub>O<sub>3</sub> is  $C_{2h}^3$  (or  $C2/m$  in international notation). The  $b = y$  axis corresponds to the 2-fold symmetry axis. The character table is given in Table 3.2 giving the irreducible representations in two commonly used notations. The symmetry label and energy of the highest few valence bands and lowest few conduction bands at  $\Gamma$  are given in Table 3.3. The conduction band minimum (CBM) and valence band maximum (VBM) have symmetry  $A_g$  and  $B_u$  respectively. This implies according to the dipole selection rules that the lowest direct gap at  $\Gamma$  is allowed for polarizations  $\mathbf{E} \perp \mathbf{b}$ . This agrees with the experimental fact that the lowest onset of absorption occurs for  $\mathbf{E} \perp \mathbf{b}$ .

One can see that only the VBM-4, at  $-0.67$  eV has the proper symmetry ( $A_u$ ) to have dipole allowed transitions to the CBM for  $\mathbf{E} \parallel \mathbf{b}$ . This would suggest a shift of the onset of absorption as large as 0.67 eV. However, inspection of the calculated absorption curves in Fig. 3.2 shows that the splitting between the curves is only about 0.35 eV slightly above the edge in agreement with experimental extrapolations. This

Table 3.3: Energy levels at  $\Gamma$  near the VBM and CBM in 0.8 $\Sigma$ +LPC approximation, and their irreducible representation.

	$E_n$ (eV)	irrep
VBM-6	-1.633	$B_u$
VBM-5	-0.706	$A_u$
VBM-4	-0.669	$A_u$
VBM-3	-0.585	$B_g$
VBM-2	-0.464	$A_g$
VBM-1	-0.133	$B_u$
VBM	0.000	$B_u$
CBM	4.933	$A_g$
CBM+1	8.778	$B_u$
CBM+2	9.339	$A_g$
CBM+3	9.412	$B_u$
CBM+4	10.593	$B_u$
CBM+5	11.385	$A_g$

is because the selection rules strictly only apply at the high-symmetry point but are weakly broken if one goes slightly away from it in k-space. The ordering of the optical absorption onsets for the three different polarizations agrees with experiment[19] and the matrix element analysis of Mengle *et al.* ,[17] once we take into account the two different labelings of the axes: our  $x, y, z$  correspond to their  $z, x, y$ . There is a slight difference in the splittings of the valence bands and their 4th and 5th level are interchanged from ours. The reason for the difference between room temperature and 77 K is still unclear but suggests that the optical absorption at low temperature may be influenced by excitonic effects. Optical absorption calculations including excitonic effects were recently reported,[16, 78] and indicate the excitonic nature of the first peaks in optical absorption and the excitonic binding energy is of order 0.1 eV. The underlying reasons for the absorption anisotropy remain the same.

### 3.4 Conclusions

In summary, the QSGW method was found to obtain the band gap in excellent agreement with experiment provided a sufficiently dense q-mesh is used and the self-energy is reduced by a factor 0.8 to mimic the effect of electron-hole interaction effects missing in the polarization function as has been found in numerous other materials and is also justified in some detail in [55]. The electron-phonon coupling or specifically the lattice polarization effect were found ultimately to be at most 0.1 eV, once understood as being the polaronic corrections related to electron-phonon interaction with the LO phonons.

# Chapter 4

## QSGW study of $(\text{Al}_x\text{Ga}_{1-x})_2\text{O}_3$ alloys

### 4.1 Introduction

In the previous chapter, we discussed the QSGW band structure and the anisotropy of the absorption onset in  $\beta$ - $\text{Ga}_2\text{O}_3$ . Many semiconductor devices require tailoring the band gap in a closely related material, to construct heterostructures. In this chapter, we present the results for an alloy system of two oxides,  $\text{Ga}_2\text{O}_3$  and  $\text{Al}_2\text{O}_3$ . Both of these materials occur in different phases. The  $\alpha$ -phase which corresponds to the corundum structure, is the preferred phase for  $\text{Al}_2\text{O}_3$  while  $\text{Ga}_2\text{O}_3$  occurs in the monoclinic structure, or the  $\beta$  phase. The primitive unit cell of the  $\beta$  phase of  $\text{Ga}_2\text{O}_3$  was shown in 1.2 while the corundum or the  $\alpha$  phase can be found in 1.3. As can be seen from the two figures, the  $\beta$  phase has the 4 cation sites distributed equally among the tetrahedral and octahedral coordinations while in the case of the  $\alpha$  phase, all the cations are octahedrally coordinated and has an overall rhombohedral symmetry. In this chapter, we study the natural question that arises in an alloy system: of these two preferred crystal structures for its constituents, which one does

the alloy system prefer? As the proportion of Al can be changed in the alloy from 0 % to 100 %, it would be interesting if we could map the preferred ground state structure of the alloy system as a function of the concentration. This question had been addressed independently and simultaneously of our own work by Peelaers *et al.* [79]. It was published shortly before ours but still left some questions open. For example, they used the hybrid functional approach [80, 81]. How important was the use of hybrid functionals in obtaining their results and more importantly, they used only the lowest energy local configurations of the Al, in its site preference for octahedral vs. tetrahedral sites. Is this assumption justified in a random alloy and how does it affect the results?

## 4.2 Computational method

The lattice constants and internal coordinates of the atoms in both the primitive unit cells were optimized within density functional theory (DFT) in PBE-GGA using the ABINIT plane wave pseudopotential approach. We used the Hartwigsen-Goedecker-Hutter (HGH)[82] pseudopotentials from the ABINIT website and a plane wave cut-off of 50-70 Hartree and a  $4 \times 4 \times 4$  mesh to sample the Brillouin zone.

Keeping the structures fixed, we then recalculated the total energies in the all-electron full-potential linearized muffin-tin orbital (FP-LMTO) method, [43, 44] which has the advantage to be free of pseudopotential choices. Further relaxation of the internal coordinates was found not to change the structure or total energy. A well converged double- $\kappa$  smoothed Hankel function basis set was used with angular momentum cut-offs of *spdfspd* and augmentation cut-off inside the sphere of  $l_{max} = 4$ . Ga-3*d* semicore orbitals are included in the basis set as local orbitals (defined inside the muffin-tin sphere only). The Brillouin zone integrations of the total energy and self-consistency used a  $6 \times 6 \times 6$  mesh. The band structures were calculated using

the QSGW method[46] with most parameters chosen as in Ref. [74] except that we found it necessary to use a finer  $\mathbf{k}$ -point mesh for the  $GW$  calculations in order to obtain well-converged self-energy corrections to the band gap. Specifically, we find that in order to have comparable convergence in the  $\alpha$  and the  $\beta$ -structures, a mesh of  $5 \times 5 \times 3$  is required for the latter and  $4 \times 4 \times 4$  in the  $\alpha$  structure. This gives the QSGW gaps converged to better than 0.1 eV.

### 4.3 Modeling of disorder

Here we discuss the treatment of disorder. In principle, in an alloy one would need to consider an ensemble average over many different local configurations of the two different cations. One way to accomplish this is the special quasirandom structure (SQS) approach[83] in which one constructs the placement of the different A and B atoms of a chosen size supercell such that various correlation parameters, such as different distance pair correlations and other local motifs all are as close as possible to the random ones. The idea is then that the energy of formation or other properties of interest can be expanded in a cluster expansion in terms of these correlations or local structural motifs and the random average is then well represented by this one carefully chosen structure. In metallic alloys, one typically needs to include various pair correlation functions in this treatment. However, in a semiconductor, one can argue that what matters most for both, the total energy of bonding and for the band gap is the local coordination. For example, in a tetrahedrally coordinated semiconductor alloy with cation alloying, one could focus on the different tetrahedral environments of each anion, such as  $A_4$ ,  $A_3B$ ,  $A_2B_2$ , etc. Here we take this idea even one step further and assume that the properties will depend only on the relative occupation by the two atoms of the octahedral vs. tetrahedral sites. Within the 10 atom primitive cell of the  $\beta$ -structure, two cation sites are octahedral and two tetrahedral. Thus, we need

to average in principle only over the probabilities that each site is occupied by Al or Ga. We hence calculate the total energies and band gaps for all possible occupations and then average them according to a Boltzmann factor  $e^{-E/k_B T}$ . Now, if the energy differences between different sites are high compared even to the growth temperature, then it means the higher energy configurations will be strongly suppressed and we might as well assume only the lowest energy configuration occurs in the alloy. On the other hand, if the growth method is far from equilibrium, one could assume at the other extreme limit that the occupations are completely random. Specifically, for 25 % Al, the Al has then equal probability to be on a tetrahedral ( $t$ ) or octahedral ( $o$ ) site. Similar for 75 % the single Ga has equal probability to be on the tetrahedral or octahedral site. For 50 % there are 4 different configurations for the Al,  $tt$ ,  $oo$  and two different  $to$  configurations. The two different  $to$  configurations differ depending on whether the two Al are next to each other or separated by a Ga in between. We thus need to check whether these have different energies (and gaps) or not. Assuming that they are close or that we neglect their difference than we would average the  $tt$ ,  $to$ ,  $oo$  configurations for the Al occupation with probabilities 1/4, 1/2, 1/4 respectively. Our approach of considering all alloy configurations in a 10 atom cell is similar to Ref. [79] but somewhat more detailed analysis is provided here.

## 4.4 Results

### 4.4.1 Lattice constants

We first show the calculated pseudocubic lattice constants  $V^{1/3}$  where  $V$  is the volume per formula unit of the alloys as function of Al concentration  $x$  in Fig. 4.1 for both structures. Here we used the structure with lowest energy in terms of the different Al occupations. We can clearly see that the lattice constants vary linearly with composition, in other words, they obey Vegard's law. Secondly, we see that the

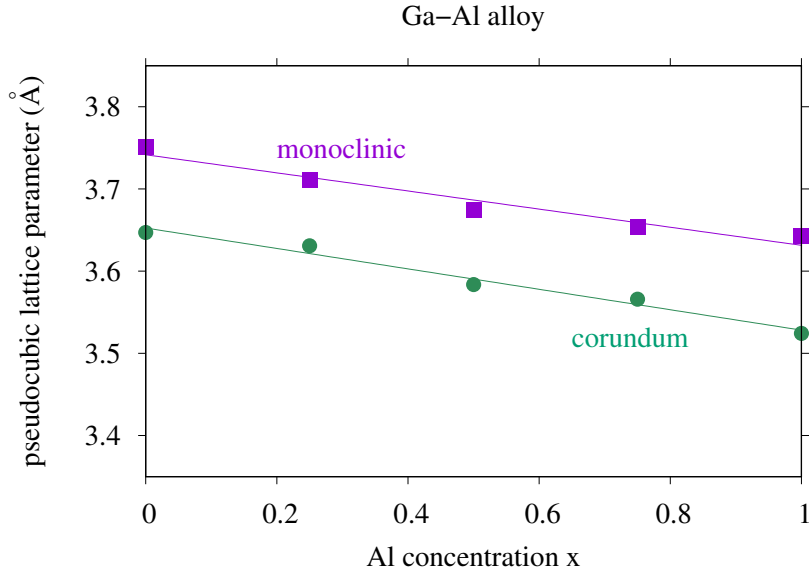


Figure 4.1: Pseudocubic lattice parameter of  $(Al_xGa_{1-x})_2O_3$  as function of  $x$  for both crystal structures.

lattice constant is systematically smaller for the corundum than for the monoclinic phase. The octahedral coordination usually leads to closer packing. Thus, the fact that there are 4 octahedral sites in corundum as opposed to 2 in monoclinic leads to a consistently smaller volume per formula unit across all the  $Al$  concentrations,  $x$ .

#### 4.4.2 Energy of formation

Next, we present the energies of formation, which are defined by

$$\begin{aligned}
 E_f[(Al_xGa_{1-x})_2O_3] &= E[(Al_xGa_{1-x})_2O_3] \\
 &\quad - xE[\alpha Al_2O_3] - (1-x)E[\beta Ga_2O_3]
 \end{aligned}
 \tag{4.1}$$

in Fig. 4.2. Please note that the reference energies of pure  $Ga_2O_3$  and pure  $Al_2O_3$  here are each calculated in their own lowest energy phase, whereas the alloy either can be in the  $\alpha$  or  $\beta$ -phase. This ensures that at the end points  $x = 0$  the monoclinic energy of formation is zero while at  $x = 1$  the corundum one is equal to zero. All of the total energies are per formula unit. We first consider only the lowest energy

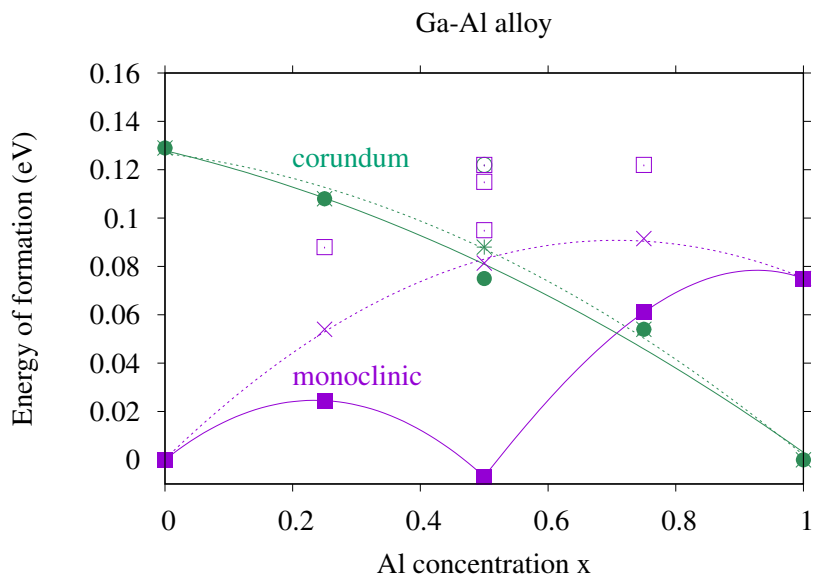


Figure 4.2: Energy of formation per formula unit for the alloys in the two structures across compositions. Solid data points show Al atoms occupying the octahedral positions while the higher energy hollow data points show the energies for configurations with increasing number of Al occupying tetrahedral sites. The  $\times$  and  $*$  show the average formation energies assuming random probability of the different configurations. The dotted lines show the corresponding interpolation while the solid lines assume the minimum energy configuration at each composition.

configuration at each composition, which for the  $\beta$  structure amounts to placing Al preferentially on octahedral sites. The results are in excellent agreement with those of Peelaers *et al.* [79] if we assume that the latter contains a typo in that the energies of formation here are per formula unit and not per cation. It is clear from the results that the Al strongly prefers to occupy the octahedral site. The energy difference per  $\text{Al}_t$  going on a tetrahedral site however is not constant. The energy difference at the 50 % concentration  $\Delta E_{to} = E_{to} - E_{oo}$  is not equal to that of  $E_t - E_o$  at 25 %, where only one Al needs to choose between a tetrahedral and octahedral site and the energy difference  $E_{tt} - E_{to} \neq E_t - E_o$ . This indicates that other aspects of the local configuration do play a role besides the nearest neighbor coordination.

The fact that the energy of formation in the monoclinic structure has a non-monotonic, bimodal distribution is interesting, in particular that the energy of formation even has a slightly negative value at 50 % is remarkable. The lower energy for adding two Al instead of one may in part be because this is a more symmetric structure. The two Al both on octahedral sites are related by the mirror plane symmetry perpendicular to the  $\mathbf{b}$ -axis. The low energy of formation is clearly related to the optimum octahedral surrounding of Al combined with tetrahedral surrounding for Ga. Strictly speaking, the negative value of the energy of formation for this configuration indicates that the 50 % compound with all Al occupying octahedral sites is a separate crystalline phase distinct from a disordered alloy and would constitute a new compound on the convex hull in the ternary phase diagram.

To further study the effects of the Al distribution, we calculated the energy of formation and the band gaps for different configurations as shown in Table 4.1. These results are also shown as open symbols in Fig.4.2. We can see here that for the 50 % composition, four different Al distributions can be considered in the unit cell. Both Al on octahedral site, both on tetrahedral site and two different ways of one Al octahedral and one tetrahedral. The latter two differ in that in one case, the

Table 4.1: Energy of formation per formula unit and band gaps in different configurations as function of concentration in  $(\text{Al}_x\text{Ga}_{1-x})_2\text{O}_3$  alloys. In the monoclinic structure the configuration is specified by which atoms go in the octahedral (o) and tetrahedral (t) sites. In the corundum structure, the sites are all octahedral but we can still distinguish the corner (c) and middle (m) sites in the structure.

$x$	Config.	$\Delta E_f$ (meV)	$E_g$ (eV)
monoclinic structure			
t-o-o-t			
0.00	Ga-Ga-Ga-Ga	0	4.91
0.25	Ga-Ga-Al-Ga	20	5.48
0.25	Al-Ga-Ga-Ga	88	5.64
0.50	Ga-Al-Al-Ga	-7	6.16
0.50	Al-Ga-Ga-Al	122	6.30
0.50	Al-Al-Ga-Ga	95	6.20
0.50	Ga-Al-Ga-Al	116	6.25
0.75	Al-Ga-Al-Al	122	6.82
0.75	Al-Al-Al-Ga	61	6.87
1.00	Al-Al-Al-Al	75	7.74
corundum structure			
c-m-m-c			
0.00	Ga-Ga-Ga-Ga	129	5.28
0.25	Al-Ga-Ga-Ga	108	5.74
0.25	Ga-Ga-Al-Ga	108	5.74
0.50	Al-Ga-Ga-Al	79	6.72
0.50	Ga-Al-Al-Ga	79	6.72
0.50	Al-Ga-Al-Ga	75	6.41
0.50	Al-Al-Ga-Ga	122	6.79
0.75	Al-Al-Ga-Al	54	7.40
0.75	Al-Al-Al-Ga	54	7.40
1.00	Al-Al-Al-Al	0	8.88

octahedral and tetrahedral are next to each other along the  $\mathbf{b}$ -direction, while in the other case, there is Ga in between them. We can see that both of these have an energy of formation in between the fully tetrahedral or fully octahedral one but are still slightly different. Also, the energy cost of moving one Al from an octahedral to a tetrahedral site is not equal to half the energy for moving two of them. This again indicates that other aspects in the Al distribution play a role in the energetics, such as how close the Al containing octahedra or tetrahedra are to each other.

In the corundum structure, we have only octahedral sites but nonetheless we can define different sites in the unit cell and consider the effects of which ones are occupied by Al or Ga. The differences in energy of formation as well as band gap between the different configurations are much smaller in this case. The only exception is the case of two Ga atoms next to each other in the 50 % case, which has a 43 meV/formula unit higher energy. This may be because the two larger atoms are next to each other causes more distortion in the structure.

From Fig. 4.2, we can see that the  $(\text{Al}_x\text{-Ga}_{1-x})_2\text{O}_3$  prefers to be in the monoclinic phase up to 70% Al concentration and the corundum phase thereafter. This however corresponds to the assumption that at each alloy composition the Al distribution is relaxed so the Al find their lowest energy configuration. If a random occupation would occur, modeled by the average energies of each possible configuration in the 10 atom cell the dotted lines are obtained in Fig. 4.2. Under that assumption the crossing to corundum phase would occur at lower concentration of Al. Nonetheless, from a thermodynamic point of view when comparing the relative stability of the two structures on the basis of energy, the assumption of minimizing the energy among different configurations is the more natural assumption. Since the total energy differences between the different configurations in Fig. 4.2 is of order 0.1 eV/formula unit, the Boltzmann factors for the higher energy configurations with tetrahedral Al occupations would be about  $e^{-1} = 0.37$  for a growth temperature of 1200K. This means

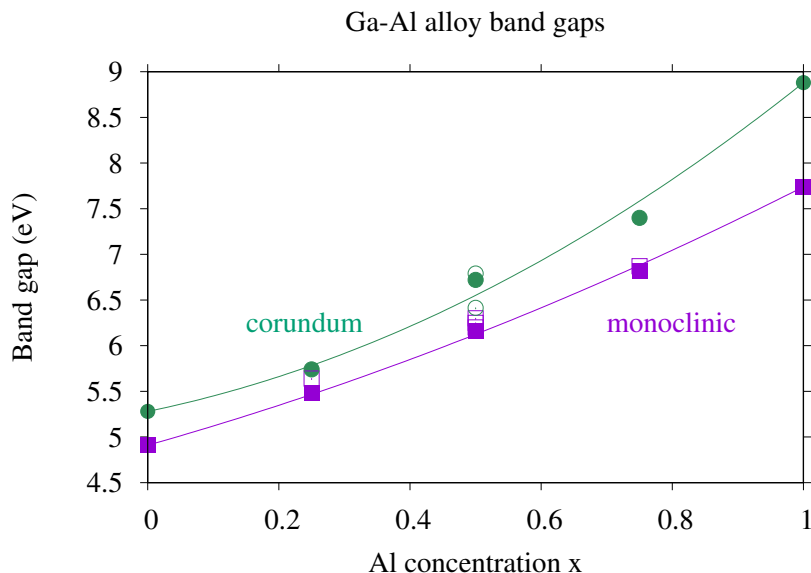


Figure 4.3: Direct band gap for the alloys as function of composition for each of the crystal structures. The solid symbols correspond to the lowest energy structure. The lines are a fit to these points with the parabolic equation defining the bowing coefficient. The open symbols to different configurations as detailed in Table 4.1.

the higher energy configurations are not expected to make a sizable contribution to the energy of formation.

### 4.4.3 Band gaps

Next, we consider the band gaps as function of concentration in each phase in Fig. 4.3. In this plot we show the band gap in the alloy configuration with the lowest energy of formation as solid symbols and the line is interpolated through them. We can see that the gaps are systematically higher in the  $\alpha$  than in the  $\beta$  structure but the difference increase with Al-concentration  $x$ . The band gaps do not vary linearly but the amount of band gap bowing is moderately small. Using the usual bowing equation  $E_g(x) = xE_g^{Al} + (1-x)E_g^{Ga} - bx(1-x)$ , the bowing coefficient  $b$  is  $0.8 \pm 0.1$  eV for the  $\beta$ -phase, and  $2.1 \pm 0.3$  eV for the  $\alpha$ -phase by fitting this equation to the data points for the lowest total energy configuration.

Next we consider the band gap differences for different Al sites reported in Table



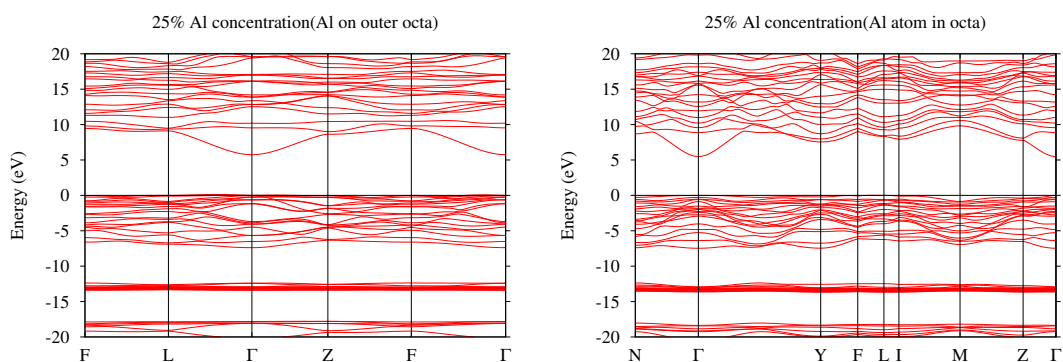


Figure 4.6: Band structures of  $(Al_xGa_{1-x})_2O_3$  for 25% Al concentration in: (a)  $\alpha$ -phase and (b)  $\beta$ -phase.

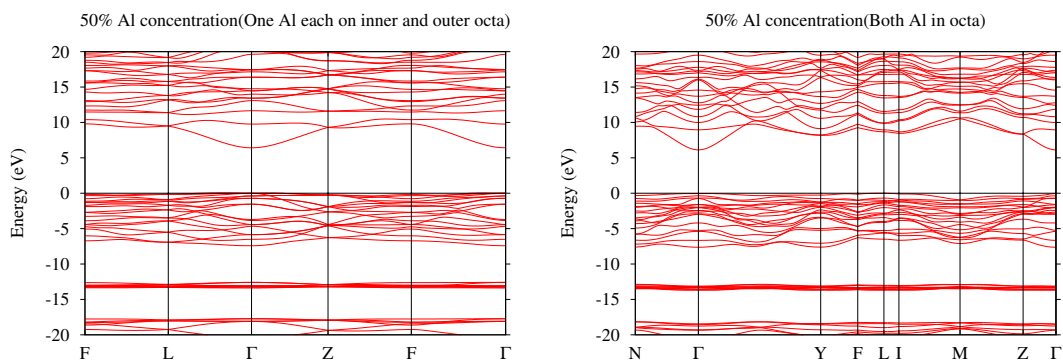


Figure 4.7: Band structures of  $(Al_xGa_{1-x})_2O_3$  for 50% Al concentration in: (a)  $\alpha$ -phase and (b)  $\beta$ -phase.

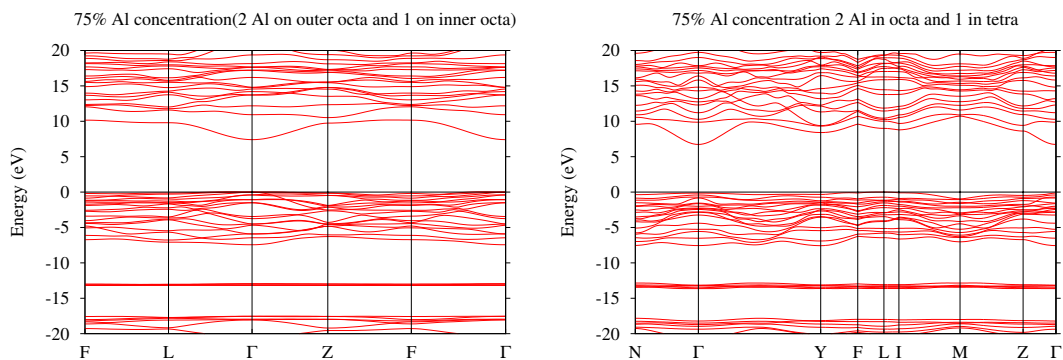


Figure 4.8: Band structures of  $(Al_xGa_{1-x})_2O_3$  for 75% Al concentration in: (a)  $\alpha$ -phase and (b)  $\beta$ -phase.

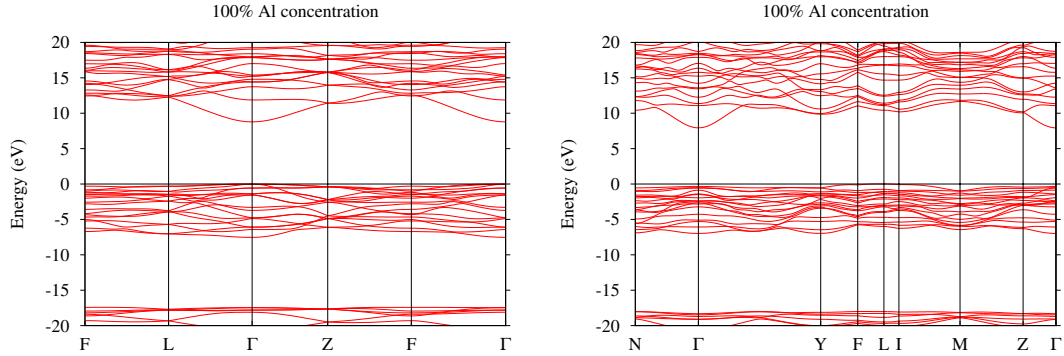


Figure 4.9: Band structures of  $(Al_xGa_{1-x})_2O_3$  for 100% Al concentration in: (a)  $\alpha$ -phase and (b)  $\beta$ -phase.

Thus the band gaps differ only very slightly depending on the precise configuration. This is even more so for the corundum structure. Hence the band gap bowings in Fig.4.3 obtained from the minimum energy configuration are adequate and a more random distribution will not lead to significantly larger or smaller bowing. Even when assuming completely random, non-equilibrium distribution of the Al, the band gaps will at most differ by 0.1 eV.

For completeness sake, the full band structures of  $(Al_xGa_{1-x})_2O_3$  alloy for all Al concentrations in both  $\alpha$  and  $\beta$ -phase are presented in Figures 4.5, 4.6, 4.7, 4.8, and 4.9. These band structures are created for the lowest energy configurations of all possible configurations. From the figures, we can see that as the Al concentration goes up, the band gap goes up for both the phases although it's always slightly higher in the  $\alpha$ -phase throughout concentrations. Also, for all concentrations in the  $\beta$ -phase, the compound appears to have an indirect band gap with the VBM somewhere between the symmetry points, F and L. In the  $\alpha$ -phase however, the band gap remains direct for all concentrations. Noticeably, the bands around -13 eV are the Ga 3d related bands which are absent in the cases of pure  $Al_2O_3$  in either crystal structure.

Overall, our band gaps are in good agreement with those of Ref. [79] obtained using a hybrid functional with adjusted exact exchange fraction for the two end compounds. They are thus also in good agreement with the available experimental

data [79].

# Chapter 5

## Vibrational properties of $\text{ZnGeGa}_2\text{N}_4$

### 5.1 Introduction

$\text{ZnGeGa}_2\text{N}_4$  comes from a class of alloys formed by combining the group-III nitrides and the corresponding heterovalent II-IV- $\text{N}_2$  compounds. These alloys have been proposed to add flexibility to the nitride semiconductors by tuning their properties. Among the many possible combinations,  $\text{ZnGeGa}_2\text{N}_4$  happens to be an ordered compound at 50 % composition of two closely lattice matched nitrides, GaN and  $\text{ZnGeN}_2$ . This structure obeys the local octet rule which means that every N atom is surrounded by two Ga, one Zn, and one Ge atom. This ensure local charge neutrality. Owing to the fact that both GaN and  $\text{ZnGeN}_2$  are lattice matched and have almost identical band gap with a significant band offset of  $\sim 1$  eV, the alloy of these two nitrides presents an ideal candidate to tailor the properties of these semiconductors further. The details about different phases of  $\text{ZnGeN}_2$ , and their heterostructures with GaN are presented in the Introduction Chapter subsection 1.2. In this chapter, we investigate the vibrational properties of this novel compound and present the infrared(IR)

and Raman spectra which may be useful in further understanding of the material and the class of alloys, in general. A group theoretical analysis, phonon frequencies and related Born effective charges, dielectric constants, infrared oscillator strengths and Raman tensors, are presented. Polarized infrared and Raman spectra for different scattering geometries are presented as well as the phonon band structure and density of states.

## 5.2 Computational method

The calculations are done using Density Functional Perturbation Theory (DFPT)[59, 60] using the plane-wave pseudopotential method as implemented in the ABINIT code [39]. Specifically, we here choose the Hartwigsen-Goedecker-Hutter pseudopotentials[82] The energy cutoff used is 80 Hartree, which was tested first to give converged results. For the Brillouin zone integration or charge densities and total energy a  $4 \times 4 \times 4$   $\mathbf{k}$ -point mesh is used. A first set of phonon calculations are done at the  $\Gamma$ -point. These are sufficient to determine the infrared absorption and reflection (IR) spectra as well as the Raman spectra assuming momentum conservation and using that visible and infrared light has negligible momentum compared to the Brillouin zone size. As has been observed in the past, [85] the Local Density Approximation (LDA) often provides higher accuracy phonons than the Generalized Gradient Approximation (GGA) in the Perdew-Burke-Ernzerhof (PBE) parametrization, [86] although a newer PBEsol is promising for both phonons and lattice constants. Here we do not focus on a comparison of different functionals. At present no experimental data are available so this would seem to be premature and the LDA has been found usually to be adequate for predicting the phonon properties. We here use the LDA based on the Ceperley-Alder parametrization.[87]

For the phonon densities of states and phonon band structures, we use the ap-

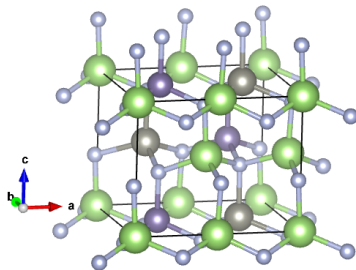


Figure 5.1: Crystal structure of ZnGeGa<sub>2</sub>N<sub>4</sub> in the  $Pmn2_1$  spacegroup.

proach described in Ref. [60] of separating the short range part of the force constant from the long-range dipole part as a way to interpolate to a finer mesh of  $\mathbf{k}$ -points for the phonon density of states calculations and for a fine set of  $\mathbf{k}$ -points along symmetry lines. A mesh of  $10 \times 10 \times 10$  was used for the phonon DOS integration.

## 5.3 Results

### 5.3.1 Group theoretical analysis and crystal structure

The unit cell of the  $Pmn2_1$  structure contains 16 atoms, 4 Ga, 2 Zn, 2 Ge, 4 N<sub>Ga</sub>, 2 N<sub>Zn</sub> and 2 N<sub>Ge</sub>, where the subscript means the cation the N sits on top of. The lattice constant and reduced coordinates were optimized within LDA and are given in Table 5.1. The crystal structure is shown in Fig. 5.1.

In total there are 48 degrees of freedom. The Zn and Ge and their respective N atoms on top are all in Wyckoff  $2a$  positions which lie in the ordinary  $m$  mirror planes, which are  $yz$  planes. The Ga and N<sub>Ga</sub> are in  $4b$  Wyckoff positions, which is the most general type of position. The point group is  $C_{2v}$ , the two-fold rotation screw axis is along the  $z$ -axis with  $z$  chosen along  $\mathbf{c}$ . The  $xz$  mirror plane  $n$  is a glide mirror-plane. The character group is given in Table 5.2.

Using standard group theoretical procedure, applied to the  $x, y, z$  displacements

Table 5.1: Lattice constant (in Å) and reduced coordinates. The Wyckoff positions are indicated with each atom type.

Lattice constants	$a$	$b$	$c$
	6.380	5.520	5.180
Reduced coordinates	$x$	$y$	$z$
Ga (4b)	0.000	-0.002	0.000
N <sub>Ga</sub> (4b)	-0.015	0.000	0.376
Zn (2a)	0.250	0.830	0.500
N <sub>Zn</sub> (2a)	0.250	0.816	0.891
Ge (2a)	0.750	0.838	0.500
N <sub>Ge</sub> (2a)	0.750	0.850	0.857

Table 5.2: Character table of  $C_{2v}$ .

irrep	$E$	$C_{2z}$	$m_{xz}$	$m_{yz}$	basis function
$a_1$	1	1	1	1	$z$
$a_2$	1	1	-1	-1	$xy$
$b_1$	1	-1	1	-1	$x$
$b_2$	1	-1	-1	1	$y$

of each type of Wyckoff position, we find that the 48 atomic displacement degrees of freedom build a representation, which can be decomposed into three translations (corresponding to  $a_1$ ,  $b_1$ ,  $b_2$  irreducible representations) and the following set of 45 vibrational modes:

$$\Gamma^{vib} = 13a_1 \oplus 10a_2 \oplus 9b_1 \oplus 13b_2. \quad (5.1)$$

In fact, the  $x, y, z$  displacements of each  $2a$  Wyckoff position leads to  $2a_1 \oplus a_2 \oplus b_1 \oplus 2b_2$  and each  $4b$  Wyckoff position leads to  $3a_1 \oplus 3a_2 \oplus 3b_1 \oplus 3b_2$  as irreducible representations. Of these modes, the  $a_1$ ,  $b_1$  and  $b_2$  are infrared active and show a LO-TO splitting for electric fields along  $z = c$ ,  $x = a$ ,  $y = b$  and all modes are Raman active. More precisely, the Raman tensors are of the form

$$\begin{aligned}
 & \begin{pmatrix} a & . & . \\ . & b & . \\ . & . & c \end{pmatrix}, & \text{for } a_1, \\
 & \begin{pmatrix} . & d & . \\ d & . & . \\ . & . & . \end{pmatrix}, & \text{for } a_2, \\
 & \begin{pmatrix} . & . & e \\ . & . & . \\ e & . & . \end{pmatrix}, & \text{for } b_1, \\
 & \begin{pmatrix} . & . & . \\ . & . & f \\ . & f & . \end{pmatrix}, & \text{for } b_2.
 \end{aligned}
 \tag{5.2}$$

Based on the form of the Raman tensors, one can deduce a set of scattering geometries which would allow one to measure all possible modes and all possible Raman tensor elements. These are described for all possible point groups in <https://www.cryst.ehu.es/cgi-bin/cryst/programs/nph-polarizationselrules>. A scattering geometry is specified by  $\mathbf{k}_i(\mathbf{e}_i\mathbf{e}_o)\mathbf{k}_o$ , where  $\mathbf{k}_i$  is the incoming wave vector,  $\mathbf{k}_o$  is the scattered wave vector and the corresponding polarizations are  $\mathbf{e}_i$ ,  $\mathbf{e}_o$ . Applied to the present group, a complete set of relevant scattering geometries, for which we will provide simulated spectra in Sec. 5.3.4 is as follows.

For parallel incident and scattered light polarizations, the only allowed modes are  $a_1$ . If in addition the wave vectors are along  $z$  and  $-z$  for backscattering geometry, (or  $z$  and  $z$  in transmission) then the modes measured are LO modes,  $a_{1L}$ , whereas

otherwise they are TO modes  $a_{1T}$ . Depending on the polarization being along  $x$ ,  $y$ , or  $z$  one would measure the  $a$ ,  $b$  or  $c$  tensor elements defined in Eq.(5.2) but one needs to distinguish the transverse,  $a_T$ ,  $b_T$ ,  $c_T$  and longitudinal  $a_L$ ,  $b_L$  mode Raman tensor elements. Note that  $c_L$  does not appear because  $a_1$  modes are only longitudinal if  $\mathbf{k}_i \parallel \hat{\mathbf{z}}$ , and  $\mathbf{k}_o \parallel \hat{\mathbf{z}}$ , but obviously, the polarizations can then not be along  $z$ . For crossed polarizers with polarizations  $x, y$  and light incident along  $z$  one would measure  $a_2$  modes. Likewise,  $b_1$  modes will be measured in a  $\mathbf{k}_i(\mathbf{e}_i\mathbf{e}_o)\mathbf{k}_o = y(xz)\bar{y}$  geometry and  $b_2$  modes in the  $x(yz)\bar{x}$  geometry. In both cases, these correspond to transverse modes. In order to detect  $b_{1L}$  or  $b_{2L}$  modes one would need a set up with orthogonal incoming and scattered wave vectors and in that case both longitudinal and transverse modes would be active. For example, in  $y(xz)x$  geometry or  $z(xz)x$  one would measure both  $b_{1T}$  and  $b_{1L}$  modes. Similarly, to measure  $b_{2L} + b_{2T}$  one could use  $x(yz)y$  or  $z(yz)y$  geometry.

### 5.3.2 Phonon frequencies and related results

The phonon frequencies at  $\Gamma$  are given in Table 5.3. Corresponding to the light propagating along  $\mathbf{z}$ ,  $\mathbf{x}$  or  $\mathbf{y}$ , the LO-TO splittings are observed for  $a_1$ ,  $b_1$  and  $b_2$  modes, respectively. Below we will refer to specific modes of each irreducible representation by adding a superscript ordered from low to high frequency, e.g.  $\omega(b_{1T}^1) = 174.76 \text{ cm}^{-1}$ . From Table 5.3, we can observe that the splittings are minute for the first few modes. However, the splittings get larger for the higher frequency modes. This is because the low energy modes are essentially folded acoustic modes of the underlying wurtzite lattice, while the higher frequency modes are optical modes corresponding to bond stretches between anions (N) and cations and therefore have a strong dipole character. The larger LO-TO splittings are also correlated with stronger oscillator strengths for infrared absorption. Since the  $a_2$  modes behave like the basis function  $xy$  they are not subject to LO-TO splitting. One may also observe that each TO phonon mode

Table 5.3: Phonon frequencies in  $Pmn2_1$  ZnGeGa<sub>2</sub>N<sub>4</sub> in cm<sup>-1</sup> labeled by irreducible representation in the column heading.

$a_2$	$b_{1T}$	$b_{1L}$	$b_{2T}$	$b_{2L}$	$a_{1T}$	$a_{1L}$
134.18	174.76	174.94	161.65	161.66	135.84	135.85
136.80	185.34	185.46	183.66	183.76	176.28	176.29
176.50	232.81	232.89	196.66	197.26	198.70	199.28
219.39	276.85	280.82	263.86	264.25	243.91	244.54
255.19	499.81	516.76	308.55	309.45	291.14	292.79
473.63	558.18	591.71	327.06	327.09	305.25	305.40
537.72	592.09	619.21	485.31	506.29	480.30	480.33
594.27	628.29	662.1	510.99	539.24	500.64	547.80
654.59	674.41	730.37	555.72	579.74	548.97	563.61
673.74			593.16	634.69	585.96	636.26
			674.77	696.42	657.88	674.39
			698.72	705.95	693.77	699.46
			717.37	749.64	699.57	749.50

of a given symmetry is followed by an LO before the next TO phonon occurs. This is a general rule obeyed by any crystal with at least orthorhombic symmetry,[88] but not for monoclinic symmetry. We note that this follows from general considerations of the phonon related  $\varepsilon$  and  $\varepsilon^{-1}$  in a Lorentz oscillator model. However, it does not mean that the eigenvectors of the TO-LO pairs constructed in this way are necessarily close to each other.

### 5.3.3 Infrared spectra

Besides inelastic neutron scattering, which allows one to measure complete phonon spectra, the most readily available methods to obtain information on the phonons are infrared absorption and Raman spectroscopy. In this section, we present our simulated infrared spectra. These are obtained from calculating the contribution of phonons to the dielectric response function in terms of the classical Lorentz oscillator model. Within DFPT, the oscillator strengths can be obtained directly from the phonon eigenvectors and the Born effective charges, which describe the coupling of

Table 5.4: Born effective charge tensor elements ( in units  $|e|$ ) for the atom of each type given in Table 5.1, indicated by the column. These local tensor elements transform between symmetry related atoms as indicated by the irreducible representation label.

Components	irrep	atom $\kappa$					
		Ga	Zn	Ge	N <sub>Ga</sub>	N <sub>Zn</sub>	N <sub>Ge</sub>
$Z_{\kappa xx}^*$	$a_1$	2.667	1.930	3.012	-2.577	-2.543	-2.580
$Z_{\kappa yy}^*$	$a_1$	2.678	1.838	3.198	-2.580	-2.927	-2.307
$Z_{\kappa zz}^*$	$a_1$	2.784	2.008	3.219	-2.669	-2.427	-2.992
$Z_{\kappa xy}^*$	$a_2$	-0.094	0.000	0.000	-0.156	0.000	0.000
$Z_{\kappa yx}^*$	$a_2$	0.021	0.000	0.000	-0.260	0.000	0.000
$Z_{\kappa xz}^*$	$b_1$	0.030	0.000	0.000	0.183	0.000	0.000
$Z_{\kappa zx}^*$	$b_1$	-0.086	0.000	0.000	0.189	0.000	0.000
$Z_{\kappa yz}^*$	$b_2$	-0.008	0.045	-0.091	-0.018	0.059	-0.094
$Z_{\kappa zy}^*$	$b_2$	0.014	0.013	0.014	0.006	0.067	-0.098

the vibrational modes to an electric field and are obtained as a mixed derivative of the total energy vs. a static electric field and an atomic displacement,[60] given by

$$Z_{\kappa\beta\alpha}^* = \frac{\partial^2 E_{tot}}{\partial u_{\kappa\alpha} \partial E_\beta} = V \frac{\partial P_\beta}{\partial u_{\kappa\alpha}} = \frac{\partial F_{\kappa\alpha}}{\partial E_\beta}, \quad (5.3)$$

where  $P_\beta$  is the macroscopic polarization,  $V$  the unit cell volume and  $u_{\kappa\alpha}$  the displacement of atom  $\kappa$  in direction  $\alpha$ , which, for a  $\mathbf{q} = 0$  mode, is the same in each unit cell.  $F_{\kappa\alpha}$  is the force on the atom  $\kappa$  in direction  $\alpha$  and  $E_\beta$  is the electric field component. Atomic units defined by  $e = 1, \hbar = 1, m_e = 1$ , with  $e$  the elementary charge and  $m_e$  the free electron mass, are used throughout the equations. The oscillator strength is then given by

$$S_{n,\alpha\alpha} = \left| \sum_{\kappa,\alpha'} Z_{\kappa,\alpha\alpha'}^* U_n(\kappa, \alpha') \right|^2, \quad (5.4)$$

where  $Z_{\kappa,\alpha\alpha'}^*$  are the Born effective charge tensor components given in Table 5.4,  $U_n(\kappa, \alpha')$  are the eigenvectors for each of the modes  $n$  at  $\mathbf{q} = 0$  and,  $\kappa$  refers to the

atom label. The  $U_n(\kappa, \alpha)$  are the eigenvectors of

$$\sum_{\kappa'\alpha'} [M_\kappa \delta_{\kappa\kappa'} \delta_{\alpha\alpha'} \omega_n^2 - K_{\kappa\alpha, \kappa'\alpha'}] U_n(\kappa', \alpha') = 0, \quad (5.5)$$

with  $M_\kappa$  the mass of atom  $\kappa$  and  $K_{\kappa\alpha, \kappa'\alpha'}$  the force constant matrix at  $\mathbf{q} = 0$ . The eigenvectors are normalized as

$$\sum_{\kappa\alpha} U_n(\kappa, \alpha)^* M_\kappa U_m(\kappa, \alpha) = \delta_{nm}. \quad (5.6)$$

The eigenvectors or mode eigendisplacements for each mode are presented in Appendix A. Note that because of the orthorhombic symmetry only diagonal elements of the tensorial quantity  $S_{n,\alpha\beta}$  are non-zero. They are listed in Table 5.5. One can see from this table, that the higher frequency modes tend to have higher oscillator strengths. This is because they correspond to bond stretches and thus have a significant dipole moment associated with them. The lower modes correspond to vibrations of groups of atoms relative to each other or modes that do not have such a clear dipole character. As already mentioned, this is directly related to the size of the LO-TO splitting.

The frequency dependent dielectric function in the region below the band gap is given by

$$\varepsilon_{\alpha\alpha}(\omega) = \varepsilon_{\alpha\alpha}^\infty + \frac{4\pi}{V} \sum_n \frac{S_{n,\alpha\alpha}}{\omega_n^2 - \omega^2 - i\Gamma_n\omega}, \quad (5.7)$$

where  $\omega_n$  are the phonon frequencies and  $\Gamma_n$  is a damping factor. The first term  $\varepsilon^\infty$ , usually referred to as the high-frequency dielectric constant, is the  $\omega \rightarrow 0$  limit of the electronic only part of the dielectric function, in other words the contribution from all the inter-band optical transitions, which, in the present material, start in the UV region. It is calculated in the DFPT framework as the adiabatic response to a static electric field in the  $x$ ,  $y$ ,  $z$  directions. Because of the orthorhombic symmetry, it is

Table 5.5: Oscillator strength tensor elements for each mode of a given symmetry in order of increasing frequency and in atomic units,  $e^2/m_e$ . For each irreducible representation given in parenthesis, only the indicated diagonal component of  $S_{n,\alpha\alpha}$  defined in Eq. 5.4, is non-zero as indicated in the column heading.

$xx$ ( $b_1$ )	$yy$ ( $b_2$ )	$zz$ ( $a_1$ )
$1.38 \times 10^{-6}$	$7.77 \times 10^{-8}$	$4.40 \times 10^{-8}$
$9.67 \times 10^{-7}$	$8.90 \times 10^{-7}$	$1.06 \times 10^{-7}$
$8.22 \times 10^{-7}$	$5.43 \times 10^{-6}$	$5.64 \times 10^{-6}$
$5.11 \times 10^{-5}$	$5.09 \times 10^{-6}$	$7.84 \times 10^{-6}$
$7.75 \times 10^{-4}$	$1.49 \times 10^{-5}$	$2.54 \times 10^{-5}$
$1.41 \times 10^{-3}$	$6.33 \times 10^{-7}$	$2.21 \times 10^{-6}$
$1.30 \times 10^{-5}$	$1.44 \times 10^{-3}$	$3.30 \times 10^{-6}$
$1.43 \times 10^{-4}$	$2.29 \times 10^{-4}$	$1.94 \times 10^{-3}$
$1.15 \times 10^{-4}$	$2.98 \times 10^{-4}$	$2.05 \times 10^{-5}$
	$2.17 \times 10^{-4}$	$4.12 \times 10^{-4}$
	$2.62 \times 10^{-4}$	$1.39 \times 10^{-4}$
	$1.38 \times 10^{-5}$	$2.04 \times 10^{-4}$
	$8.38 \times 10^{-5}$	$4.42 \times 10^{-6}$

also a diagonal tensor,  $\varepsilon_{\alpha\alpha}^\infty$ . The values of these tensor elements are given in Table 5.6. They are related to the anisotropic indices of refraction in the visible region at a frequency with  $\hbar\omega$  well below the band gap energy but far enough above the highest phonon frequencies, before the dispersion will bend the  $\varepsilon(\omega)$  down. The values of  $n_{\alpha\alpha} = \sqrt{\varepsilon_{\alpha\alpha}^\infty}$  are given in Table 5.7 for convenience.

The static dielectric constant  $\varepsilon_{\alpha\alpha}^0$  is the value obtained by taking the  $\omega \rightarrow 0$  limits of Eq.(5.7) and applies for frequencies well below the lowest phonon frequency. They are also included in Table 5.6. There is actually another contribution at even lower frequencies which is due to the piezoelectric response, which leads to strain in response to an applied electric field and the strain in turn leads to an induced polarization, but this contribution is here not included, so our value corresponds to clamped lattice vectors or unit cell shape.

Please note that unlike the oscillator strength and susceptibility or dielectric function, which are all *global* quantities, the Born effective charge tensors are *local* quan-

Table 5.6: High-frequency and static dielectric tensor components.

$\epsilon_{xx}^\infty$	$\epsilon_{yy}^\infty$	$\epsilon_{zz}^\infty$	$\epsilon_{xx}^0$	$\epsilon_{yy}^0$	$\epsilon_{zz}^0$
5.7825	5.830	5.893	10.223	10.626	11.008

Table 5.7: The indices of refraction.

$n_{xx}$	$n_{yy}$	$n_{zz}$
2.405	2.4145	2.4275

tities at particular sites in the unit cell. This implies that they only have the local site symmetry of the Wyckoff site, which for site  $2a$  is only a mirror plane and for site  $4b$  is no symmetry at all. They are thus not required to be diagonal or symmetric but still obey the sum-rule  $\sum_{\kappa} Z_{\kappa,\alpha\alpha'}^* = 0$  for each  $\alpha, \alpha'$ . For the diagonal elements, the  $Z_{\kappa,\alpha\alpha}^*$  have the same sign on each of the symmetry related atoms and thus it is only after summing over all types of atoms that cancellation takes place, balancing the cation and anion charges. For the off-diagonal elements they sum to zero for each type of atom separately. In fact, while the Ga and  $N_{\text{Ga}}$  which are on  $4b$  sites can have all off-diagonal elements non-zero, the Zn, Ge and their corresponding  $N_{\text{Zn}}, N_{\text{Ge}}$  still are required by symmetry to have zero  $xy$  and  $xz$  elements but can have non-zero  $yz$  elements because they are located on the  $yz$  mirror plane. These off-diagonal components sum to zero when adding the contributions of the symmetry related atoms of each type in the unit cell because the  $Z_{\kappa\beta\alpha}^*$  tensor element will change sign under the symmetry operation relating the two atoms according to the irreducible representation corresponding to  $\beta\alpha$ , which is  $a_2$  for  $xy$  or  $yx$ ,  $b_1$  for  $xz$  or  $zx$  and  $b_2$  for  $yz$  or  $zx$ . These irreducible representations are indicated in Table 5.4. The reason why the  $Z_{\kappa\beta\alpha}^* \neq Z_{\kappa\alpha\beta}^*$  is that the first index corresponds to the electric field component and the second to the atom displacement component involved in their definition, given in Eq.(5.3).

From the above defined  $\varepsilon(\omega)$  we can extract various related optical functions, in the infrared range. In particular, the optical absorption coefficient  $\alpha(\omega) = 2\omega\text{Im}[\varepsilon(\omega)]/n(\omega)$  and the reflectivity  $R(\omega) = |(\tilde{n}(\omega) - 1)/(\tilde{n}(\omega) + 1)|^2$  with  $\tilde{n} = n + i\kappa = \sqrt{\varepsilon}$  the complex index of refraction as well as the loss function  $-\text{Im}\{\varepsilon(\omega)^{-1}\}$  are the most closely related to the measurements. The zeros in the real part  $\text{Re}\{\varepsilon(\omega)\} = \varepsilon_1(\omega)$  and the peaks in the loss function indicate the LO mode frequencies, while the peaks in  $\text{Im}\{\varepsilon(\omega)\} = \varepsilon_2(\omega)$  give the TO modes. The reflectivity shows the typical *Reststrahlen* bands (RB) which jump to almost 100% reflectivity at the TO modes and fall back at the LO modes. Note that the absorption coefficient  $\alpha(\omega)$  can show features at both the TO and LO modes because of the possibility of a zero in the index of refraction.

The infrared spectra for the three polarizations are shown in Fig. 5.2. For each polarization  $z, x, y$  the corresponding irreducible mode  $a_1, b_1, b_2$  imaginary and real parts of  $\varepsilon(\omega)$  are shown in black solid and red dashed lines. The blue (green) solid lines show the reflectivity (loss function). The purple dashed line shows the absorption coefficient. In the low frequency region it is multiplied by the factor indicated to make these much lower intensity features visible. We note that the broadening or damping factors  $\Gamma_n$  were not calculated but just given some typical value. Calculating these damping factors would require including anharmonic terms and hence phonon-phonon scattering processes. In reality these broadening factors may be mode dependent but here the same value of  $\Gamma_n = 5 \text{ cm}^{-1}$  is applied to all modes.

We next discuss in some detail how these spectra relate to the data of Table 5.3. We start with the  $b_1$  modes or  $x$ -polarization. Although there are in principle nine  $b_1$  modes, at first sight, we see only five clearly distinguishable RBs. The first one is the one corresponding to mode  $b_{1T}^4$  at  $276.8 \text{ cm}^{-1}$ . This mode is indeed seen to have an oscillator strength of order  $10^{-5}$  in Table 5.5 compared to the lower ones which are 1-2 orders weaker but is itself rather weak compared to the ones above  $400 \text{ cm}^{-1}$ . To see the lower frequency modes better, we show the absorption coefficient multiplied

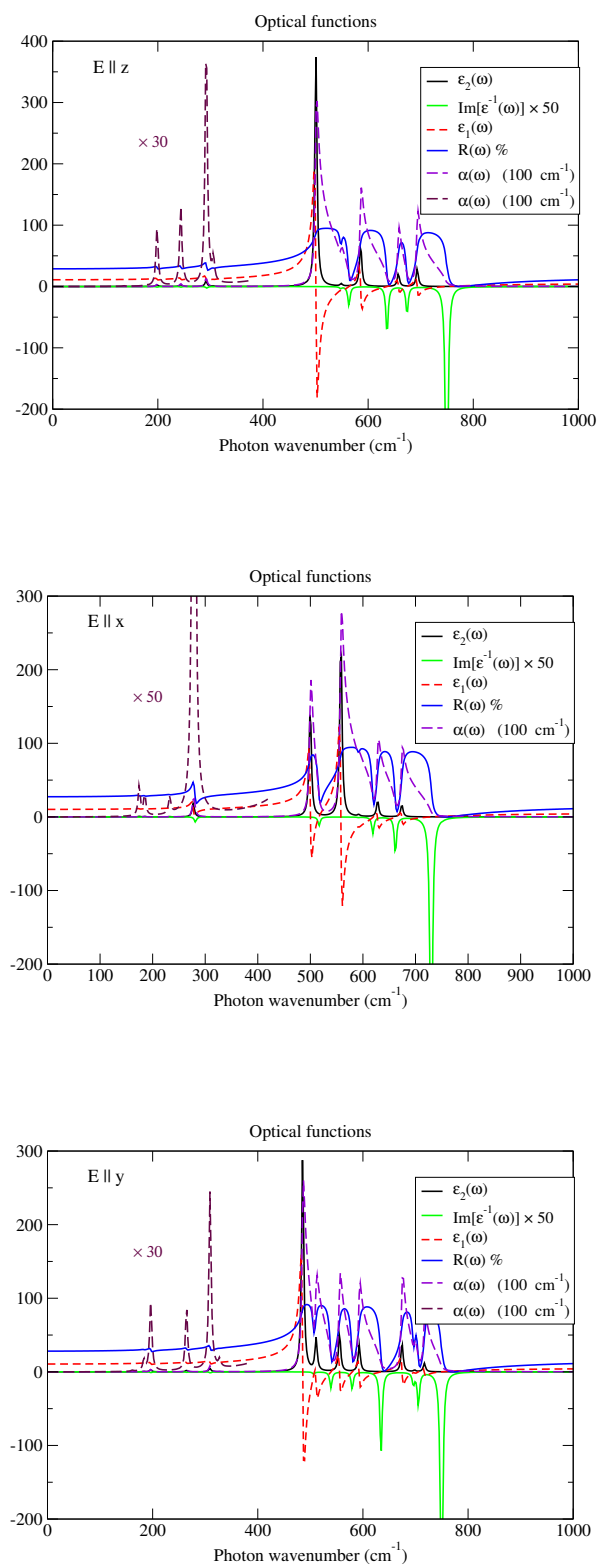


Figure 5.2: IR spectra for (a)  $a_1$  modes, (b)  $b_1$  modes and (c)  $b_2$  modes.

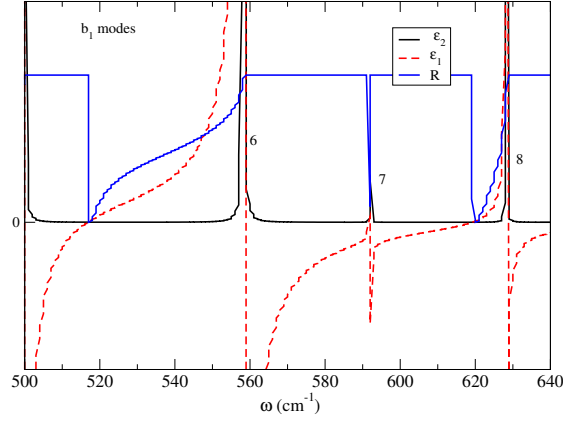


Figure 5.3: IR spectrum of  $b_1$  modes with very small  $\Gamma_n = 10^{-5} \text{ cm}^{-1}$  broadening zoomed in on region  $500 < \omega < 640 \text{ cm}^{-1}$  focused on modes 6-8. The  $y$ -scales have been arbitrary adjusted.

by a factor 50 separately in the region below  $400 \text{ cm}^{-1}$ . The next band correspond to the TO mode  $b_{1T}^5$  at  $499.81 \text{ cm}^{-1}$  and the corresponding LO one is at  $516.76 \text{ cm}^{-1}$ .

The next RB for mode  $b_{1T}^6$  starts at  $558.18 \text{ cm}^{-1}$  but it comes down only at  $619.21 \text{ cm}^{-1}$ . Table 5.5 shows that the  $b_{1T}^7$  mode at  $592.09 \text{ cm}^{-1}$  has much weaker oscillator strength of order  $10^{-5}$  and hence is hidden by the 6th mode RB. Looking only at the spectra and without knowledge of Table 5.5, which is essentially the situation the experimentalists would be confronted with, one could be tempted to associate the LO mode of  $619.21 \text{ cm}^{-1}$  with mode 6. One would then have missed one of the modes entirely. Upon closer inspection, the shape of the  $\varepsilon_1(\omega)$  in this energy region already shows that the zero crossing, which should have occurred at  $591.71 \text{ cm}^{-1}$ , is hidden simply because of the broadening. There is also a very small dip visible in the reflection spectrum, but one could easily imagine that additional experimental broadening could hide this feature. As shown in Fig. 5.3, when we recalculate these spectra with a much smaller (in fact un-physically small broadening of  $10^{-5} \text{ cm}^{-1}$  or less) we can see the the  $b_{1L}^6$  and  $b_{1T}^7$  modes clearly as a sharp dip in the reflectivity curve to almost zero and a peak in  $\varepsilon_2$ .

On the other hand, in view of the LO-TO rule, it is clearly not allowed to assume that the 591.71 cm<sup>-1</sup> LO mode would correspond to the 592.09 cm<sup>-1</sup> TO mode, even if rounded to one cm<sup>-1</sup> these appear to be the same and could have been just a mode with very weak LO-TO splitting below the error bar of the calculation. Indeed, associating the 558.18 cm<sup>-1</sup> TO mode with the 619.21 cm<sup>-1</sup> LO mode would violate the LO-TO rule.

The origin of the LO-TO rule is the alternation of poles in the dielectric and inverse dielectric function and follows from the analytical form of  $\varepsilon(\omega)$ , in other words from the Kramers-Kronig relations or causality, that each pole is followed by a zero before the next pole. On the other hand, from the first-principles computational point of view, the LO and TO set of modes for a given symmetry result from diagonalization of a different dynamical matrix, one including long-range forces and the other not. From that point of view, their eigenvectors need not be the same and the pairing of modes on a one-to-one basis is not obvious. In other words, the TO-LO rule which ensures a one-to-one pairing of TO to LO modes does not require that the eigenvectors of these corresponding modes are closely related. To analyze the correlation between TO and LO eigenvectors of corresponding mode numbers we calculate[89]

$$C_{nm} = \frac{1}{2} \sum_{\kappa, \alpha} [U_{\kappa\alpha}^{Tn} M_{\kappa} U_{\kappa\alpha}^{Lm} + U_{\kappa\alpha}^{Ln} M_{\kappa} U_{\kappa\alpha}^{Tm}]. \quad (5.8)$$

which for  $b_1$  modes gives

$$\begin{pmatrix}
 0.998 & -0.001 & 0.000 & 0.001 & 0.005 & 0.004 & -0.001 & -0.001 & -0.005 \\
 -0.001 & 0.999 & 0.000 & 0.000 & -0.004 & -0.003 & 0.002 & 0.001 & 0.005 \\
 0.000 & 0.000 & 0.999 & -0.002 & -0.004 & -0.003 & 0.001 & 0.001 & 0.004 \\
 0.001 & 0.000 & -0.002 & 0.995 & -0.035 & -0.026 & 0.008 & 0.007 & 0.035 \\
 0.005 & -0.004 & -0.004 & -0.035 & -0.881 & 0.212 & 0.098 & 0.119 & 0.176 \\
 0.004 & -0.003 & -0.003 & -0.026 & 0.212 & -0.122 & 0.708 & 0.205 & 0.324 \\
 -0.001 & 0.002 & 0.001 & 0.008 & 0.098 & 0.708 & 0.090 & -0.408 & 0.100 \\
 -0.001 & 0.001 & 0.001 & 0.007 & 0.119 & 0.205 & -0.408 & 0.347 & 0.584 \\
 -0.005 & 0.005 & 0.004 & 0.035 & 0.176 & 0.324 & 0.100 & 0.584 & -0.533
 \end{pmatrix}
 = C_{nm}^{b_1} . \tag{5.9}$$

Note that the eigenvectors at  $\mathbf{q} = 0$  are real, so no complex conjugate is needed. This shows that the first 4 TO-LO modes are almost perfectly correlated while from mode 5 and onward, the correlation between corresponding modes becomes poorer. In particular, mode  $b_{1T}^6$  is more correlated with  $b_{1L}^7$  than with its own LO mode.

For the  $a_1$  modes, there should be 13 modes, but we see only 4 RBs in the region

above  $400\text{ cm}^{-1}$  and one rather weak one near  $300\text{ cm}^{-1}$ . Inspection of the table of oscillator strengths shows that this must be mode  $a_{1T}^5$  at  $201.1\text{ cm}^{-1}$  with an oscillator strength of order  $10^{-5}$ . The modes number 6 and 7 again have weak oscillator strengths of order  $10^{-6}$ , so the first strong RB corresponds to mode 8 at  $500.6\text{ cm}^{-1}$  and coming down at  $563.6\text{ cm}^{-1}$  which however corresponds to  $a_{1L}^9$ . So again, looking at the spectra only, we apparently skipped a hidden mode with weak oscillator strength. We can see that the frequency of  $a_{1T}^9$  is close to that of  $a_{1L}^8$ . In the RB we just see a little dip near  $550\text{ cm}^{-1}$  which signals the hidden mode. Mode  $a_{1T}^{10}$  at  $585.9$  starts an RB ending at  $636.2\text{ cm}^{-1}$ . Mode  $a_{1T}^{11}$  corresponds to the onset of the RB at  $658.8\text{ cm}^{-1}$  is nicely isolated but the next RB starting at  $a_{1T}^{12}$  ends only at  $749.5\text{ cm}^{-1}$  which corresponds rather to  $a_{1L}^{13}$  with again a weak hidden mode at  $699.5\text{ cm}^{-1}$  in between.



Again, we see that from mode 8 onward, the correlations between corresponding TO and LO eigenvectors becomes small and in particular modes 8 and 9 have larger correlation with each other's eigenvectors than with themselves.

A similar analysis applies to the  $b_2$  modes. Here we see actually 6 clearly distinguishable RBs with corresponding peaks in  $\varepsilon_2(\omega)$  in the region above  $400 \text{ cm}^{-1}$  and one clear dip in the 5th band indicating another weaker mode. Even in the low frequency region we may see 3 small features in the reflectivity curve signaling the



### 5.3.4 Raman spectra

The Raman cross-section for the Stokes process (energy loss) for each mode is given by,[61]

$$\frac{dS}{d\Omega} = \frac{(\omega_0 - \omega_m)^4}{c^4} |\mathbf{e}_i \cdot \boldsymbol{\alpha}^m \cdot \mathbf{e}_o|^2 \frac{\hbar}{2\omega_m} (n_m + 1), \quad (5.12)$$

where  $\omega_0$  is the incident light frequency,  $\omega_m$  the mode frequency, and  $n_m$  is the boson occupation number  $n_m = [\exp(\hbar\omega_m/k_B T) - 1]^{-1}$ ,  $\mathbf{e}_i$  and  $\mathbf{e}_o$  refer to the incident and the scattered polarization directions and  $\boldsymbol{\alpha}^m$  is the second-rank Raman susceptibility tensor for mode  $m$  which is given by,

$$\alpha_{\alpha\beta}^m = \sqrt{V} \sum_{\kappa\gamma} \frac{\partial \chi_{\alpha\beta}}{\partial \tau_{\kappa\gamma}} U_m(\kappa\gamma), \quad (5.13)$$

in terms of  $U_m(\kappa\gamma)$ , the eigenvector of the  $m$ -th vibrational mode and the derivative of the susceptibility vs. atomic displacements. Given the Raman tensor, the Raman spectrum can be generated for any choice of incoming and scattered light polarizations. Therefore we first provide the full set of Raman tensor elements in Table 5.8. Whether the longitudinal or transverse modes are excited depends on the direction of the incoming and scattered wave vectors as explained in Sec. 5.3.1.

The spectra are simplest to interpret when the polarization vectors are along the crystallographic axes. Specific scattering geometries can be used to excite only modes of one irreducible representation at a time and measure a specific component of the Raman tensors as given in Eq.(5.2). These were already explained at the end of Sec.5.3.1. The Raman spectra for a complete set of backscattering geometries that would allow one to measure each of the TO modes and the  $a_2$  modes which are only Raman but not IR active, and their different tensor components as well as the  $a_{1L}$  LO modes are given in Figs. 5.4, 5.5, 5.6.

In Fig. 5.4 one can distinguish all 13 modes. Six of them occur for frequencies below 400 cm<sup>-1</sup>. However, some seem to be absent for particular polarizations. For

Table 5.8: Raman tensor components.

$a_1(TO)$ $a^T = \alpha_{xx}^T$	$a_1(TO)$ $b^T = \alpha_{yy}^T$	$a_1(TO)$ $c^T = \alpha_{zz}^T$	$a_1(LO)$ $a^L = \alpha_{xx}^L$	$a_1(LO)$ $b^L = \alpha_{yy}^L$	$a_1(LO)$ $c^L = \alpha_{zz}^L$
$-3.77 \times 10^{-4}$	$3.68 \times 10^{-4}$	$-6.24 \times 10^{-5}$	$-3.74 \times 10^{-4}$	$3.70 \times 10^{-4}$	$-6.50 \times 10^{-5}$
$1.84 \times 10^{-4}$	$-6.21 \times 10^{-4}$	$-3.16 \times 10^{-4}$	$1.84 \times 10^{-4}$	$-6.18 \times 10^{-4}$	$-3.22 \times 10^{-4}$
$-1.68 \times 10^{-4}$	$-2.12 \times 10^{-4}$	$4.51 \times 10^{-4}$	$-1.35 \times 10^{-4}$	$-1.91 \times 10^{-4}$	$4.15 \times 10^{-4}$
$-2.30 \times 10^{-4}$	$-5.29 \times 10^{-4}$	$4.48 \times 10^{-4}$	$-1.88 \times 10^{-4}$	$-5.06 \times 10^{-4}$	$4.12 \times 10^{-4}$
$5.18 \times 10^{-4}$	$3.69 \times 10^{-4}$	$2.32 \times 10^{-4}$	$4.52 \times 10^{-4}$	$3.47 \times 10^{-4}$	$3.49 \times 10^{-4}$
$6.25 \times 10^{-5}$	$3.05 \times 10^{-4}$	$8.72 \times 10^{-4}$	$6.74 \times 10^{-5}$	$3.04 \times 10^{-4}$	$8.31 \times 10^{-4}$
$3.35 \times 10^{-3}$	$-1.10 \times 10^{-3}$	$1.42 \times 10^{-3}$	$3.28 \times 10^{-3}$	$-1.16 \times 10^{-3}$	$1.53 \times 10^{-3}$
$-2.03 \times 10^{-3}$	$-1.58 \times 10^{-3}$	$2.78 \times 10^{-3}$	$-3.98 \times 10^{-3}$	$-5.37 \times 10^{-3}$	$4.70 \times 10^{-3}$
$-3.65 \times 10^{-3}$	$-5.65 \times 10^{-3}$	$-5.45 \times 10^{-3}$	$-1.51 \times 10^{-4}$	$-3.24 \times 10^{-3}$	$2.07 \times 10^{-3}$
$5.14 \times 10^{-5}$	$4.23 \times 10^{-3}$	$-1.68 \times 10^{-3}$	$1.75 \times 10^{-3}$	$-3.23 \times 10^{-3}$	$1.78 \times 10^{-3}$
$-4.00 \times 10^{-3}$	$9.93 \times 10^{-5}$	$1.31 \times 10^{-3}$	$-2.71 \times 10^{-3}$	$-1.73 \times 10^{-3}$	$1.13 \times 10^{-3}$
$7.64 \times 10^{-4}$	$-6.62 \times 10^{-4}$	$-3.01 \times 10^{-3}$	$-3.24 \times 10^{-3}$	$-3.49 \times 10^{-3}$	$-3.41 \times 10^{-3}$
$3.49 \times 10^{-3}$	$3.51 \times 10^{-3}$	$2.89 \times 10^{-3}$	$4.42 \times 10^{-3}$	$3.29 \times 10^{-3}$	$6.86 \times 10^{-3}$
$b_1(TO)$ $e^T = \alpha_{xz}^T$	$b_1(LO)$ $e^L = \alpha_{xz}^L$	$a_2$ $d = \alpha_{xy}$	$b_2(TO)$ $f^T = \alpha_{yz}^T$	$b_2(LO)$ $f^L = \alpha_{yz}^L$	
$-1.93 \times 10^{-4}$	$-1.08 \times 10^{-4}$	$2.77 \times 10^{-4}$	$-1.97 \times 10^{-4}$	$-1.97 \times 10^{-4}$	
$1.27 \times 10^{-5}$	$1.26 \times 10^{-5}$	$-2.86 \times 10^{-4}$	$-1.80 \times 10^{-4}$	$-1.81 \times 10^{-4}$	
$3.80 \times 10^{-4}$	$3.80 \times 10^{-4}$	$-7.13 \times 10^{-5}$	$1.15 \times 10^{-4}$	$1.26 \times 10^{-4}$	
$-1.19 \times 10^{-4}$	$-1.39 \times 10^{-4}$	$7.89 \times 10^{-4}$	$-1.50 \times 10^{-4}$	$-1.53 \times 10^{-4}$	
$7.18 \times 10^{-4}$	$-5.95 \times 10^{-5}$	$4.21 \times 10^{-4}$	$2.43 \times 10^{-4}$	$2.48 \times 10^{-4}$	
$1.53 \times 10^{-3}$	$-3.38 \times 10^{-4}$	$-8.97 \times 10^{-4}$	$1.16 \times 10^{-4}$	$1.14 \times 10^{-4}$	
$-1.14 \times 10^{-4}$	$4.24 \times 10^{-4}$	$2.14 \times 10^{-3}$	$7.19 \times 10^{-4}$	$1.38 \times 10^{-4}$	
$6.46 \times 10^{-4}$	$1.04 \times 10^{-3}$	$1.61 \times 10^{-3}$	$-2.41 \times 10^{-4}$	$6.17 \times 10^{-4}$	
$-3.37 \times 10^{-4}$	$2.90 \times 10^{-3}$	$-2.45 \times 10^{-3}$	$-6.63 \times 10^{-4}$	$2.58 \times 10^{-4}$	
		$3.34 \times 10^{-4}$	$6.89 \times 10^{-4}$	$1.04 \times 10^{-3}$	
			$-8.37 \times 10^{-4}$	$8.58 \times 10^{-4}$	
			$6.95 \times 10^{-4}$	$1.09 \times 10^{-3}$	
			$5.85 \times 10^{-4}$	$2.28 \times 10^{-3}$	

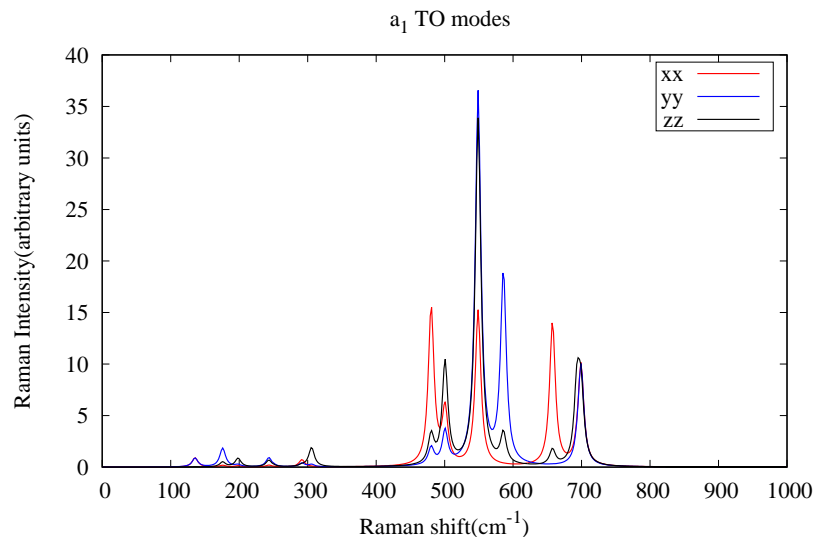


Figure 5.4: Raman spectra for  $a_{1T}$  modes for  $\bar{y}(xx)y$ ,  $\bar{x}(yy)x$  and  $\bar{x}(zz)x$  scattering geometries.

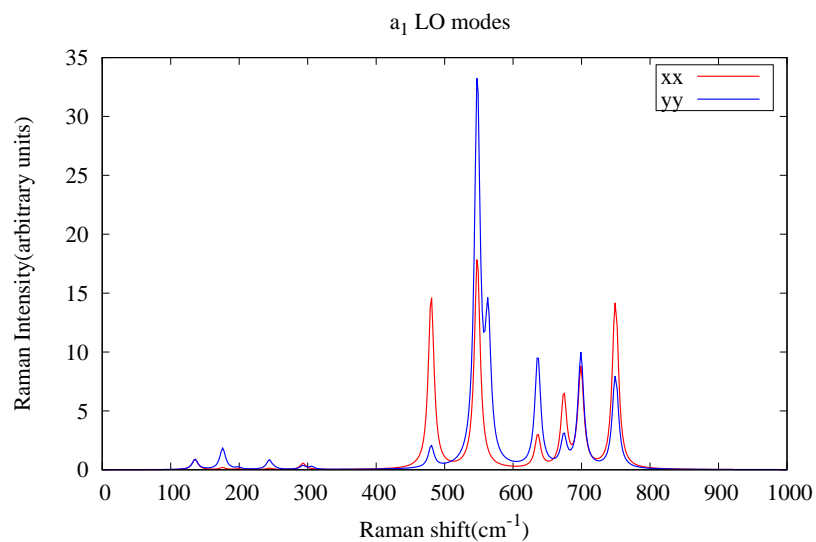


Figure 5.5: Raman spectra for  $a_{1L}$  modes for  $\bar{z}(xx)z$ ,  $\bar{z}(yy)z$  scattering geometries.

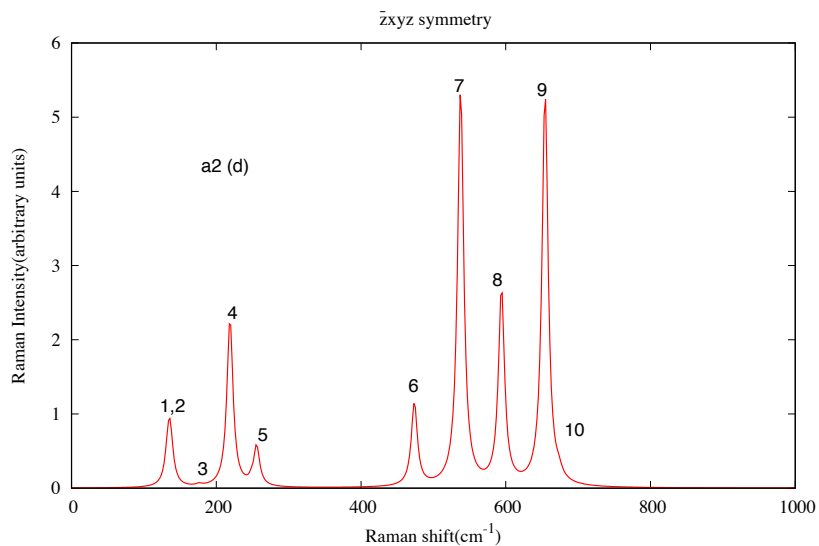


Figure 5.6: Raman spectra for  $\bar{z}(xy)z$  scattering geometry, giving the  $a_2$  modes with  $d$  tensor component.

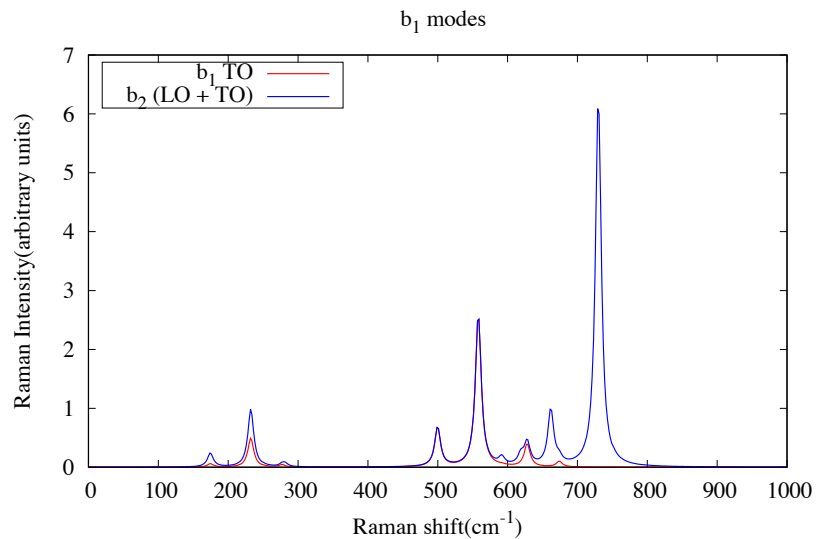


Figure 5.7: Raman spectra for  $\bar{y}(xz)y$  showing only  $b_{1T}$  modes and for  $y(xz)x$  scattering geometry, giving  $b_{1T} + b_{1L}$  modes.

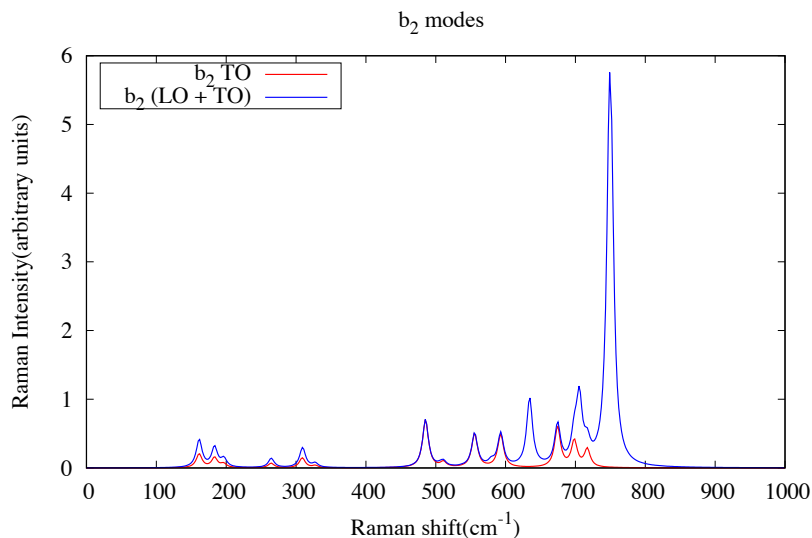


Figure 5.8: Raman spectra for  $\bar{x}(yz)x$  showing only  $b_{2T}$  modes and for  $x(yz)y$  scattering geometry, giving  $b_{2T} + b_{2L}$  modes.

example, the first peak has almost zero intensity for  $xx$  or  $zz$  polarization. Inspection of Table 5.8 shows that these modes indeed have very low Raman tensor components of order  $10^{-5}$ , while the strongest peaks have matrix elements of order  $10^{-3}$ . Please note that the intensity is proportional the tensor element modulo squared, thus this means a ratio of 4 orders of magnitude between the weakest and strongest modes. Modes 12 and 13 are very close to each other and mode 12 is only strong for  $zz$  polarization while 13 is strong for all three polarizations. Thus modes 12 and 13 are merged into one peak but its peak position is slightly shifted for  $zz$  compared to the other polarizations. Mode 11 is seen be very weak for  $yy$  polarization but is strongest for  $xx$  polarization. These observations can be verified to be consistent with Table 5.8. Thus to find all  $a_{1T}$  modes experimentally, it would be important to explore the three polarizations.

For the  $a_{1L}$  spectra, shown in Fig. 5.5, we can see modes 7-13 clearly for  $y$  polarization but mode 9 is very weak in  $xx$  polarization. Thus for the  $xx$  polarization

there appear to be only 6 peaks above 400 cm<sup>-1</sup>. Comparing now infrared with Raman spectra, we note that modes 7 and 9 which are quite weak in IR are strong in Raman spectra, in particular the TO mode  $a_{1T}^9$  is the strongest peak both for  $yy$  and  $zz$  polarization.

The  $a_2$  modes shown in Fig. 5.6 were labeled to show that modes 1 and 2 are too close together to be distinguished and mode 10 only shows up as a small shoulder. In Fig. 5.7 we show spectra for  $\bar{y}(xz)y$  backscattering geometry, displaying only the  $b_{1T}$  modes as red lines and for  $y(xz)x$  right-angle geometry displaying  $b_{1T} + b_{1L}$  modes as blue lines. In the low energy region we see only 3 peaks because the second mode at 185 cm<sup>-1</sup> has negligible Raman tensor component. Since these modes show very little LO-TO splitting, the  $b_{1T} + b_{1L}$  spectrum has about twice the intensity in this region as the  $b_{1T}$  one. In contrast, the next two peaks are clearly  $b_{1T}^5$  and  $b_{1T}^6$ . Mode  $b_{1L}^5$  at 516.7 cm<sup>-1</sup> has very weak intensity and is not seen. The highest two peaks clearly belong only to  $b_{1L}$ , while the shoulder at 674.4 cm<sup>-1</sup> right above the  $b_{1L}^8$  mode (662.1 cm<sup>-1</sup>) belongs to the  $b_{1T}$  spectrum. Similar results are shown for  $b_2$  modes in Fig. 5.8.

The above set of spectra all depend only on the Raman tensor elements modulo squared. However, the reader may notice that in Table 5.8 these matrix elements also have a sign. In order to reveal the sign one needs to look at a scattering geometry where more than one tensor element is at play so that their terms are added including the proper signs before taking the modulo squared. This can for instance be done by focusing on a single mode and mapping out the angular dependence of the polarization in a polar plot. As an example, consider an incoming wave with  $\mathbf{k}_i$  and  $\mathbf{k}_o$  both along  $z$  and polarization  $\mathbf{e}_i = \mathbf{e}_o = \hat{x} \cos \phi + \hat{y} \sin \phi$ . The Raman intensity will then be proportional to  $|a \cos^2 \phi + b \sin^2 \phi|^2$ . If  $a$  and  $b$  have the same sign this will give a “peanut shaped” pattern as function of angle  $\phi$  but if  $a$  and  $b$  have opposite signs, it will trace out a four-lobed polar plot. If  $a = b$  it would give a circular pattern. For

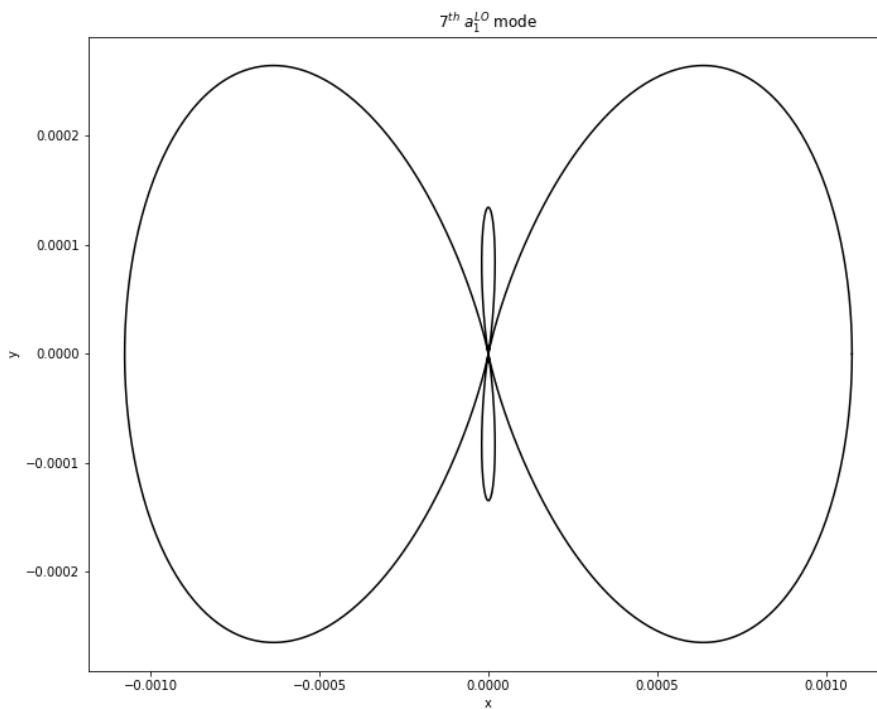


Figure 5.9: Polar plot for mode  $a_{1L}^7$  as function of angle  $\phi$  of  $\mathbf{e}_i$  with respect to  $x$ -axis (crystallographic  $\mathbf{a}$ -direction)  $\mathbf{e}_o \parallel \mathbf{e}_i$  and  $\mathbf{k}_{i/o}$  along  $z$  or  $\mathbf{c}$  are assumed.

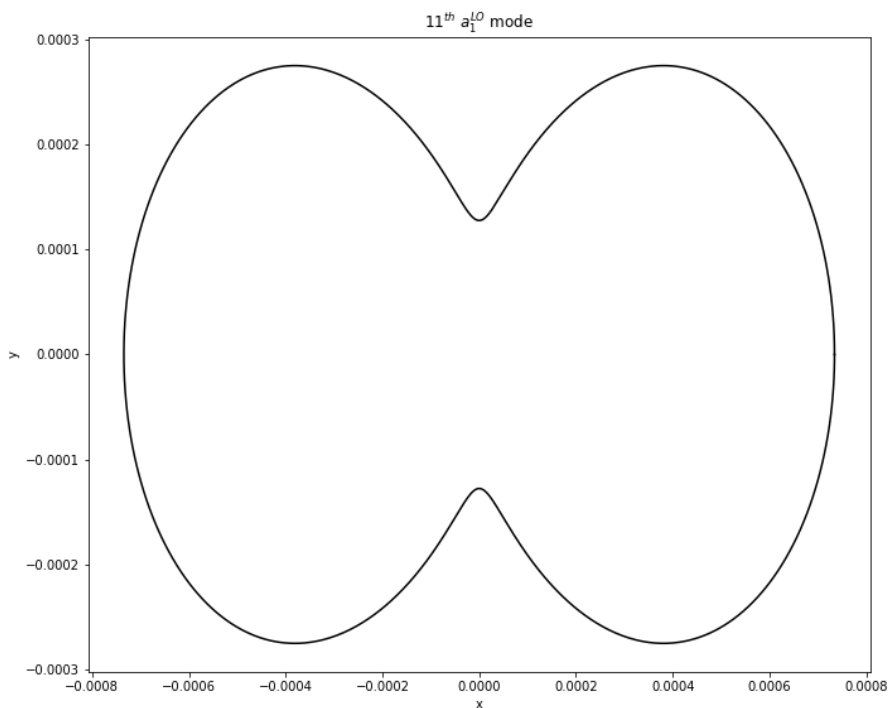


Figure 5.10: Polar plot for mode  $a_{1L}^{11}$  as function of angle  $\phi$  of  $\mathbf{e}_i$  with respect to  $x$ -axis (crystallographic  $\mathbf{a}$ -direction)  $\mathbf{e}_o \parallel \mathbf{e}_i$  and  $\mathbf{k}_{i/o}$  along  $z$  or  $\mathbf{c}$  are assumed.

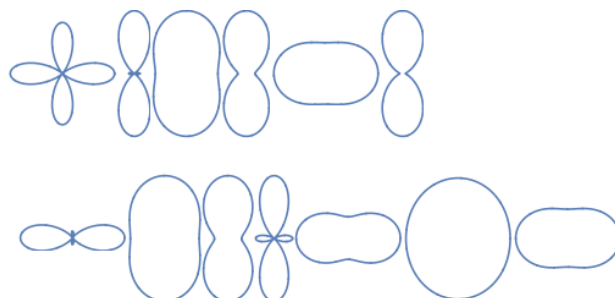


Figure 5.11: Polar plot shapes for all  $a_{1L}$  modes as function of azimuthal angle (about the  $c$ -axis) in the  $xy$ -plane with  $x$  horizontal,

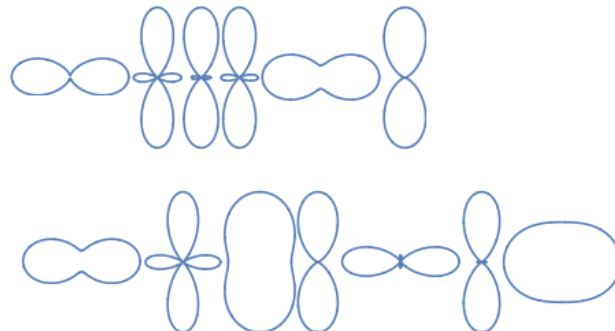


Figure 5.12: Polar plot shapes for all  $a_{1T}$  modes as function of azimuthal angle (about the  $b$ -axis) in the  $xz$ -plane with  $x$  horizontal,

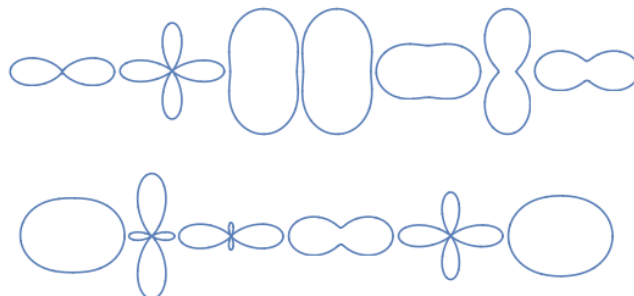


Figure 5.13: Polar plot shapes for  $a_{1T}$  modes as function of azimuthal angle (about the  $a$ -axis) in the  $yz$ -plane with  $y$  horizontal. In each case the plots correspond to the modes in order of increasing frequency as given in Table 5.3. Note that the size of each plot relative to the others is arbitrary, only the shape's aspect ratio has meaning.

example for mode  $a_{1L}^7$  we see that  $b^L$  and  $a^L$  have opposite signs and indeed the polar plot of this mode, shown in Fig. 5.9 shows a four-lobed shape. Because  $|a| > |b|$  it is more extended in the  $x$ -direction than the  $y$  direction. As another example, the angular pattern for mode  $a_{1L}^{11}$ , for which  $a$  and  $b$  have the same sign is shown in Fig. 5.10 and shows a peanut shape. In fact, Fig. 5.11 shows the polar plot angular shapes for all  $a_{1L}$  modes in order of increasing frequency. Similarly, the  $a_{1T}$ -modes as function of the azimuthal angle about the  $\mathbf{b}$  or  $\mathbf{a}$  axes are given in Fig. 5.12 and 5.13. Clearly all of these modes have characteristic fingerprint like angular shapes which might be useful to identify specific modes in comparison between theory and experiment.

For  $a_2$  modes in the  $xy$  plane and for  $\mathbf{e}_i$  at an angle  $\phi$  from the  $x$ -axis and  $\mathbf{e}_o$  at an angle  $\phi + \frac{\pi}{2}$  from the  $x$ -axis the angular pattern is  $d^2 \cos 2\phi$ , which is a symmetric four-leave clover pattern. The same is true for the  $b_{1T}$  modes with crossed polarizers and with azimuthal angle  $\phi$  with respect to the  $\mathbf{b}$  axis in the  $xz$  plane and for  $b_{2T}$  modes in the  $xy$  plane as function of azimuthal angle about the  $\mathbf{a}$ -axis.

### 5.3.5 Phonon dispersion and density of states

The phonon densities of states (DOS) are shown in Fig. 5.14. The DOS figure shows the partial density of states for each of the constituents as well as the total DOS. The vibrational modes fall clearly in two ranges, the quasi-acoustic range below 400  $\text{cm}^{-1}$  and the optic range above 500  $\text{cm}^{-1}$ . The heavier atoms, Zn, Ge and Ga have their strongest weight in the low-frequency range, which shows two peaks. In these two peaks, we can see that the Ga contribution is about equally spread over both, while the Zn contributes more to the low energy region and Ge more to the higher energy region. As the masses of these atoms increase from Zn to Ga to Ge, but are all close to each other, it is clear that this distribution does not reflect the mass differences but rather the differences in force constants related to these frequencies. The high

frequency optical mode range can almost entirely be attributed to the presence of the lighter N atoms. It consists of three peaks and zooming in on the cation contributions, we can see that Ga atoms show a higher contribution in the middle and lower peaks, the Zn contribution is stronger in the lower frequency peak, and that of the Ge atoms in the highest peaks. While we cannot simply separate Zn-N, Ga-N and Ge-N bond stretch modes because the actual normal modes are mixtures of them, it still suggest clearly an increasing bond strength in the same order. The phonon densities of states of GaN and  $\text{ZnGeN}_2$  can be found in the Materials Project [90] and were here included for comparison. Comparing the DOS figure with either of  $\text{ZnGeN}_2$  or that of GaN, we find striking similarities. The acoustic region in GaN also shows two distinct peaks. However the optical range is much narrower and has basically a TO and LO branch peak only.

In  $\text{ZnGeN}_2$  the optical mode region has a similar overall frequency range but is split in more distinct peaks and is overall stretched over a wider range of frequencies than even for  $\text{ZnGeGa}_2\text{N}_4$ . This indicates that the Ga-N bond stretch related modes are intermediate in frequency between the Zn-N and Ge-N ones and hence fill out this spectral range in a more uniform way. The relative contribution of Zn-N and Ge-N bonds in different frequency ranges in  $\text{ZnGeN}_2$  is found to be consistent with the present results in  $\text{ZnGeGa}_2\text{N}_4$ .

The phonon density of states is important because several thermodynamic properties can be obtained from integrating over it. Secondly, it was found in previous studies of phonons in  $\text{ZnGeN}_2$  and related materials[91, 92] that for disordered forms of this material, the Raman spectra resemble the phonon DOS more than the specific modes at  $\Gamma$ . In other instances, a mixture of disorder related DOS type peaks and sharp peaks corresponding to specific  $\Gamma$ -modes can be seen [93]. This is because disorder breaks the momentum conservation law and allows modes throughout the Brillouin zone to contribute to the Raman scattering. Precise ordering in these

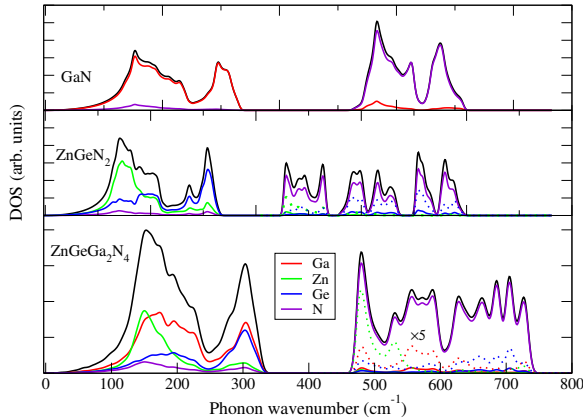


Figure 5.14: Phonon total and atom resolved partial densities of states of ZnGeGa<sub>2</sub>N<sub>4</sub> compared with those for GaN and ZnGeN<sub>2</sub>, the latter two from Materials Project. The dashed lines in the high frequency region for Zn, Ga and Ge were multiplied by a factor 5 for easier viewing of their relative contribution.

ternary and even more so in the present quaternary alloys is a significant challenge for the crystal growth.

Finally, the phonon band dispersions throughout the Brillouin zone are shown in Fig. 5.15. In addition to the information about the acoustic and optical phonon modes at high symmetry points as well as the sharp jumps in the phonon dispersion at  $\Gamma$  indicating LO-TO splitting along particular directions, this figure shows that the structure is dynamically stable, as it does not show any modes with imaginary frequency. At  $\Gamma$ , the plot gives the TO modes but one can clearly see that when one approaches  $\Gamma$  along for example the  $X - \Gamma$  direction, some modes (namely the  $b_1$  modes) approach the LO mode until the last data point along the line where they jump to the TO-value at  $\Gamma$ . Along  $Z - \Gamma$  this behavior happens for  $a_1$  modes and along  $Y - \Gamma$  it happens for  $b_2$  modes. We used 100 points along these lines. This reflects that the phonon frequencies in the limit  $\mathbf{q} \rightarrow 0$  depend on the direction one approaches 0 from. The objective behind using a much larger division of 100 points when approaching  $\Gamma$  is to capture the LO-TO splitting in the form of a sudden jumps

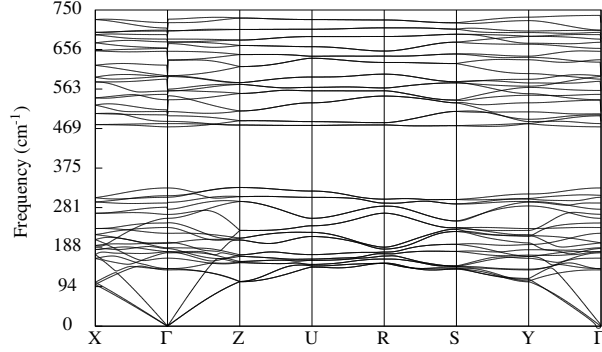


Figure 5.15: Phonon band structure of  $\text{ZnGeGa}_2\text{N}_4$ .  $X, Y, Z, U, R, S$  correspond to  $\mathbf{b}_1/2, \mathbf{b}_2/2, \mathbf{b}_2/2, (\mathbf{b}_1 + \mathbf{b}_3)/2, (\mathbf{b}_1 + \mathbf{b}_2 + \mathbf{b}_3)/2$  and  $(\mathbf{b}_1 + \mathbf{b}_2)/2$ .

in the optical phonon dispersion.

## 5.4 Conclusions

In this chapter, we presented a comprehensive study of the phonons in  $\text{ZnGeGa}_2\text{N}_4$ , a mixed 50 % compound of  $\text{ZnGeN}_2$  and  $\text{GaN}$  with a specific ordering, obeying the octet rule and with  $Pmn2_1$  spacegroup. A group theoretical analysis of the modes at  $\Gamma$  is presented and besides the vibrational frequencies, related quantities, such as the Born effective charges, and dielectric constants  $\varepsilon^\infty, \varepsilon^0$  tensors are presented. We then used these to predict infrared spectra and Raman spectra for various polarizations, which could be used to obtain fully all different modes and Raman tensor components. We showed that although the number of peaks seen in these spectrum simulations doesn't always match with the expected number of phonon modes from the symmetry analysis, this can be explained by some modes having very weak oscillator strengths or by the occurrence of closely spaced modes which merge into one peak. We showed that the alternation of TO and LO modes is obeyed in detail even though the *Reststrahlen* bands may give the impression of a mode switch in some instances. The correlation between LO and TO mode eigenvectors was also investigated and shows that for higher frequency modes there is no clear one-to-one correlation between corresponding

mode numbers. Angular patterns for Raman spectra of the modes were also shown and provide a further fingerprinting method to identify the modes and an opportunity to observe the sign of the Raman tensor elements. We also presented the full Brillouin zone phonon band structure and densities of states and resolved the latter into atom components, identifying thereby the contributions from separate cation-N bonds and their distribution over the phonon DOS.

# Chapter 6

## Vibrational properties of $\alpha$ -MoO<sub>3</sub>

### 6.1 Introduction

Orthorhombic  $\alpha$ -MoO<sub>3</sub> is a layered oxide with various applications and with excellent potential to be exfoliated as a 2D ultra-thin film or monolayer. While there have been prior Raman and infrared studies [36, 37, 28, 38] a full first-principles analysis of the vibrational properties and polarization dependent Raman spectra on single crystals or thin films has not yet been reported. Here we present a first-principles calculation of the phonons in  $\alpha$ -MoO<sub>3</sub> including simulations of the Raman and infrared spectra. This study may be useful in the characterization of ultra-thin layers or nano-flakes of MoO<sub>3</sub> and may assist in further understanding of  $\alpha$ -MoO<sub>3</sub> and the transition metal oxides, in general. A group theoretical analysis, phonon frequencies and related Born effective charges, dielectric constants, infrared oscillator strengths and Raman tensors are presented as well.

### 6.2 Computational Method

The calculations are done using Density Functional Perturbation Theory (DFPT)[59, 60] using the plane-wave pseudopotential method as implemented in ABINIT [39].

Specifically, with the Abinit code we choose the Hartwigsen-Goedecker-Hutter pseudopotentials [82] and the local density approximation. The energy cutoff used in these calculations 160 Rydberg, which was tested first to give converged results. For the Brillouin zone integration or charge densities and total energy a  $4 \times 4 \times 4$   $\mathbf{k}$ -point mesh is used. A first set of phonon calculations are done at the  $\Gamma$ -point. These are sufficient to determine the infrared absorption and reflection (IR) spectra as well as the Raman spectra assuming momentum conservation and using that visible and infrared light has negligible momentum compared to the Brillouin zone size.

## 6.3 Results

### 6.3.1 Crystal structure and group theoretical analysis

The space group of  $\alpha$ - $\text{MoO}_3$  is  $Pm\bar{c}n$  number 62 (or  $D_{2h}^{16}$ ). Note that the standard setting of the International Tables for Crystallography is  $Pnma$  but then the normal mirror plane, labeled  $m$ , is perpendicular to  $\mathbf{b}$  whereas ours is perpendicular to  $\mathbf{a}$ . In the symmetrized version of the Materials Project coordinates [90], corresponding to  $Pnma$  the direction normal to the layers is the  $a$  direction, which is our  $c$ . Hence the double glide mirror plane, labeled  $n$ , is perpendicular to  $\mathbf{c}$  in our case. The point group is  $D_{2h}$ . The unit cell of the structure contains 16 atoms, 4 Mo and 12 O atoms, which belong to three different types. The optimized lattice constant within LDA and reduced coordinates are given in Table 6.1. We also give the volume of the cell  $V$  in this table and compare our lattice constants with the experimental ones by Seguin *et al.* [28] and with the ones from Materials Project [90] optimized in the generalized gradient approximation (GGA) in the Perdew-Burke-Ernzerhof (PBE) parameterization.[86] Note that Seguin *et al.* [28] used yet another setting  $Pbnm$  where the largest lattice constant normal to the layers is the  $b$  direction.

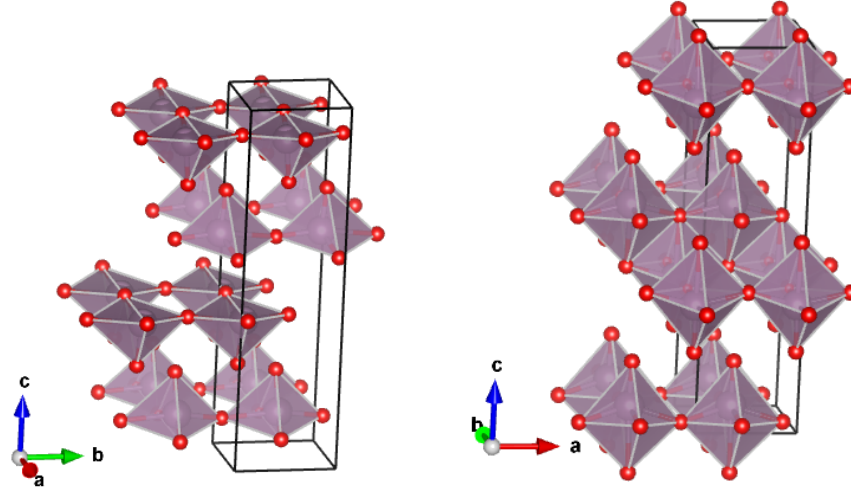
We may note that our lattice volume is slightly underestimated compared to the

experiment while the GGA value is 6 % overestimated. However, we should also note that this overestimate is mostly stemming from the  $c$ -lattice constant overestimate, which is 4 % and the about 2 % from the  $a$  lattice constant. The  $c$  lattice direction is perpendicular to the layers and thus most sensitive to the weak van der Waals interactions. The good agreement for this in LDA may be somewhat spurious and does not indicate that LDA should always perform well on such interlayer interactions but is useful here. Our  $b/a$  ratio at 1.062 is intermediate between the experimental value of 1.072 and the PBE value of 1.055. Our  $c/a$  ratio at 3.708 is smaller than the experimental value of 3.748 and the Materials Project [90] value of 3.855. The character table of the point group  $D_{2h}$  is given in Table 6.2.

The crystal structure is shown in Fig. 6.1. Note that the  $\text{O}_2$  is bonded to a single Mo and has a short bond of only 1.702 Å.  $\text{O}_1$  is bonded to two Mo in a bridge configuration along the  $b$  direction with alternating bond lengths of 1.781 Å and 2.218 Å.  $\text{O}_3$  is bonded to two Mo along the  $a$  direction each at 1.978 Å but also to another Mo at a larger distance of 2.386 Å in the  $c$ -direction. When this last long bond is ignored the structure can be described in terms of slightly distorted square pyramids which are corner sharing in the  $ab$ -plane. Two adjacent layers of such pyramids face each other via their flat faces and form a double layer with the short Mo- $\text{O}_2$  bonds facing outward. These double layers are weakly van der Waals bonded. When the longer bond of 2.386 is included in the coordination polyhedron, the structure can be viewed as consisting of distorted octahedra which share edges with the lower octahedron in the  $a$  direction and corners in the  $a$  and  $b$ -directions. Along the  $c$  axis double layers are stacked with a van der Waals gap formed between the  $\text{O}_2$  single bonded oxygens.

Excluding the translations along the three directions,  $x$ ,  $y$  and  $z$ , the vibrational

Figure 6.1: Crystal structure of  $\alpha$ - $\text{MoO}_3$  in the  $Pm\bar{c}n$  spacegroup setting. Viewed in terms of pyramidal or distorted octahedral units. The small red spheres are O atoms, the larger grey spheres hidden under the polyhedra are the Mo atoms. In the view on the left, the longest Mo-O bond in the vertical direction is omitted from the nearest neighbor polyhedron.



modes are distributed over the irreducible representations as

$$\begin{aligned} \Gamma^{vib} = & 8A_g \oplus 4B_{1g} \oplus 4B_{2g} \oplus 8B_{3g} \oplus 4A_u \\ & \oplus 7B_{1u} \oplus 7B_{2u} \oplus 3B_{3u}. \end{aligned} \quad (6.1)$$

Table 6.1: Reduced coordinates and lattice constants in  $\alpha$ - $\text{MoO}_3$  in the  $Pnma$  spacegroup.

atom	Wyckoff	$x$	$y$	$z$
Mo	4c	0.25	0.91613	0.60637
O <sub>1</sub>	4c	0.25	0.46959	0.58859
O <sub>2</sub>	4c	0.25	0.95868	0.72917
O <sub>3</sub>	4c	0.25	0.50056	0.93527
	$a$ (Å)	$b$ (Å)	$c$ (Å)	$V$ (Å <sup>3</sup> )
Calc. (LDA)	3.7217	3.9510	13.7916	202.798
Expt. [28]	3.6964	3.9628	13.855	202.949
MP (PBE)[90]	3.761	3.969	14.425	215.328

Table 6.2: Character table of  $D_{2h}$ .

irrep	$E$	$I$	$C_{2y}$	$m_{xz}$	$C_{2z}$	$m_{xy}$	$C_{2x}$	$m_{yz}$	basis function
$A_g$	1	1	1	1	1	1	1	1	$x^2, y^2, z^2$
$B_{1g}$	1	1	-1	-1	1	1	-1	-1	$xy$
$B_{2g}$	1	1	1	1	-1	-1	-1	-1	$xz$
$B_{3g}$	1	1	-1	-1	-1	-1	1	1	$yz$
$A_u$	1	-1	1	-1	1	-1	1	-1	$xyz$
$B_{1u}$	1	-1	-1	1	1	-1	-1	1	$z$
$B_{2u}$	1	-1	1	-1	-1	1	-1	1	$y$
$B_{3u}$	1	-1	-1	1	-1	1	1	-1	$x$

### 6.3.2 Phonon frequencies and related results.

The phonon frequencies at  $\Gamma$  are given in Table 6.3. Corresponding to the light propagating along  $\mathbf{z}$ ,  $\mathbf{x}$  or  $\mathbf{y}$ , the LO-TO splittings are observed for  $B_{1u}$ ,  $B_{3u}$  and  $B_{2u}$  modes, respectively. From Table 6.3, we can observe that the splittings are significantly smaller for the lower frequency modes compared to the higher frequency modes. This is because only the high frequency modes have significant bond stretch dipolar character. The larger LO-TO splittings are also correlated with stronger oscillator strengths for infrared absorption.

Our calculated values are compared with the experimental results of Seguin *et al.* [28] who also includes previous experimental results and provides a symmetry labeling of the modes. These data are here reproduced in Fig. 6.2 for easier comparison with the results in figs for IR and Raman spectra. However, we have relabeled them to take into account the different choice of crystallographic axes here. Our  $a, b, c$  correspond to Seguin's  $c, a, b$ . Taking  $x, y, z$  along  $a, b, c$  this then also implies that our  $B_{1u}, B_{2u}, B_{3u}$  correspond to their  $B_{2u}, B_{3u}, B_{1u}$  respectively and our  $B_{1g}, B_{2g}, B_{3g}$  become their  $B_{2g}, B_{3g}, B_{1g}$ .  $A_g$  and  $A_u$  stay the same. The  $A_u$  modes are silent and can thus not be measured by either infrared or Raman spectroscopies. The calculated phonon frequencies can be seen to generally underestimate the experimental value up to 14 %, although the errors are not uniformly distributed. The modes with -14%

error turn out to be modes with quite weak oscillator strengths and where several modes are close in frequency so that the experimental assignment may not be entirely clear if polarization selection rules were not used. For example for mode  $B_{1u}^4$ , the value  $374 \text{ cm}^{-1}$  was measured by Seguin *et al.* [28] while Py and Mashke [37] give a calculated value  $B_{1uT}^4 = 380 \text{ cm}^{-1}$  but did not observe it experimentally. Seguin *et al.* assign this mode as strong while nearby  $B_{2u}$  mode at  $358 \text{ cm}^{-1}$  is designated as weak. Another weak peak is observed in the IR spectrum at  $350 \text{ cm}^{-1}$ . The oscillator strengths given in Table 6.5 show clearly that  $B_{1u}^4$  should be weaker than  $B_{2u}^3$  and  $B_{2u}^4$ . The proximity of these modes makes it difficult to disentangle them experimentally without using polarization dependence. If we re-assign the experimental  $358 \text{ cm}^{-1}$  mode as our  $B_{1uT}^4$  then our error on this mode frequency is reduced to  $-7\%$ . The experimental  $374 \text{ cm}^{-1}$  peak would then correspond to the  $B_{2u}^4$  average of TO and LO modes.

One may also observe that each TO phonon mode of a given symmetry is followed by an LO before the next TO phonon occurs. This is a general rule obeyed by any crystal with at least orthorhombic symmetry, but not for monoclinic symmetry. We note that this follows from general considerations of the phonon related  $\varepsilon$  and  $\varepsilon^{-1}$  in a Lorentz oscillator model. However, it does not mean that the eigenvectors of the TO-LO pairs constructed in this way are necessarily close to each other.

We now discuss the nature of a few of the vibrational modes. The lowest frequency  $B_{1u}^1$  corresponds to a sliding of an entire bilayer with respect to the other in the  $b$  direction as can be seen in Fig. 6.2(a). The  $B_{2u}^1$  mode on the other hand has bilayers moving relative to each other perpendicular to each other Fig. 6.2(b).

The  $A_g^1$  mode on the other hand consists mostly of a sliding of the layers within one bilayer with respect to each other but also with a slight breathing component of the distance between these layers within the bilayer (Fig. 6.3)(a). This mode is already significantly higher in frequency which clearly shows that the bonding between layers

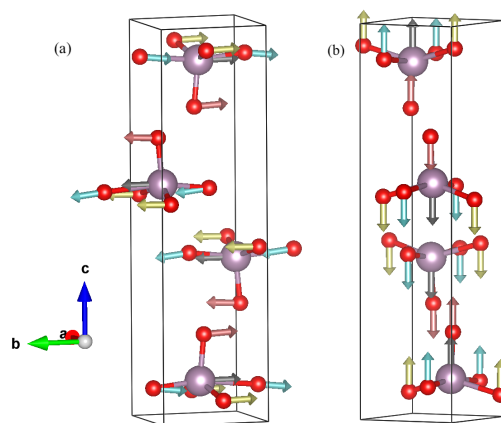


Figure 6.2: Eigendisplacement pattern for (a)  $B_{1u}^1$  mode and (b)  $B_{2u}^1$  modes.

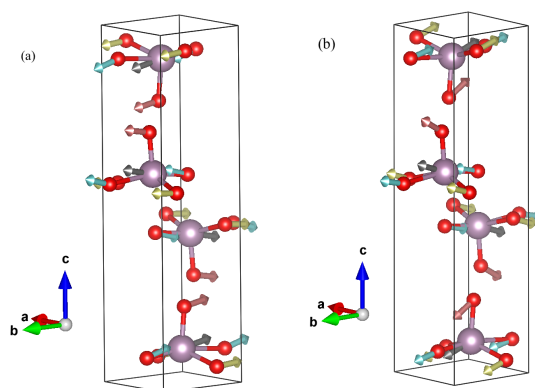


Figure 6.3: Eigendisplacement pattern for (a)  $A_g^1$  mode and (b)  $B_{3g}^1$  mode.

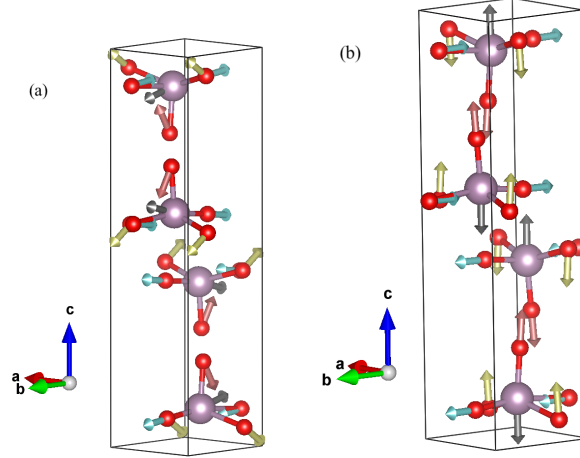


Figure 6.4: Eigendisplacement pattern for (a)  $A_g^7$  mode and (b)  $A_g^8$  mode.

within a bilayer is stronger than between bilayers. The lowest  $B_{3g}^1$  mode is similar but with the two bilayers having opposite sign instead of the same sign (Fig. 6.3(b)). The  $A_g^2$  and  $B_{3g}^2$  modes are mostly a breathing mode of the interlayer distance within a bilayer but again, either in phase between the two bilayers or out of phase. The intermediate frequency modes are more complex in nature.

### 6.3.3 Infrared spectra and associated quantities.

In this section, we present our simulated infrared spectra and associated quantities. These are obtained from calculating the contribution of phonons to the dielectric response function in terms of the classical Lorentz oscillator model. Within DFPT, the oscillator strengths can be obtained directly from the phonon eigenvectors and the Born effective charges, which describe the coupling of the vibrational modes to an electric field and are obtained as a mixed derivative of the total energy vs. a static electric field and an atomic displacement, given by

$$Z_{\kappa\beta\alpha}^* = \frac{\partial^2 E_{tot}}{\partial u_{\kappa\alpha} \partial E_\beta} = V \frac{\partial P_\beta}{\partial u_{\kappa\alpha}} = \frac{\partial F_{\kappa\alpha}}{\partial E_\beta} \quad (6.2)$$

Table 6.3: Phonon frequencies of  $\alpha$ - $\text{MoO}_3$  in  $\text{cm}^{-1}$ . Experimental values from Seguin *et al.* [28].  $\sigma$  is the error of the calc. compared to expt. in %

$B_{1uT}$			$B_{1uL}$			$B_{2uT}$		
calc	expt	$\sigma$	calc	expt	$\sigma$	calc	expt	$\sigma$
53.24	53	0.4	53.28	53	0.5	46.88	44	6
241.45	260	-7	243.10	260	-7	213.97	228	-6
303.31	353	-14	312.88	363	-14	301.57	348	-13
333.42	374	-11	334.62	380 <sup>1</sup>	-12	327.98	363	-10
428.85	441	-3	477.10	505	-5	476.96	500	-5
725.40	814	-11	737.92	825	-11	732.49	818	-10
909.44	962	-5	959.67	1010	-5	948.17	1002	-5
$B_{1g}$			$B_{3uT}$			$B_{3uL}$		
calc	expt	$\sigma$	calc	expt	$\sigma$	calc	expt	$\sigma$
101.50	116	-12	174.14	191	-9	176.97	191	-7
183.80	198	-7	244.22	268	-9	322.23	343	-6
258.69	283	-9	535.38	545	-2	799.16	851	-6
651.88	666	-2						
$A_g$			$B_{2uL}$			$B_{3g}$		
calc	expt	$\sigma$	calc	expt	$\sigma$	calc	expt	$\sigma$
73.44	83	-11	46.98	6	44	89.94	98	-8
151.43	158	-4	214.00	228	-6	146.16	154	-5
195.69	197	-1	321.22	352	-9	227.42	246	-8
299.00	337	-11	351.13	390	-10	302.60	338	-11
329.83	366	-10	490.32	525	-7	342.49	380	-10
445.84	472	-0.2	906.12	974	-7	447.71	472	-5
727.19	819	-11	948.17	1002	-5	729.82	820	-11
945.50	996	-5				957.39	996	-4
			$A_u$			$B_{2g}$		
			calc			calc	expt.	$\sigma$
			48.84			117.27	128	-8
			211.03			224.88	217	4
			263.01			270.29	291	-7
			535.78			652.04	666	-2

Table 6.4: Born effective charge tensor elements for the atoms listed in Table 6.1. By symmetry all  $Z_{xy}^*$ ,  $Z_{yx}^*$ ,  $Z_{xz}^*$ ,  $Z_{zx}^*$  are zero.

Components(label)	Mo	O <sub>1</sub>	O <sub>2</sub>	O <sub>3</sub>
$Z_{xx}^*(A_g)$	7.483	-1.139	-0.552	-5.790
$Z_{yy}^*(A_g)$	6.649	-4.859	-0.619	-1.169
$Z_{zz}^*(A_g)$	4.571	-0.686	-2.275	-1.609
$Z_{yz}^*(B_{3g})$	0.285	-0.305	-0.343	-0.303
$Z_{zy}^*(B_{3g})$	0.617	-0.506	-0.350	-0.197

where  $P_\beta$  is the macroscopic polarization,  $V$  the unit cell volume and  $u_{\kappa\alpha}$  the displacement of atom  $\kappa$  in direction  $\alpha$  which for a  $\mathbf{q} = 0$  mode is the same in each unit cell.  $F_{\kappa\alpha}$  is the force on the atom  $\kappa$  in direction  $\alpha$  and  $E_\beta$  is the electric field component. Atomic units are used throughout in which  $\hbar = e = m_e = 1$ . Note that the Born effective charge tensors are not macroscopic tensors but only reflect the point group symmetry of the Wyckoff site of that atom. Because the atoms are all in  $4c$  positions which lie on the mirror planes  $m_x$  and hence need to have zero  $xz$  and  $xy$  tensor elements. However they do have a non-zero  $yz$  and  $zy$  element, which differ because the first index refers to the derivative vs. electric field and the second to the derivative vs. atom displacement direction. The Born charges are seen to deviate significantly from the nominal charge of  $\text{Mo}^{+6}$  and  $\text{O}^{-2}$  and have also significant anisotropies. Specifically, O<sub>2</sub> which is bonded to a single Mo in the  $z$  direction is seen to be anomalously small in the  $x$  and  $y$  directions. On the other hand O<sub>1</sub> which is the bridge oxygen is seen to have the largest effective charge component in the  $y$  direction and O<sub>3</sub> in the  $x$  direction. The off-diagonal  $yz, zy$  elements sum to zero for each atom type separately because of the sign changes of the symmetry related atoms which behave as  $B_{3g}$ . The diagonal terms sum to zero for each diagonal component when summing over all atoms, balancing the cation and anions.

Table 6.5: Oscillator strength tensors.

$S_{n,xx} (B_{3u})$	$S_{n,yy} (B_{2u})$	$S_{n,zz} (B_{1u})$
$9.07 \times 10^{-5}$	$3.05 \times 10^{-7}$	$6.94 \times 10^{-8}$
$1.67 \times 10^{-3}$	$4.85 \times 10^{-7}$	$1.559 \times 10^{-5}$
$4.33 \times 10^{-3}$	$5.94 \times 10^{-4}$	$1.08 \times 10^{-4}$
	$1.06 \times 10^{-4}$	$1.07 \times 10^{-5}$
	$2.73 \times 10^{-4}$	$5.05 \times 10^{-4}$
	$3.55 \times 10^{-3}$	$1.62 \times 10^{-4}$
	$2.22 \times 10^{-9}$	$8.71 \times 10^{-4}$

The oscillator strength is then given by

$$S_{n,\alpha\alpha} = \left| \sum_{\kappa,\alpha'} Z_{\kappa,\alpha\alpha'}^* U_n(\kappa, \alpha') \right|^2, \quad (6.3)$$

where  $Z_{\kappa,\alpha\alpha'}^*$  are the Born effective charge tensor components given in Table 5.4,  $U_n(\kappa, \alpha')$  are the eigenvectors for each of the modes  $n$  at  $\mathbf{q} = 0$  and,  $\kappa$  refers to the atom label. The eigenvectors are normalized as

$$\sum_{\kappa\alpha} U_n(\kappa, \alpha)^* M_\kappa U_m(\kappa, \alpha) = \delta_{nm}, \quad (6.4)$$

where  $M_\kappa$  are the atom masses. Note that because of the orthorhombic symmetry the oscillator strength tensor is diagonal. Its non-zero elements are listed in Table 6.5. One can see from this table, that the higher frequency modes tend to have higher oscillator strengths. This is because they correspond to bond stretches and thus have a significant dipole moment associated with them. An exception is the highest  $B_{2u}$  mode has quite small oscillator strength and correspondingly also small TO-LO splitting.

The frequency dependent dielectric function in the region below the band gap is

Table 6.6: High-frequency and static dielectric tensor components.

$\varepsilon_{xx}^\infty$	$\varepsilon_{yy}^\infty$	$\varepsilon_{zz}^\infty$	$\varepsilon_{xx}^0$	$\varepsilon_{yy}^0$	$\varepsilon_{zz}^0$
6.792	6.162	4.662	27.210	13.024	7.173
5.959	5.205	4.001			

Table 6.7: The indices of refraction.

$n_{xx}$	$n_{yy}$	$n_{zz}$
2.606	2.482	2.159
2.441	2.282	2.000

given by

$$\varepsilon_{\alpha\alpha}(\omega) = \varepsilon_{\alpha\alpha}^\infty + \frac{4\pi}{V} \sum_n \frac{S_{n,\alpha\alpha}}{\omega_n^2 - \omega^2 - i\Gamma_n\omega} \quad (6.5)$$

where  $\omega_n$  are the phonon frequencies and  $\Gamma_n$  is a damping factor.

The first term  $\varepsilon^\infty$  is the high-frequency dielectric constant, meaning at frequencies below the gap but above the phonon frequencies. More precisely it is the static limit of the electronic contribution to the dielectric function, in other words the contribution from all higher frequency excitations, namely the inter-band optical transitions. It is calculated in the DFPT framework as the adiabatic response to a static electric field in the  $x$ ,  $y$ ,  $z$  directions. Because of the orthorhombic symmetry it is also a diagonal tensor,  $\varepsilon_{\alpha\alpha}^\infty$ . The values of this tensor are given in Table 6.6. They are directly related to the anisotropic indices of refraction in the visible region below the gap but above the phonon frequencies. The values of  $n_{\alpha\alpha} = \sqrt{\varepsilon_{\alpha\alpha}^\infty}$  are given in Table 6.7 for convenience. The static dielectric constant  $\varepsilon_{\alpha\alpha}^0$  in Table 6.6 applies for frequencies well below the phonon frequencies.

From the above defined  $\varepsilon(\omega)$  we can extract various related optical functions, in the infrared range. In particular, the optical absorption  $\alpha(\omega) = 2\omega\text{Im}[\varepsilon(\omega)]/n(\omega)$  and the reflectivity  $R(\omega) = |(\tilde{n}(\omega) - 1)/(\tilde{n}(\omega) + 1)|^2$  with  $\tilde{n} = n + i\kappa = \sqrt{\varepsilon}$  the

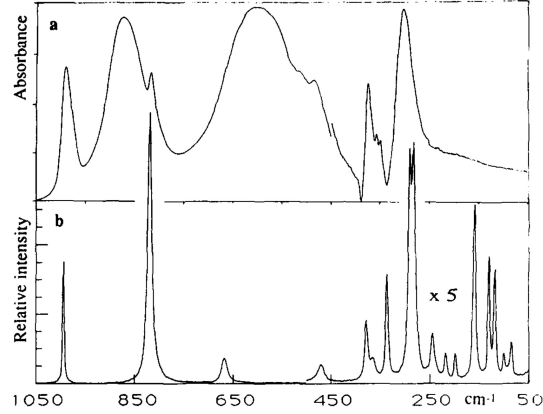
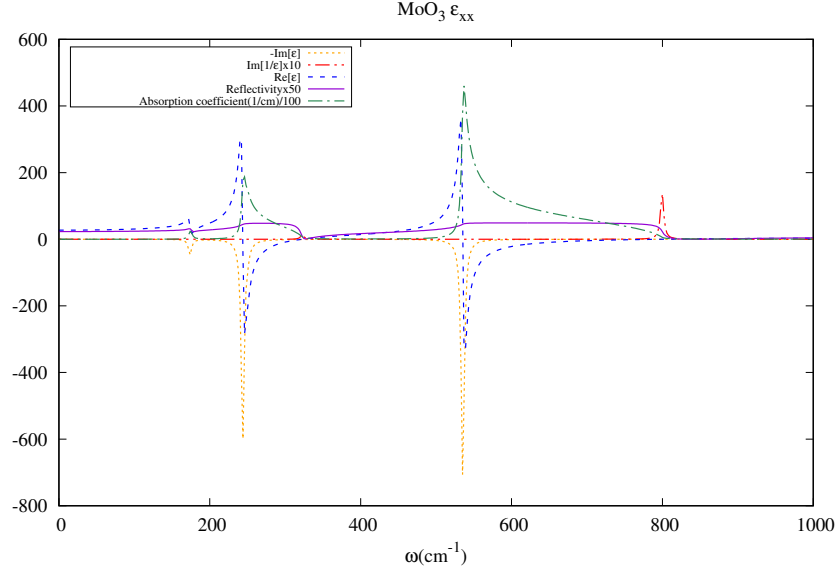


Figure 6.5: IR and Raman spectra of  $o$ - $\text{MoO}_3$ . The Raman spectrum below  $500 \text{ cm}^{-1}$  is amplified by a factor of 5. Image taken from [28].

complex index of refraction as well as the loss function  $-\text{Im}\{\varepsilon(\omega)^{-1}\}$  are the most closely related to the measurements. The zeros in the real part  $\varepsilon_1(\omega) = \text{Re}[\varepsilon(\omega)]$  and the peaks in the loss function indicate the LO mode frequencies, while the peaks in  $\varepsilon_2(\omega) = \text{Im}\{\varepsilon(\omega)\}$  give the TO modes. The reflectivity shows the typical *Reststrahlen* bands (RB) which jump to almost 100% reflectivity at the TO modes and fall back at the LO modes. Note that the absorption coefficient shows peaks corresponding to those in  $\varepsilon_2(\omega)$  but also shoulders at the zeros of  $\varepsilon_1(\omega)$ . The infrared spectra for the three polarizations are shown in Figs. 6.6,6.7,6.8. These correspond respectively to  $B_{1u}$ ,  $B_{2u}$  and  $B_{3u}$  modes which are active for polarizations along  $z$ ,  $y$  and  $x$ .

We may compare these with the IR absorption spectra of Seguin *et al.* [28] as seen in Fig. 6.5 which however do not mention the polarization. The highest absorption band found by them near  $1000 \text{ cm}^{-1}$  agrees well with our  $B_{1u}$  peak at  $909\text{-}945 \text{ cm}^{-1}$  and corresponds to  $z$ -polarization, related to the Mo-O<sub>2</sub> bond stretch of the shortest bond. The next main feature in Seguin *et al.* [28] corresponds to our  $B_{2u}$  spectrum for  $y$ -polarization and starts at  $B_{2uT}^6$  at  $732 \text{ cm}^{-1}$  and ends at the  $B_{2uL}^6$  at  $906 \text{ cm}^{-1}$ . Note that this mode is also close to the strongest  $A_g$  mode in Raman. However, the sharp feature on that peak at lower energy with much smaller LO-TO splitting is the  $B_{1uT}^6, B_{1uL}^6$  RB. The next broad feature is clearly dominated by the  $B_{3u}^3$  RB between


 Figure 6.6: IR spectra for  $B_{3u}$  modes.

535  $\text{cm}^{-1}$  and 799  $\text{cm}^{-1}$ . In the lower frequency region, a RB occurs near 260  $\text{cm}^{-1}$  in the experiment, which corresponds to peaks in our spectra near 240  $\text{cm}^{-1}$  and stems mostly from the  $x$  polarization  $B_{3u}^2$  mode. A less intense RB is seen near 350  $\text{cm}^{-1}$  which corresponds to our  $B_{2u}^4$  mode.

### 6.3.4 Raman spectra

The Raman cross-section for the Stokes process (energy loss) for each mode is given by,

$$\frac{dS}{d\Omega} = \frac{(\omega_0 - \omega_m)^4}{c^4} |\mathbf{e}_i \cdot \boldsymbol{\alpha}^m \cdot \mathbf{e}_o|^2 \frac{\hbar}{2\omega_m} (n_m + 1) \quad (6.6)$$

where  $\omega_0$  is the incident light frequency,  $\omega_m$  the mode frequency, and  $n_m$  is the phonon occupation number  $n_m = [\exp(\hbar\omega_m/k_B T) - 1]^{-1}$ ,  $\mathbf{e}_i$  and  $\mathbf{e}_o$  refer to the incident and the scattered polarization directions and  $\boldsymbol{\alpha}^m$  is the second-rank Raman susceptibility tensor for mode  $m$  which is given by,

$$\alpha_{\alpha\beta}^m = \sqrt{V} \sum_{\kappa\gamma} \frac{\partial \chi_{\alpha\beta}}{\partial \tau_{\kappa\gamma}} U_m(\kappa\gamma), \quad (6.7)$$

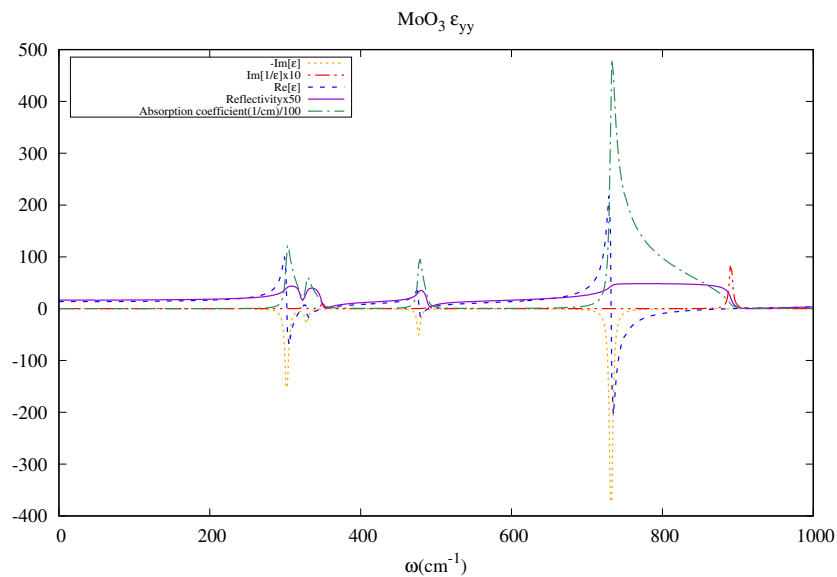


Figure 6.7: IR spectra for  $B_{2u}$  modes.

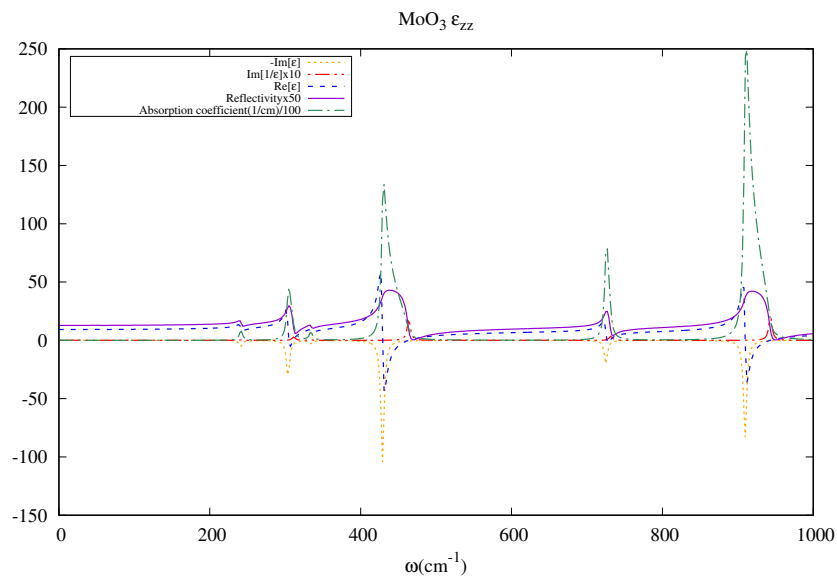
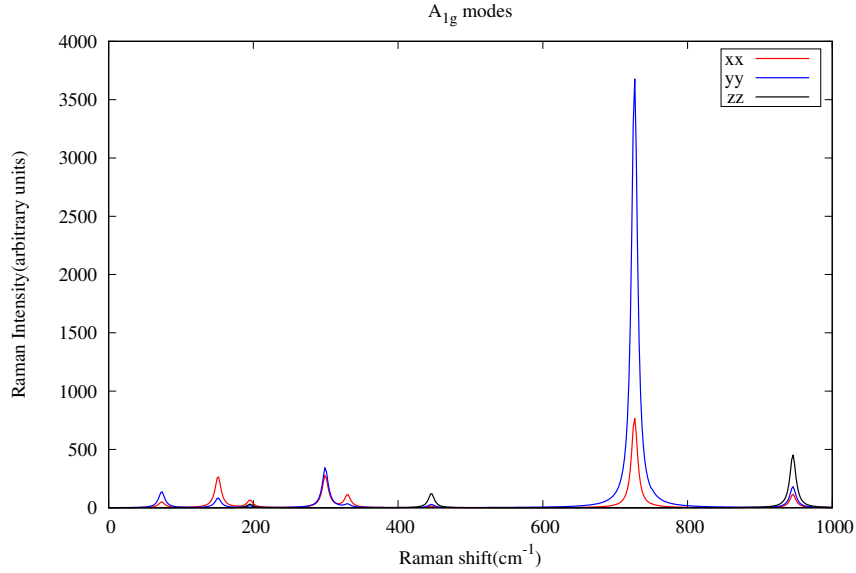


Figure 6.8: IR spectra for  $B_{1u}$  modes.

Table 6.8: Raman tensor components.

$A_g$ $a = \alpha_{xx}$	$A_g$ $b = \alpha_{yy}$	$A_g$ $c = \alpha_{zz}$
$1.99 \times 10^{-3}$	$3.34 \times 10^{-3}$	$-6.09 \times 10^{-5}$
$-6.93 \times 10^{-3}$	$-3.85 \times 10^{-3}$	$-2.39 \times 10^{-4}$
$3.84 \times 10^{-3}$	$1.83 \times 10^{-3}$	$-2.69 \times 10^{-3}$
$1.04 \times 10^{-2}$	$1.16 \times 10^{-2}$	$-1.22 \times 10^{-4}$
$-6.95 \times 10^{-3}$	$3.32 \times 10^{-3}$	$-3.98 \times 10^{-4}$
$2.97 \times 10^{-3}$	$4.26 \times 10^{-3}$	$-9.03 \times 10^{-3}$
$3.20 \times 10^{-2}$	$7.01 \times 10^{-2}$	$4.84 \times 10^{-4}$
$1.52 \times 10^{-2}$	$1.90 \times 10^{-2}$	$3.04 \times 10^{-2}$
$B_{1g}$ $d = \alpha_{xy}$	$B_{2g}$ $e = \alpha_{xz}$	$B_{3g}$ $f = \alpha_{yz}$
$3.24 \times 10^{-3}$	$-3.09 \times 10^{-3}$	$1.00 \times 10^{-3}$
$-3.92 \times 10^{-3}$	$3.67 \times 10^{-3}$	$7.40 \times 10^{-4}$
$1.17 \times 10^{-2}$	$-9.62 \times 10^{-3}$	$1.33 \times 10^{-3}$
$9.17 \times 10^{-3}$	$-1.72 \times 10^{-2}$	$2.16 \times 10^{-4}$
		$-7.88 \times 10^{-3}$
		$1.26 \times 10^{-3}$
		$8.75 \times 10^{-4}$
		$-9.53 \times 10^{-4}$


 Figure 6.9: Raman spectra for  $A_g$  modes.

in terms of  $U_m(\kappa\gamma)$ , the eigenvector of the  $m$ -th vibrational mode and the derivative of the susceptibility vs. atomic displacements.

The Raman tensor elements are given in Table 6.8. The Raman spectra for different scattering geometries, denoted by  $\mathbf{k}_i(\mathbf{e}_i\mathbf{e}_o)\mathbf{k}_o$  with  $\mathbf{k}_{i/o}$  the incident/scattered wavevector and  $\mathbf{e}_{i/o}$  the incident and scattered light polarization are given in Figs. 6.9, 6.10, 6.11 and 6.12. For  $A_g$  modes corresponding to parallel polarizations, the intensity of the spectrum depends on the polarization selected. For  $z(xy)z$  (transmission) or  $z(xy)\bar{z}$  (reflection) one measures  $B_{1g}$  modes, for  $xz$ -polarizations one measures  $B_{2g}$  and for  $yz$  polarization one measures  $B_{3g}$  modes.

One can see that the  $A_g$  have by far the strongest intensities. The  $B_{3g}$  modes are the weakest. The strongest  $A_g$  mode at  $727\text{ cm}^{-1}$  in  $yy$  polarization corresponds to a mode with mostly in-plane eigendisplacements of Mo- $\text{O}_1$  bond stretches. It also has fairly strong  $xx$  intensity but negligible  $zz$  motion because it does not involve motions normal to the layer. On the other hand, the  $A_g$  mode at  $945\text{ cm}^{-1}$  has its strongest polarization as  $zz$  and corresponds to a Mo- $\text{O}_2$  stretch mode. The strongest  $B_{1g}$  mode is at  $259\text{ cm}^{-1}$  while the strongest  $B_{2g}$  mode are at  $270\text{ cm}^{-1}$  and  $652\text{ cm}^{-1}$ . All modes

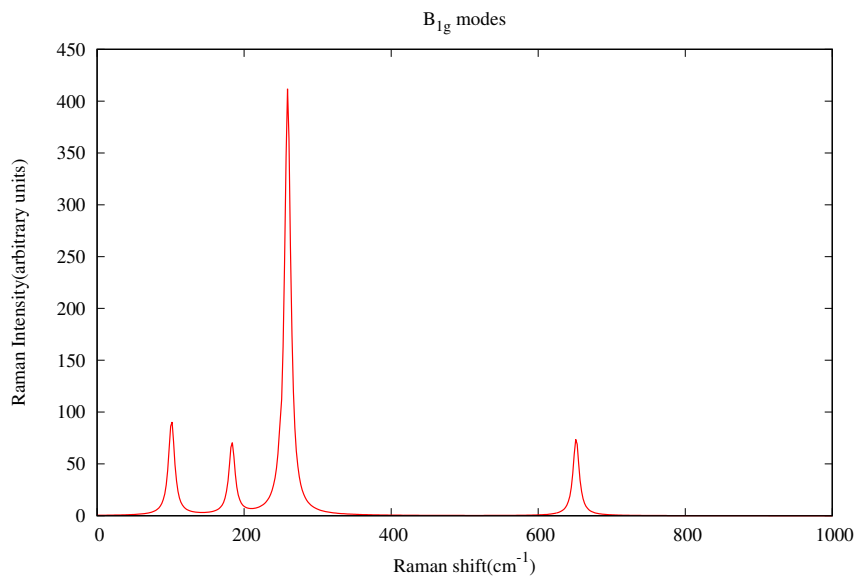


Figure 6.10: Raman spectrum for  $B_{1g}$  modes, scattering geometry  $z(xy)z$ .

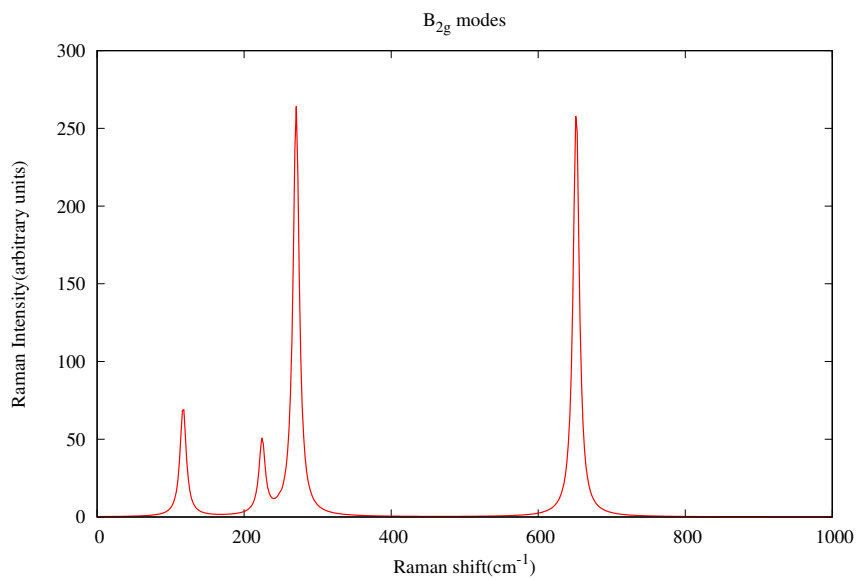


Figure 6.11: Raman spectrum for  $B_{2g}$  modes, scattering geometry  $y(xz)y$ .

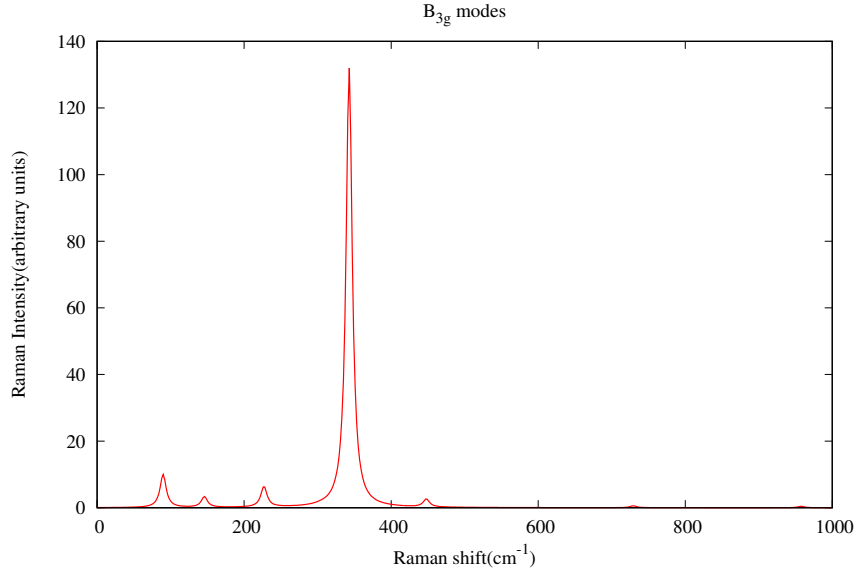


Figure 6.12: Raman spectrum for  $B_{3g}$  modes, scattering geometry  $x(yz)x$ .

below  $\sim 500 \text{ cm}^{-1}$  are significantly weaker. The three most prominent modes,  $A_g$  at  $945 \text{ cm}^{-1}$ ,  $727 \text{ cm}^{-1}$  and the  $B_{1g}$  mode at  $652 \text{ cm}^{-1}$  agree well with the experimental spectrum of Seguin *et al.* [28] shown in Fig. 6.5 apart from our underestimates of these frequencies compared to the experiment.

## 6.4 Conclusions

In this chapter, we have presented a DFPT study of the phonons in orthorhombic  $\alpha$ - $\text{MoO}_3$  with an emphasis on the Raman and infrared spectra. Agreement in phonon frequencies with experimental data is obtained to within about 10 % giving mostly an underestimate of the phonon frequencies in spite of using the LDA, which here apparently gives the volume very close to the experiment, while usually it tends to underestimate lattice constants. However the intensities in Raman spectra and the assignments of the major features are in good agreement with the experimental data reported in Seguin *et al.* [28], which also include previously measured values.

As we have seen from the eigendisplacement figures for various vibrational modes

in the bilayer structure, it seems some of the modes lead to interesting dynamics such as to cause one layer to slide past another or pull the layers apart. As an outlook for my future work, it would be interesting to study the monolayer structure as well and study the shifts in these phonon frequencies.

# Chapter 7

## Conclusions

In this thesis, we mainly focussed on two classes of materials, the wide band-gap oxides and the group II-III-IV nitride alloy system. In view of the growing interest in these materials with wide variety of applications, the goal of this thesis was to perform first-principles calculations and enhance the understanding of these materials. In chapter 3, we performed the QSGW band structure calculations for  $\beta$ -Ga<sub>2</sub>O<sub>3</sub> and reported the value of the band gap to be 4.9 eV. While initial calculations at the QSGW level gave an overestimate of the band gap, good agreement with experiment was obtained when (1) the calculation is sufficiently converged in the  $\mathbf{k}$ -point mesh on which the GW self-energy is calculated and (2) a reduction of the screening by 20% justified for many materials on the basis of including electron-hole interactions is included. On the other hand, electron-phonon coupling or specifically the lattice-polarization effect of the screening were found ultimately to be negligible. In addition to the band structure calculations, we also reported the anisotropy in the absorption onset. New insights were gained as we were studying the alloy system, (Al<sub>x</sub>Ga<sub>1-x</sub>)<sub>2</sub>O<sub>3</sub> in chapter 4. It was found that the LPC corrections in our initial calculations were significantly higher in comparison with the new calculations. It was primarily because of our use of a coarse  $\mathbf{k}$ -point mesh in the earlier work and thus the LPC corrections overestimated for the

electron-phonon interactions. We studied the alloy system for both the phases  $\alpha$  and  $\beta$ .  $\text{Al}_2\text{O}_3$  is found to be most stable in the rhombohedral crystal structure ( $R\bar{3}c$ ) as the most stable  $\alpha$  phase with a band gap of  $\sim 8.8$  eV. Likewise,  $\text{Ga}_2\text{O}_3$  is found to be most stable in the monoclinic crystal structure ( $C2/m$ ) as the most stable  $\beta$  phase. Both the phases consist of 10-atom unit cells with 4 cation positions available. The monoclinic cell has 2 tetrahedral and 2 octahedral cation coordinations while in the rhombohedral structure, all the 4 cation sites are octahedrally coordinated. The compositions of the alloy were varied from 0% Al concentration to 100% in the increments of 25%. The compositions were reported to be in excellent agreement with Vegard's law and the band structures for the lowest energy configurations for each composition were presented. With the finer  $\mathbf{k}$ -point mesh of  $5 \times 5 \times 3$  for monoclinic and  $4 \times 4 \times 4$  for the rhombohedral structure, the results were found to have the LPC corrections to be less than 0.1 eV and were in excellent agreement with the computational work reported by Peelaers *et. al.* [79] around the same time.

In chapter 5, we presented the first-principles calculations of the vibrational properties of  $\text{ZnGeGa}_2\text{N}_4$ , an alloy compound formed at 50% composition of GaN and  $\text{ZnGeN}_2$ . Of the many possible configurations, we focussed on the lowest energy, octet preserving superlattice formed by half a cell of  $\text{ZnGeN}_2$  and half GaN along the  $\mathbf{b}$ -axis of  $\text{ZnGeN}_2$  in the  $Pbn2_1$  structure. Using density functional perturbation theory implemented in ABINIT [39], we calculated the phonon modes at the zone center,  $\Gamma$  and presented the group theoretical analysis of the modes and several related quantities like the dielectric constants, Born effective charges, and oscillator strengths, which were then used to calculate the LO-TO splittings as well as the IR and Raman spectra. We also reported the element wise contributions as well as the total phonon density of states, and the phonon band structures. In chapter 6, we studied the vibrational properties of the bilayered, orthorhombic  $\alpha$ - $\text{MoO}_3$ . The phonon modes at the zone center  $\Gamma$ , the group theoretical analysis, and the related properties like dielectric

constants, Born effective charges, oscillator strengths are calculated and compared with the experimental work presented by Seguin *et. al.* [28]. Good agreement was obtained with the experimental data but our calculations provide additional details such as the polarization dependence of the IR and Raman spectra, which were not explicitly resolved in the previous experimental work. Our calculations also provide insights into the nature of the modes and why many modes occur in groups of four with closely related frequencies. This is related to the relative phases of the atomic motions in the bilayers relative to each other and those of the two layers that make up each bilayer. We also gained insight into the importance of the weak inter bilayer interactions for particular modes.

# Appendix A

## Appendix

### A.1 Supplemental material for $\text{ZnGeGa}_2\text{N}_4$

In this section we provide eigendisplacement patterns for each of the modes. First, in Table A.1 we give the positions of the 16 atoms in the cell and their symmetry relations. The structure and the symmetry elements are given in Fig. A.1.

The eigen displacement patterns of the modes are shown as bar graphs showing  $u_x$ ,  $u_y$ ,  $u_z$  displacements of each of the atoms labeled as in Table A.1 and normalized by multiplying the actual displacements of atom  $\kappa$  by  $1/\sqrt{M_\kappa}$ . The patterns of sign changes in  $u_x$ ,  $u_y$ ,  $u_z$  displacements between the atoms related by symmetry are given in Table A.2 for each type of Wyckoff position.

The  $a_1$  mode displacement patterns are shown in Figs. 7.2-7.15, the  $b_1$  modes in Figs. 7.16-7.24, the  $b_2$  in Figs. 7.25-7.37 and the  $a_2$  in Figs. 7.38-7.42. The TO and LO mode displacements of corresponding modes are shown together.

Table A.1: Reduced coordinates of atoms in the cell and the symmetry elements linking them to the first atom of each type. Note that  $2_{1z}$  is a two fold screw axis along  $z$  with translation in the  $z$  direction by  $c/2$  and placed at  $x = 0$   $y = -b/3$  and is thus accompanied by an additional translation of  $y = b/3$ ,  $m_x$  is an ordinary reflection but with translation  $x = a/2$  because it is placed at  $x = a/4$ ,  $n_y$  is a glide mirror plane with translations  $x = a/2$ ,  $z = c/2$  and an additional  $y = b/3$  because of its placement at  $y = b/6$ .

atom	$x$	$y$	$z$	symmetry elements
Ga <sub>1</sub>	0.001	-0.002	0.000	1
Ga <sub>2</sub>	0.501	0.335	0.500	$n_y$
Ga <sub>3</sub>	0.499	-0.002	0.000	$m_x$
Ga <sub>4</sub>	-0.001	0.335	0.500	$2_{1z}$
Zn <sub>1</sub>	0.250	0.830	0.500	1, $m_x$
Zn <sub>2</sub>	0.750	0.503	0.000	$2_{1z}$ , $n_y$
Ge <sub>1</sub>	0.750	0.838	0.500	1, $m_x$
Ge <sub>2</sub>	0.250	0.495	0.000	$2_{1z}$ , $n_y$
N <sub>Ga1</sub>	-0.015	-0.001	0.376	1
N <sub>Ga2</sub>	0.485	0.334	0.876	$n_y$
N <sub>Ga3</sub>	0.515	-0.001	0.376	$m_x$
N <sub>Ga4</sub>	0.015	0.334	0.876	$2_{1z}$
N <sub>Zn1</sub>	0.250	0.816	0.892	1, $m_x$
N <sub>Zn2</sub>	0.750	0.517	0.382	$2_{1z}$ , $n_y$
N <sub>Ge1</sub>	0.750	0.850	0.857	1, $m_x$
N <sub>Ge2</sub>	0.250	0.483	0.357	$2_{1z}$ , $n_y$

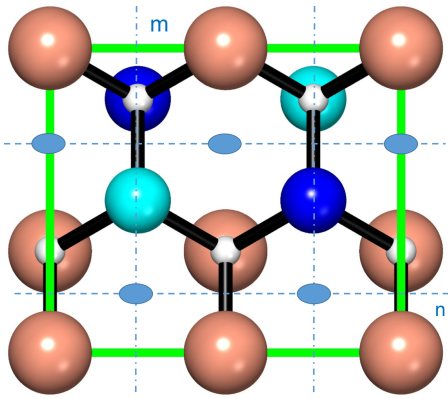


Figure A.1:  $Pmn2_1$  structure of  $ZnGeGa_2N_4$  projected along  $c$ -axis indicating symmetry elements. Image taken from [25].

Table A.2: Sign changes of displacements between symmetry related atoms 1-4 for Wyckoff 4a and 1-2 for Wyckoff 2b atom ordered as in Table A.1.

irrep	4a			2b		
	$u_x$	$u_y$	$u_z$	$u_x$	$u_y$	$u_z$
$a_1$	+- - -	+ - + -	+ + + +	00	+ -	+ +
$a_2$	+ - + -	+ + - -	+ - - +	+ -	00	00
$b_1$	+ + + +	+ - - +	+ + - -	+ +	00	00
$b_2$	+ - - +	+ + + +	+ - + -	00	+ +	+ -

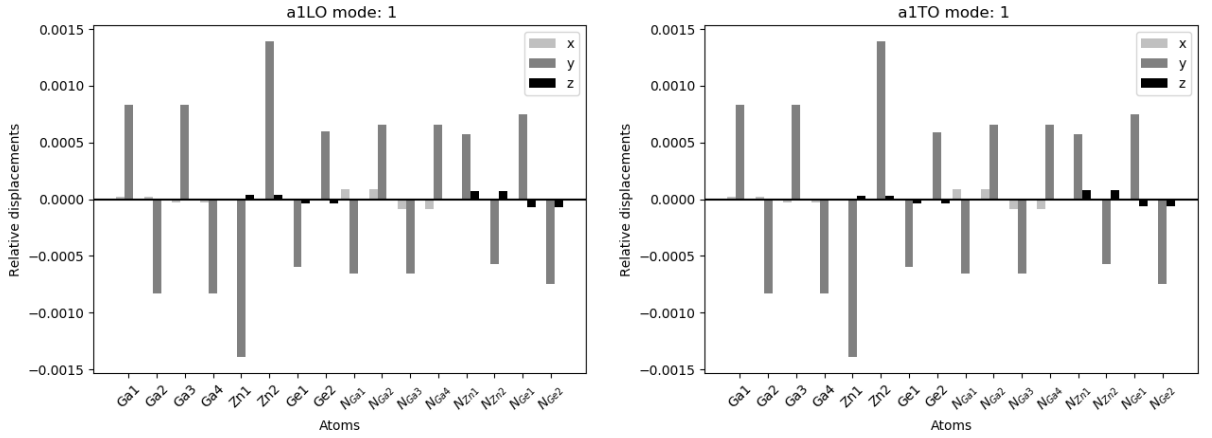


Figure A.2:  $a_1^n$  modes eigendisplacements (a) LO (b) TO for  $n = 1$

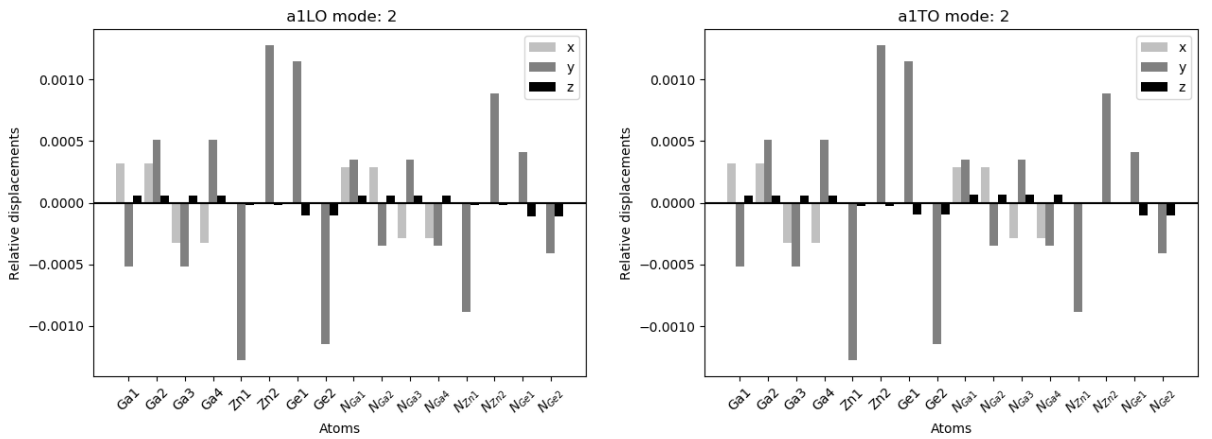


Figure A.3:  $a_1^n$  modes eigendisplacements (a) LO (b) TO for  $n = 2$

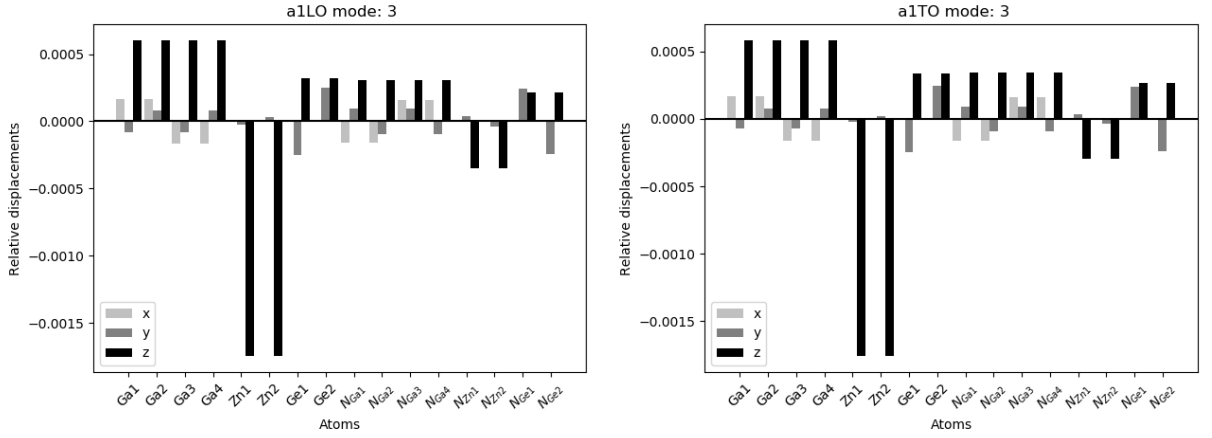


Figure A.4:  $a_1^n$  modes eigendisplacements (a) LO (b) TO for  $n = 3$

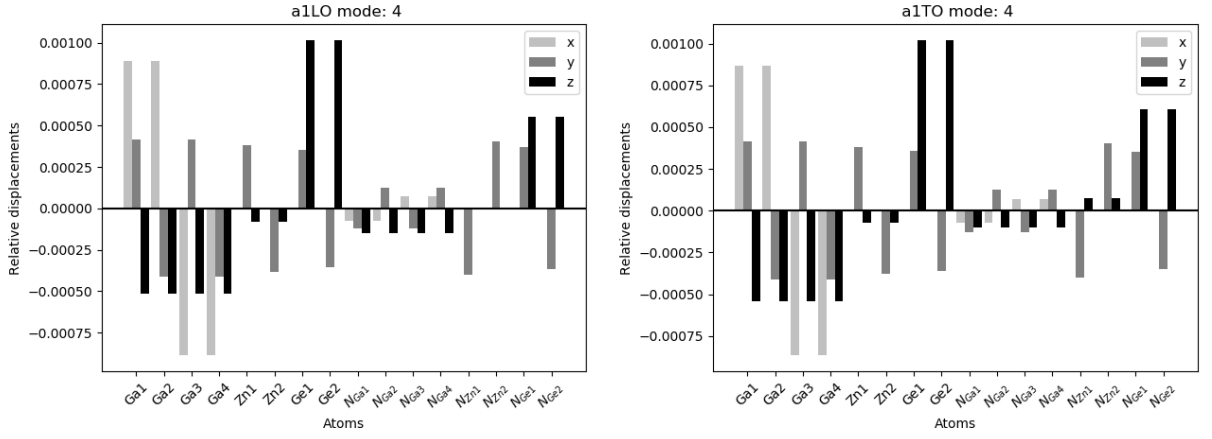


Figure A.5:  $a_1^n$  modes eigendisplacements (a) LO (b) TO for  $n = 4$

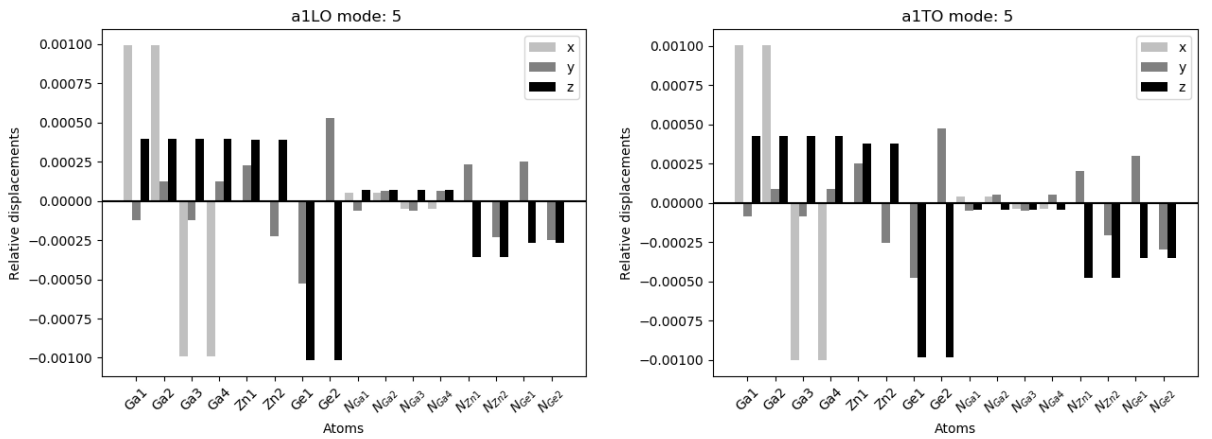


Figure A.6:  $a_1^n$  modes eigendisplacements (a) LO (b) TO for  $n = 5$

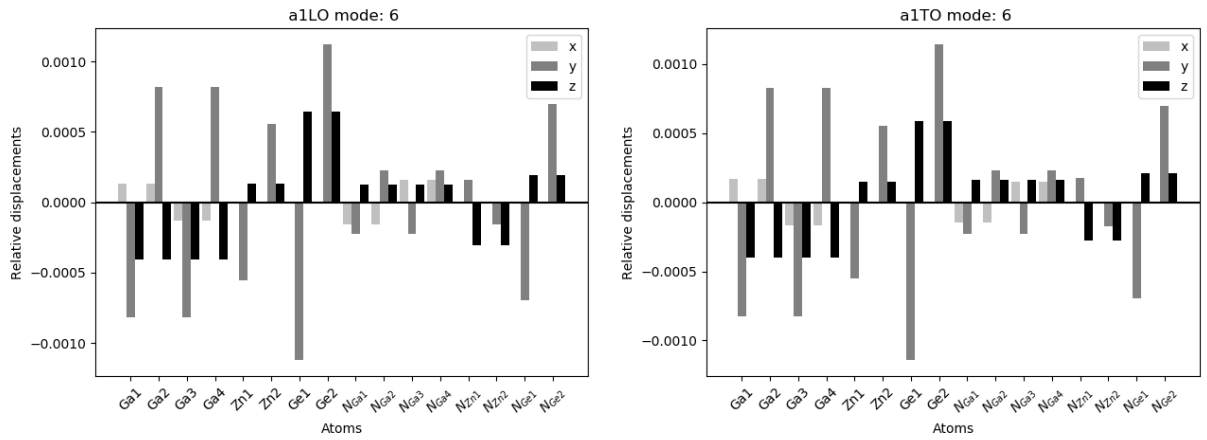


Figure A.7:  $a_1^n$  modes eigendisplacements (a) LO (b) TO for  $n = 6$

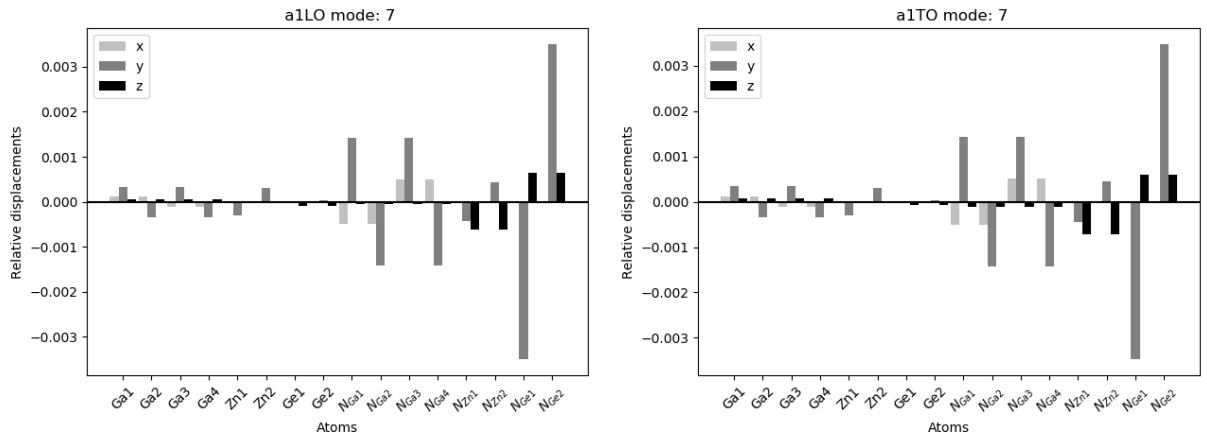


Figure A.8:  $a_1^n$  modes eigendisplacements (a) LO (b) TO for  $n = 7$

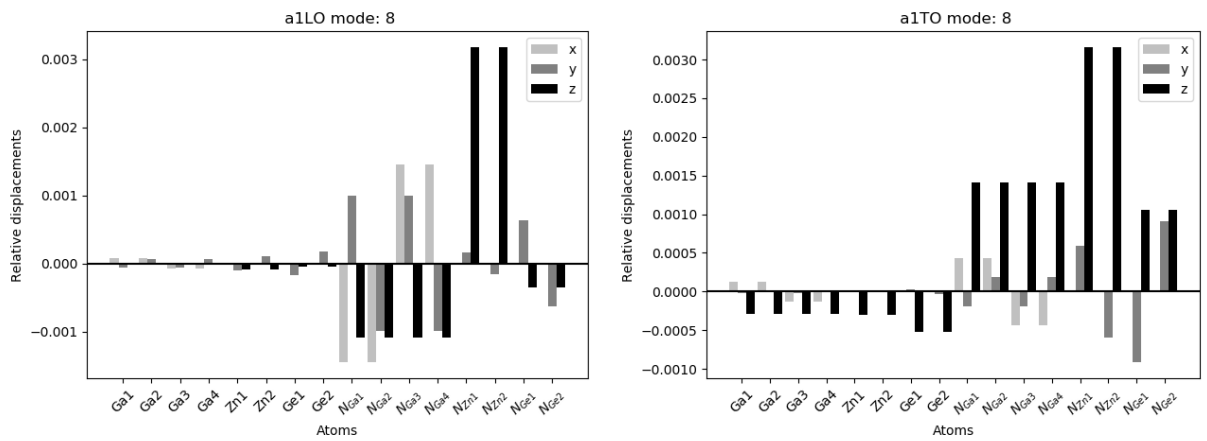


Figure A.9:  $a_1^n$  modes eigendisplacements (a) LO (b) TO for  $n = 8$

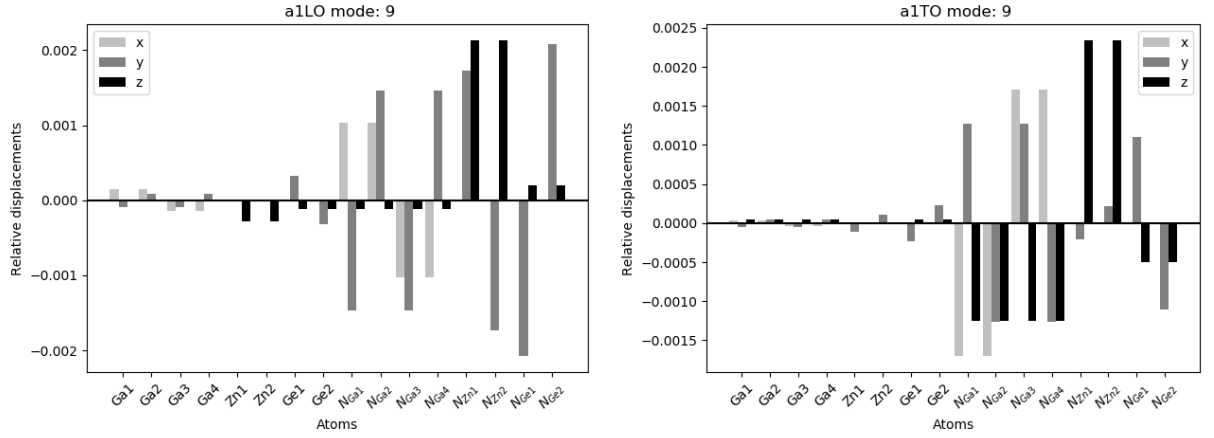


Figure A.10:  $a_1^n$  modes eigendisplacements (a) LO (b) TO for  $n = 9$

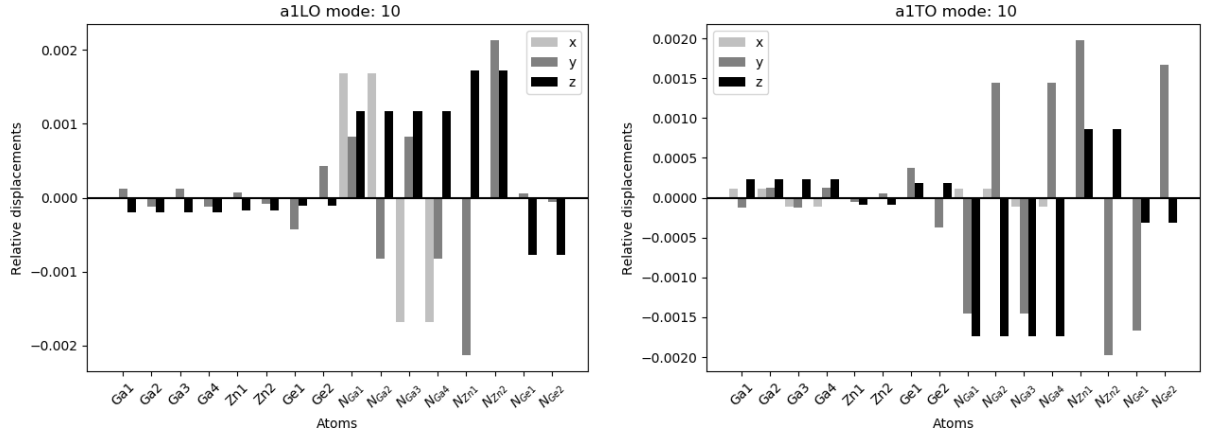


Figure A.11:  $a_1^n$  modes eigendisplacements (a) LO (b) TO for  $n = 10$

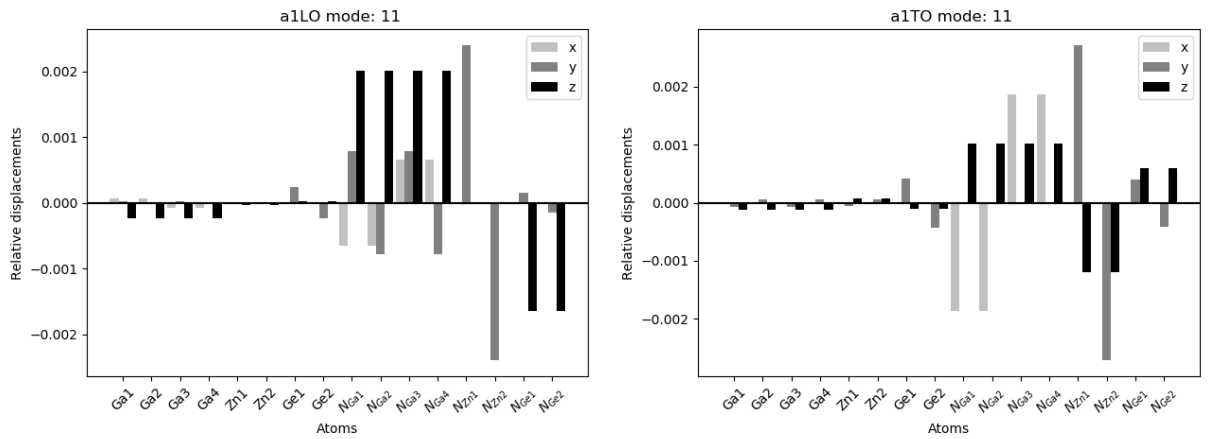


Figure A.12:  $a_1^n$  modes eigendisplacements (a) LO (b) TO for  $n = 11$

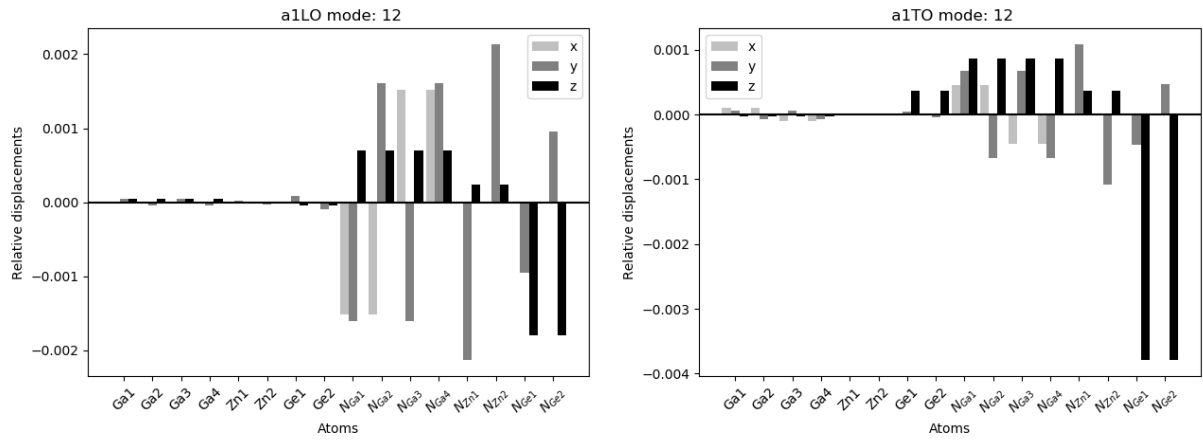


Figure A.13:  $a_1^n$  modes eigendisplacements (a) LO (b) TO for  $n = 12$

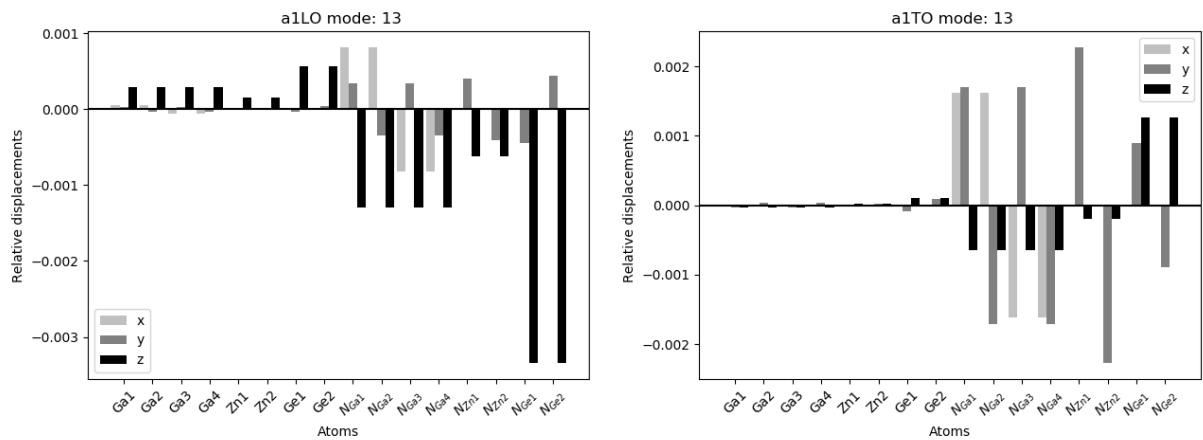


Figure A.14:  $a_1^n$  modes eigendisplacements (a) LO (b) TO for  $n = 13$

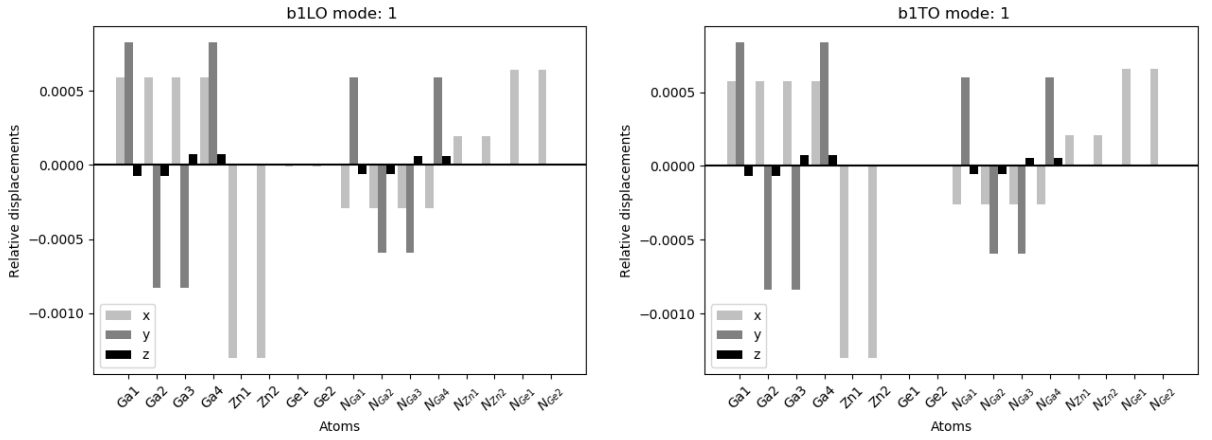


Figure A.15:  $b_1^n$  modes eigendisplacements (a) LO (b) TO for  $n = 1$

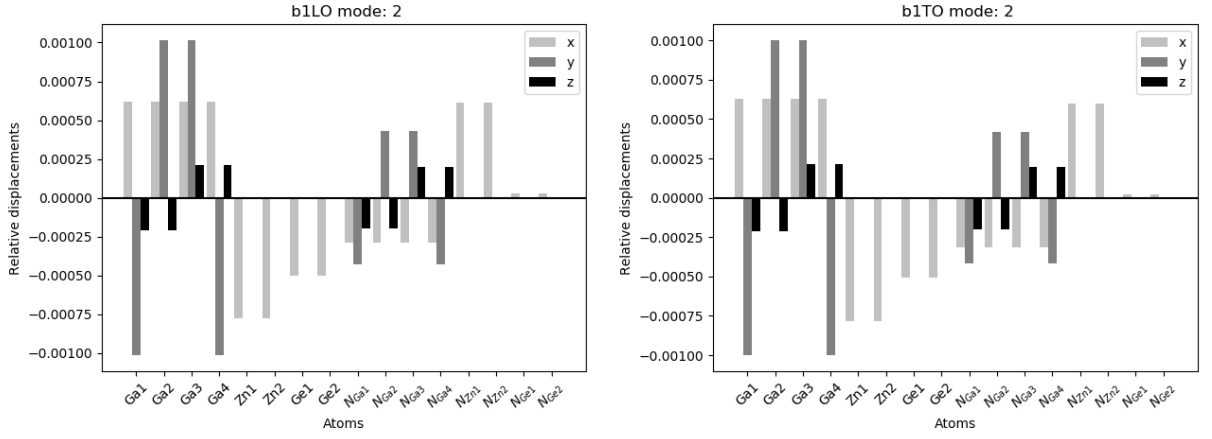


Figure A.16:  $b_1^n$  modes eigendisplacements (a) LO (b) TO for  $n = 2$

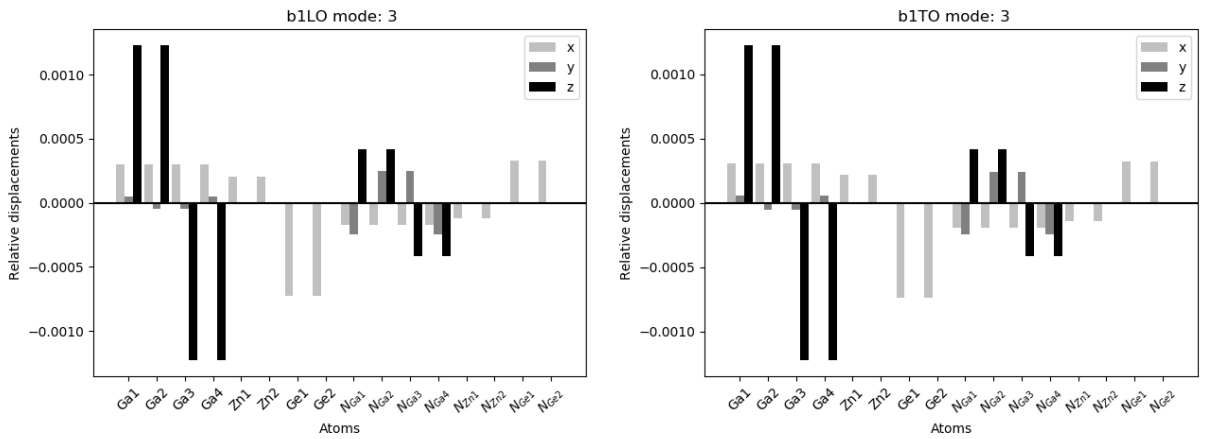


Figure A.17:  $b_1^n$  modes eigendisplacements (a) LO (b) TO for  $n = 3$

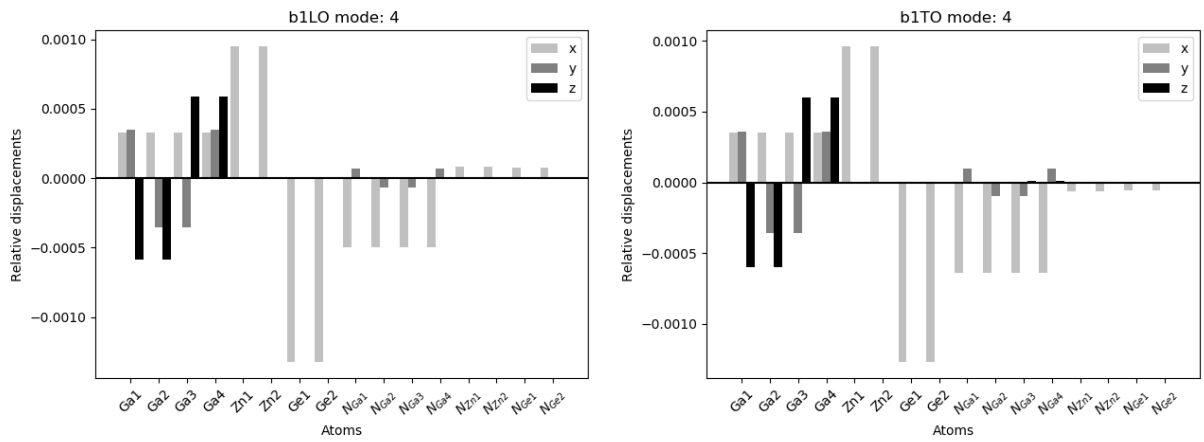


Figure A.18:  $b_1^n$  modes eigendisplacements (a) LO (b) TO for  $n = 4$

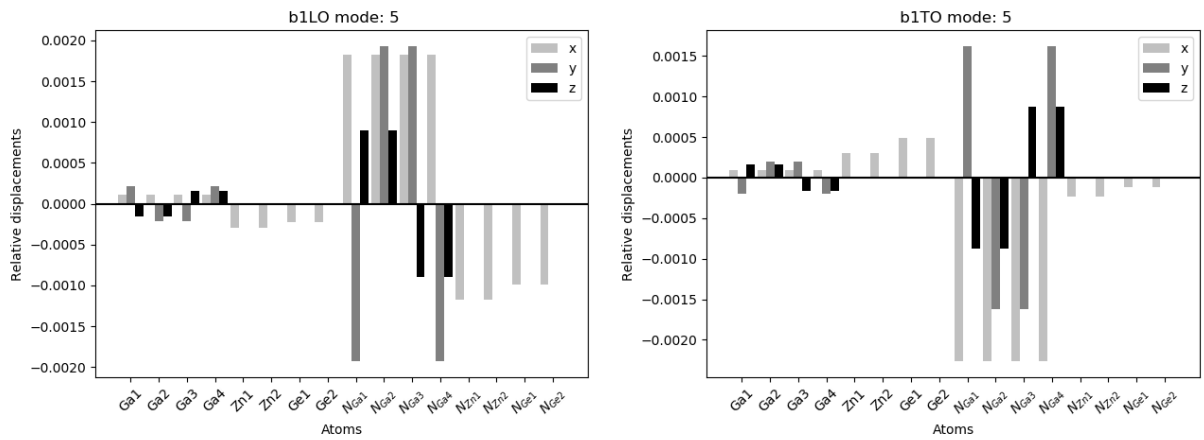


Figure A.19:  $b_1^n$  modes eigendisplacements (a) LO (b) TO for  $n = 5$

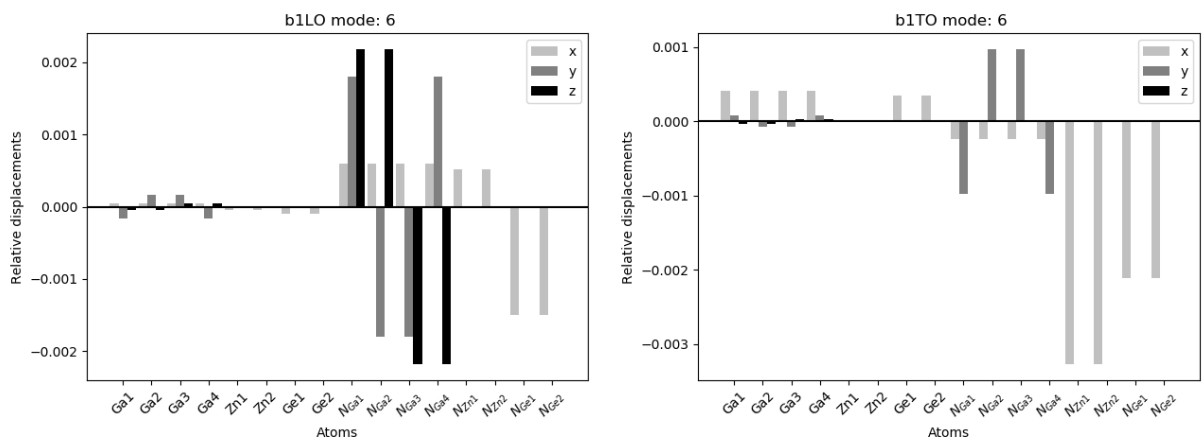


Figure A.20:  $b_1^n$  modes eigendisplacements (a) LO (b) TO for  $n = 6$

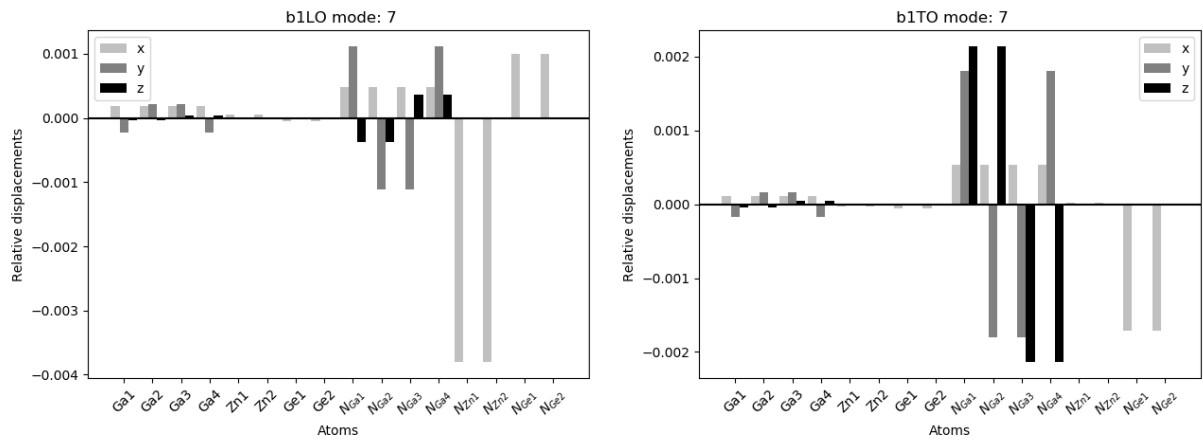


Figure A.21:  $b_1^n$  modes eigendisplacements (a) LO (b) TO for  $n = 7$

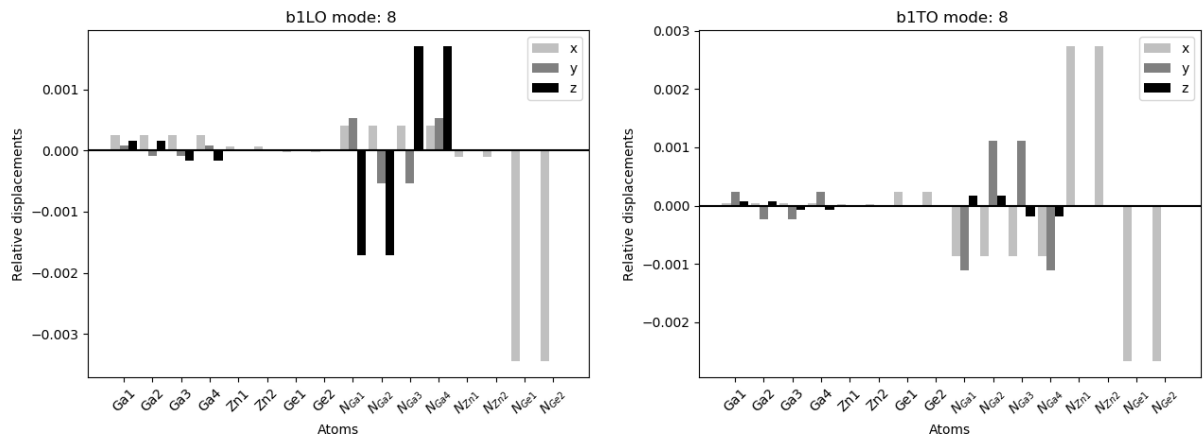


Figure A.22:  $b_1^n$  modes eigendisplacements (a) LO (b) TO for  $n = 8$

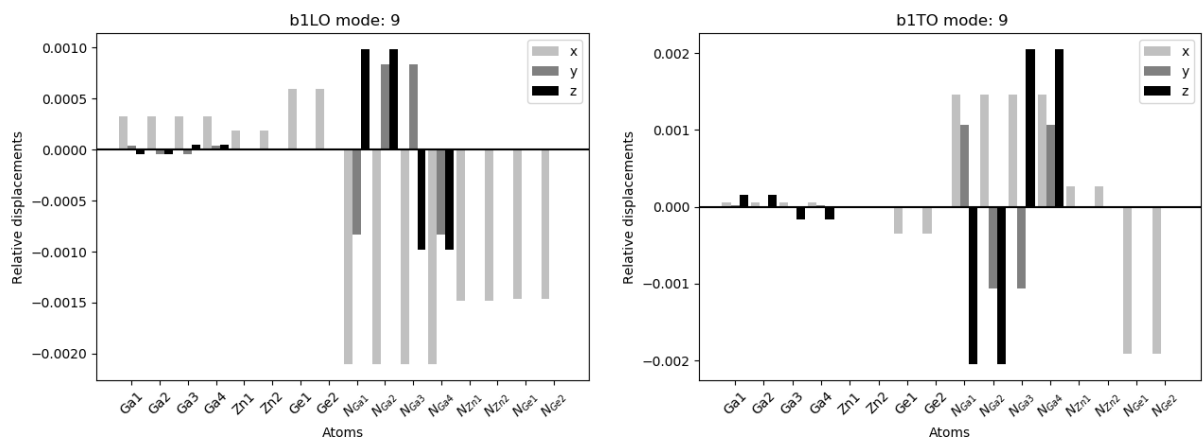


Figure A.23:  $b_1^n$  modes eigendisplacements (a) LO (b) TO for  $n = 9$

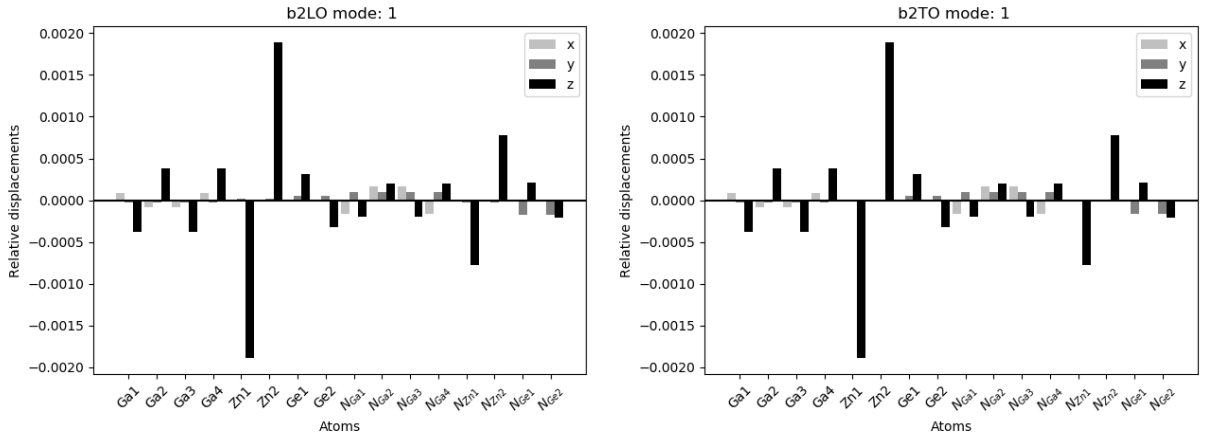


Figure A.24:  $b_2^n$  modes eigendisplacements (a) LO (b) TO for  $n = 1$

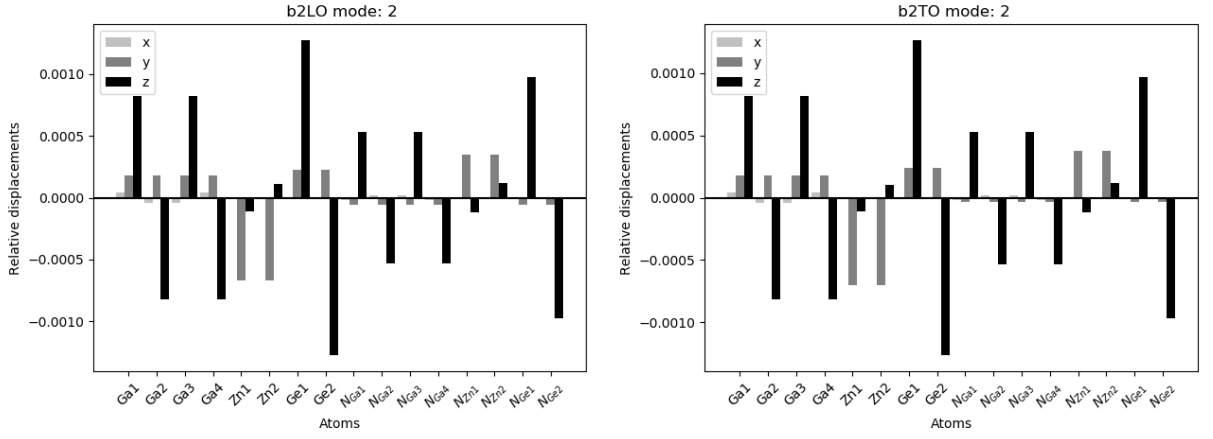


Figure A.25:  $b_2^n$  modes eigendisplacements (a) LO (b) TO for  $n = 2$

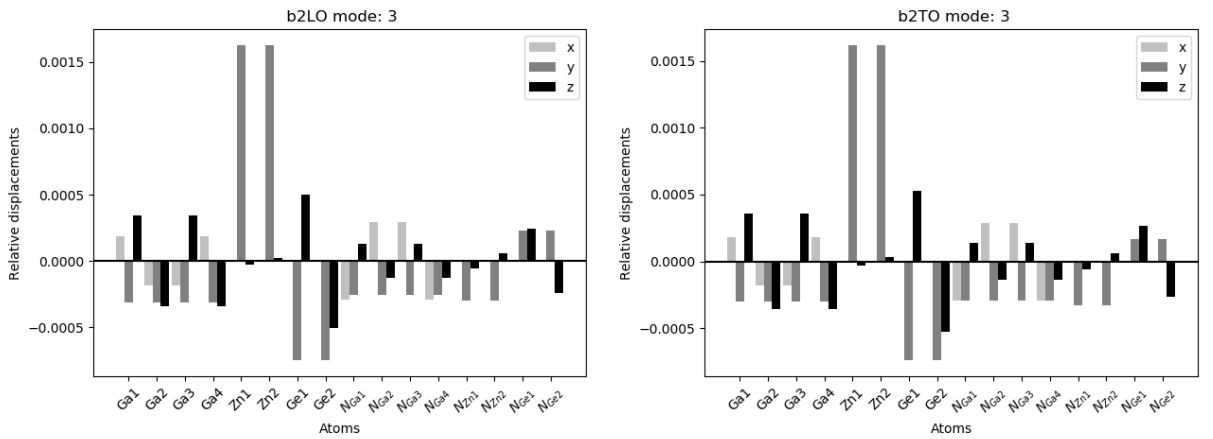


Figure A.26:  $b_2^n$  modes eigendisplacements (a) LO (b) TO for  $n = 3$

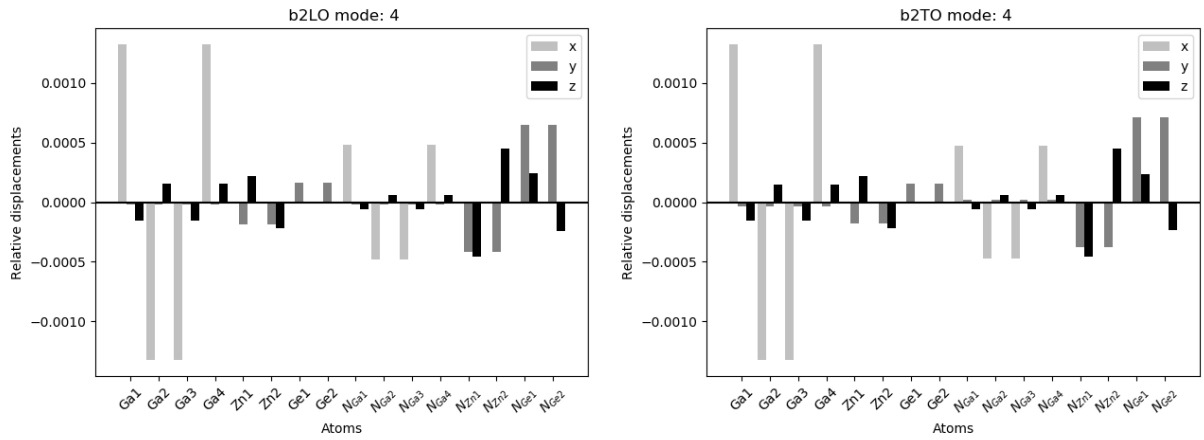


Figure A.27:  $b_2^n$  modes eigendisplacements (a) LO (b) TO for  $n = 4$

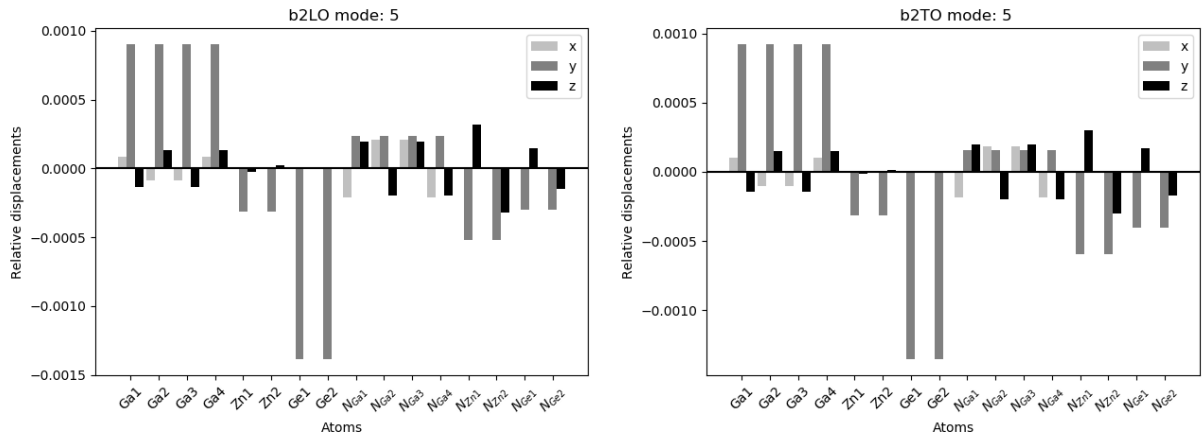


Figure A.28:  $b_2^n$  modes eigendisplacements (a) LO (b) TO for  $n = 5$

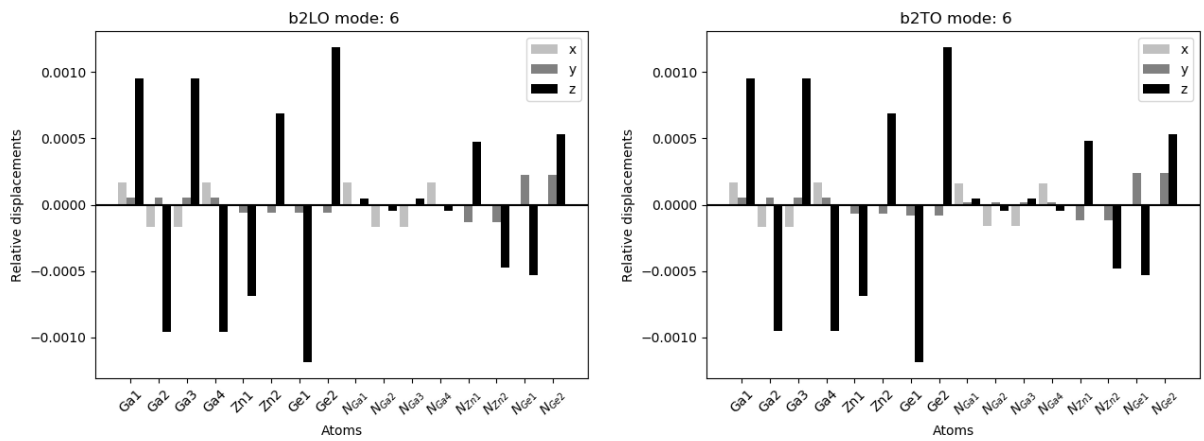


Figure A.29:  $b_2^n$  modes eigendisplacements (a) LO (b) TO for  $n = 6$

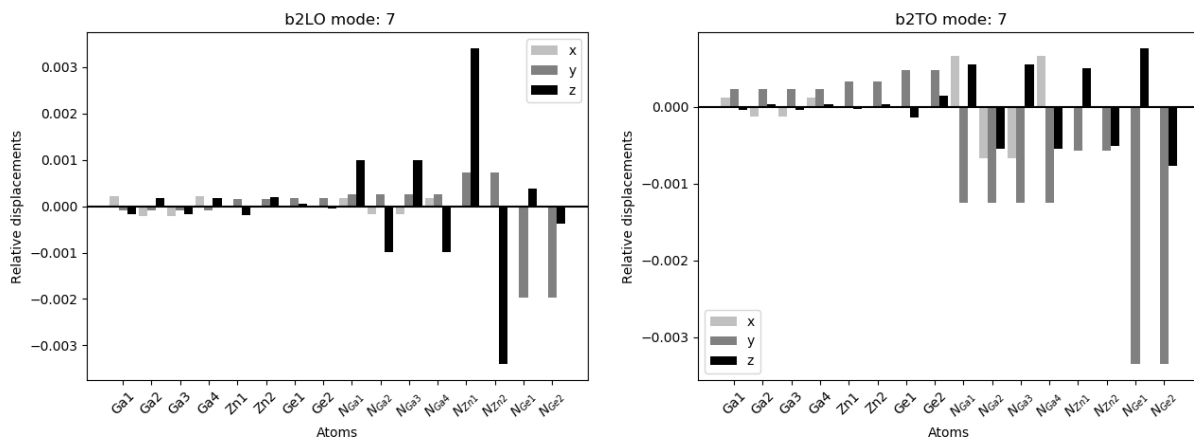


Figure A.30:  $b_2^n$  modes eigendisplacements (a) LO (b) TO for  $n = 7$

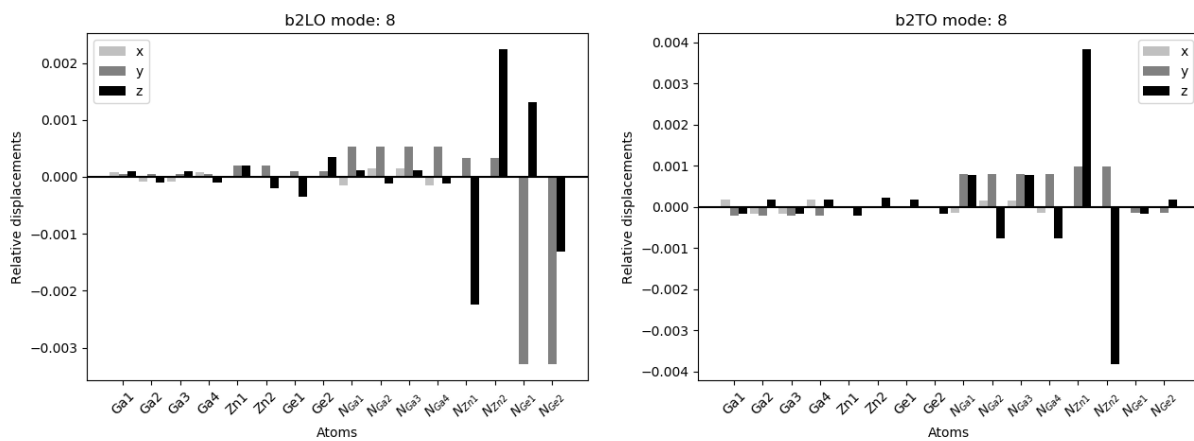


Figure A.31:  $b_2^n$  modes eigendisplacements (a) LO (b) TO for  $n = 8$

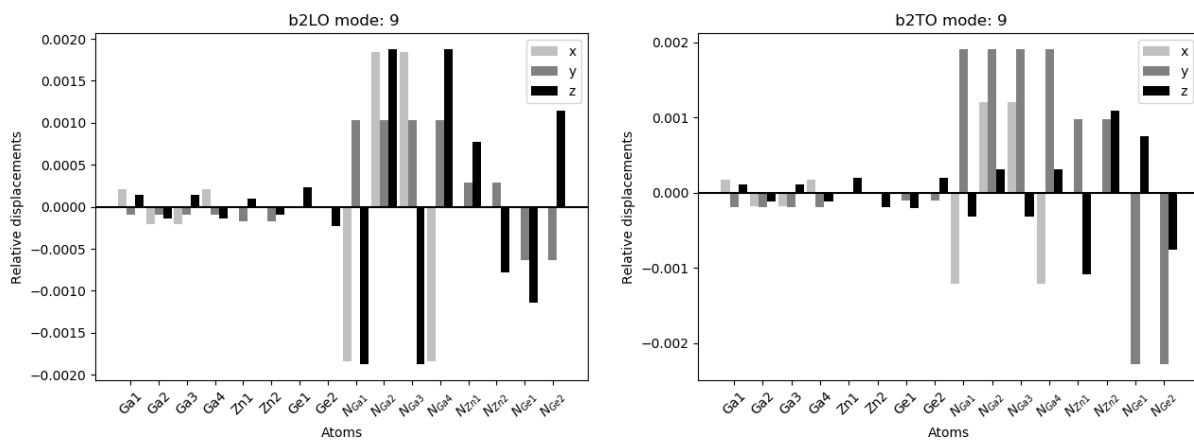


Figure A.32:  $b_2^n$  modes eigendisplacements (a) LO (b) TO for  $n = 9$

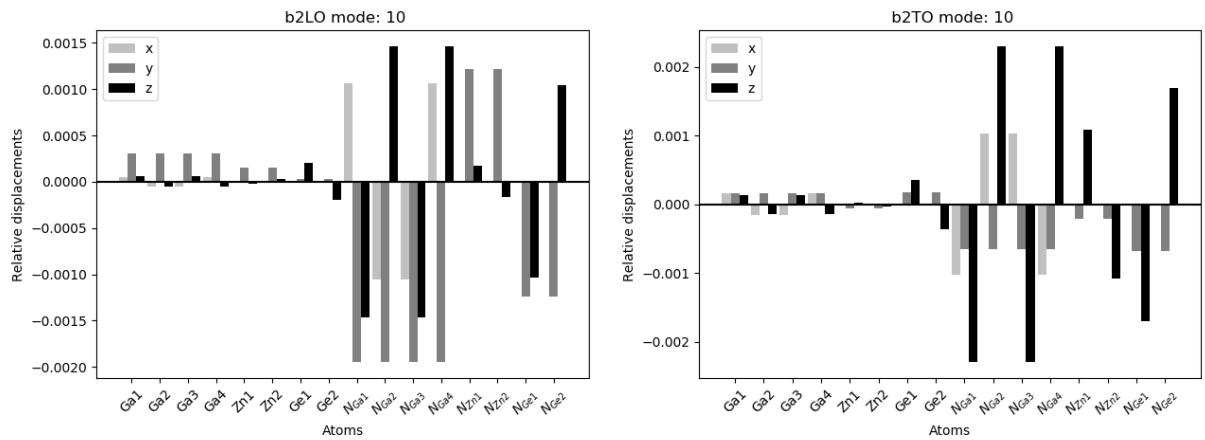


Figure A.33:  $b_2^n$  modes eigendisplacements (a) LO (b) TO for  $n = 10$

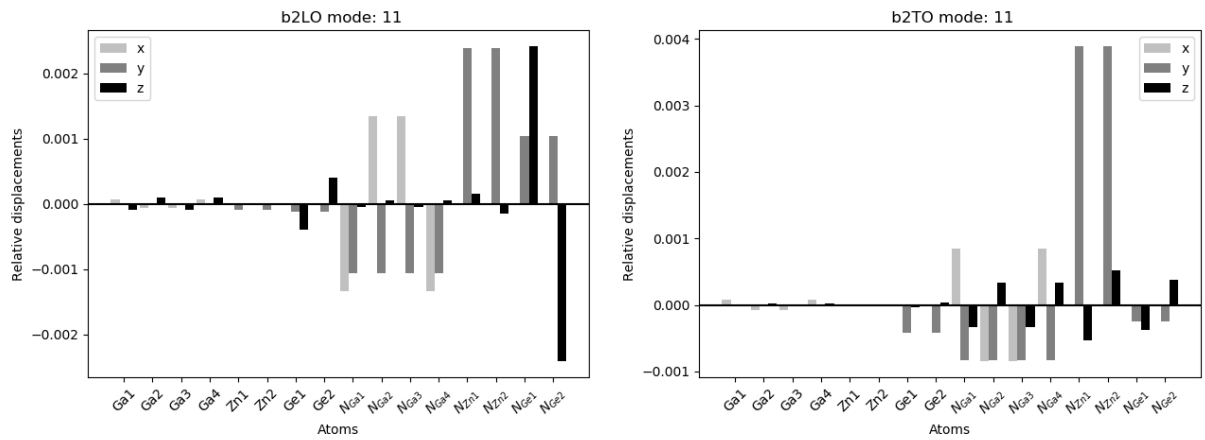


Figure A.34:  $b_2^n$  modes eigendisplacements (a) LO (b) TO for  $n = 11$

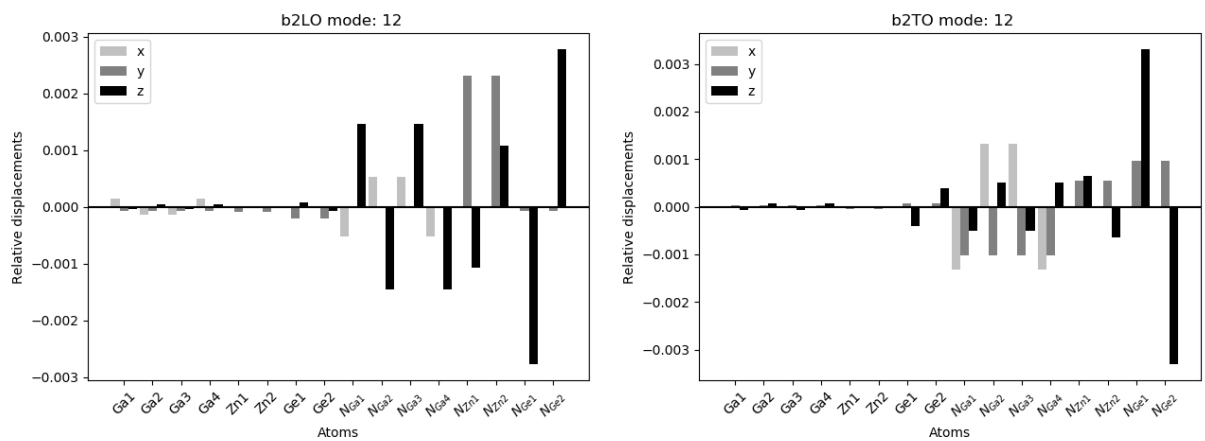


Figure A.35:  $b_2^n$  modes eigendisplacements (a) LO (b) TO for  $n = 12$

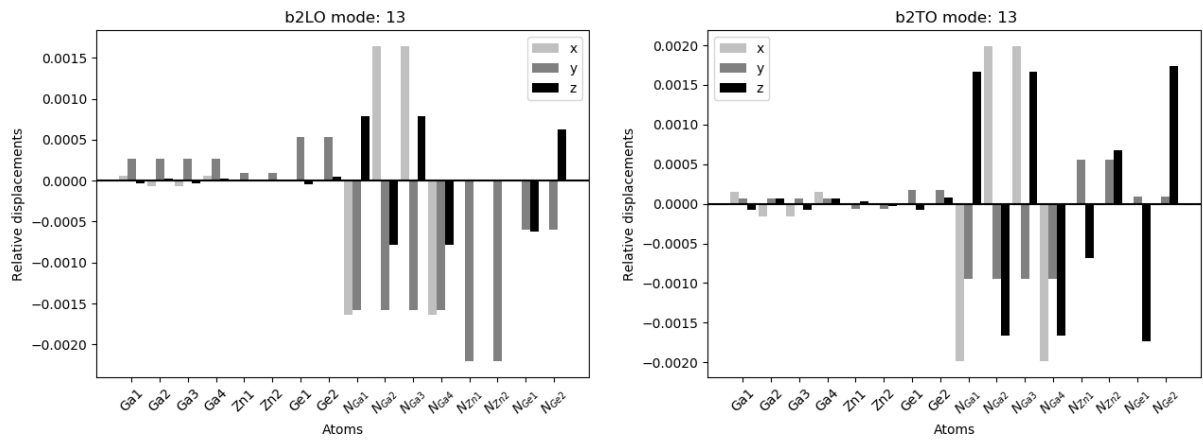


Figure A.36:  $b_2^n$  modes eigendisplacements (a) LO (b) TO for  $n = 13$

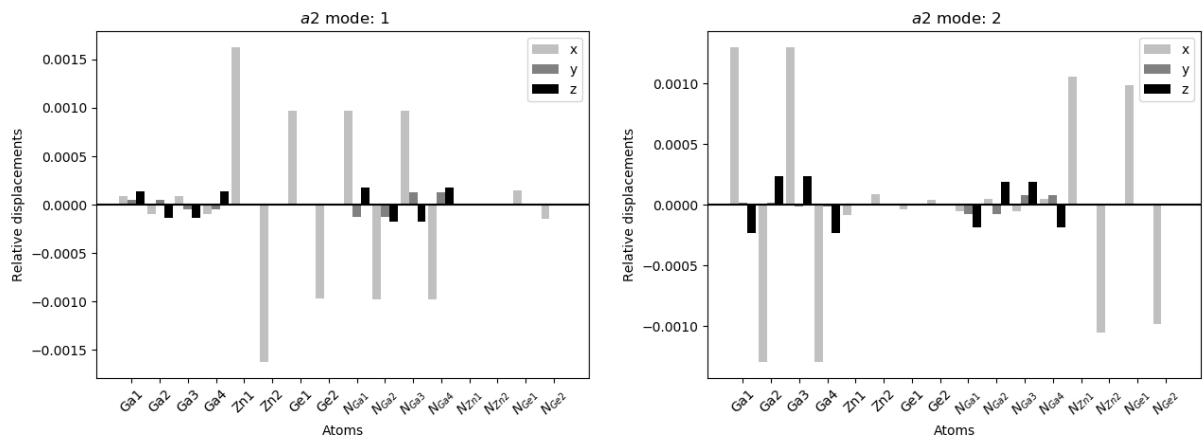


Figure A.37:  $a_2^n$  mode eigendisplacements for (a)  $n = 1$  (b)  $n = 2$

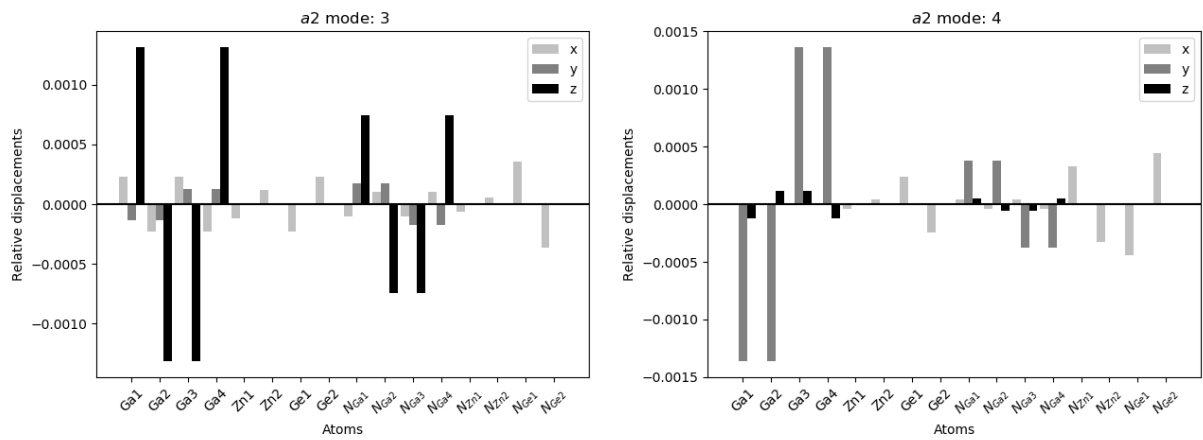


Figure A.38:  $a_2^n$  mode eigendisplacements for (a)  $n = 3$  (b)  $n = 4$

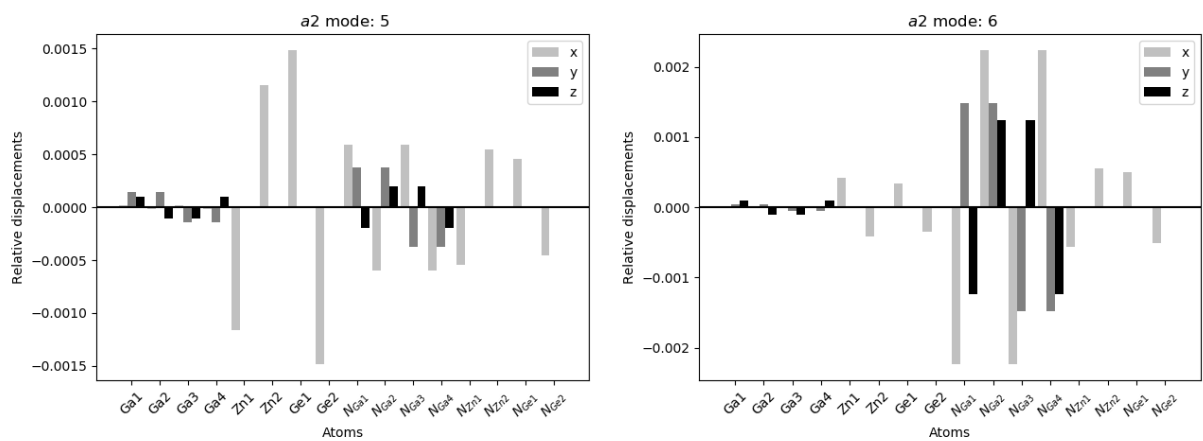


Figure A.39:  $a_2^n$  mode eigendisplacements for (a)  $n = 5$  (b)  $n = 6$

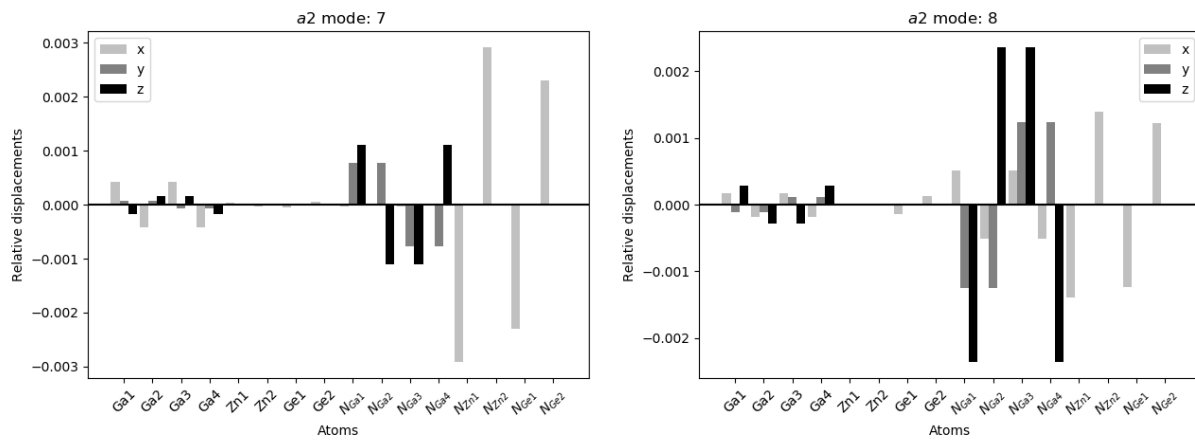


Figure A.40:  $a_2^n$  mode eigendisplacements for (a)  $n = 7$  (b)  $n = 8$

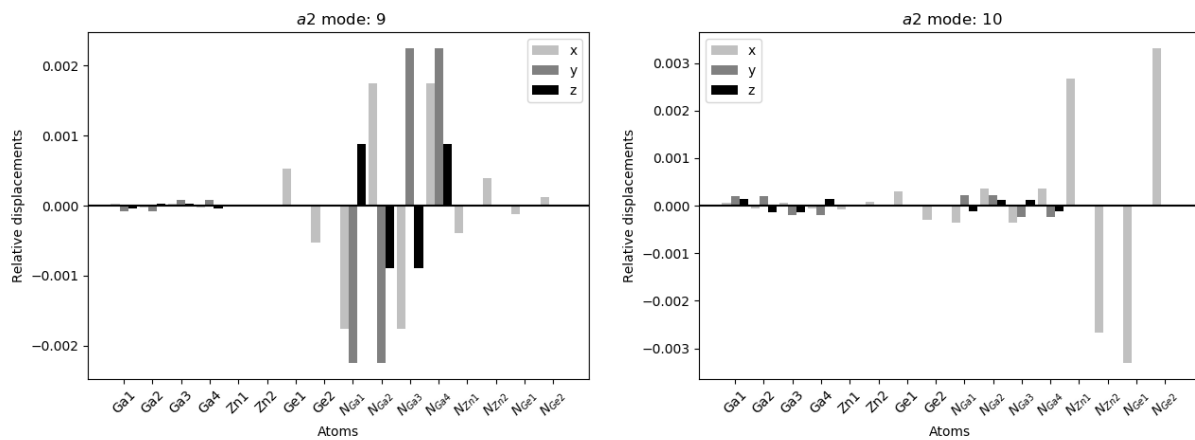


Figure A.41:  $a_2^n$  mode eigendisplacements (a)  $n = 9$  and (b)  $n = 10$ .

# Bibliography

- [1] M. Higashiwaki, K. Sasaki, A. Kuramata, T. Masui, S. Yamakoshi, Gallium oxide ( $\text{Ga}_2\text{O}_3$ ) metal-semiconductor field-effect transistors on single-crystal  $\beta$ - $\text{Ga}_2\text{O}_3$  (010) substrates, *Applied Physics Letters* 100 (1) (2012) 013504. arXiv:<https://doi.org/10.1063/1.3674287>, doi:10.1063/1.3674287.  
URL <https://doi.org/10.1063/1.3674287>
- [2] K. Ghosh, U. Singiseti, Ab initio velocity-field curves in monoclinic  $\beta$ - $\text{Ga}_2\text{O}_3$ , *Journal of Applied Physics* 122 (3) (2017) 035702. arXiv:<https://doi.org/10.1063/1.4986174>, doi:10.1063/1.4986174.  
URL <https://doi.org/10.1063/1.4986174>
- [3] P. H. Kang Y, Krishnaswamy K, V. de Walle CG, Fundamental limits on the electron mobility of  $\beta$ - $\text{Ga}_2\text{O}_3$ , *J Phys Condens Matter* 29 (23) (2017) 234001. doi:10.1088/1361-648X/aa6f66.
- [4] K. Ghosh, U. Singiseti, Electron mobility in monoclinic  $\beta$ - $\text{Ga}_2\text{O}_3$ ?Effect of plasmon-phonon coupling, anisotropy, and confinement, *Journal of Materials Research* 32 (22) (2017) 4142-4152. doi:10.1557/jmr.2017.398.
- [5] M. Lorenz, J. Woods, R. Gambino, Some electrical properties of the semiconductor  $\beta$ - $\text{Ga}_2\text{O}_3$ , *Journal of Physics and Chemistry of Solids* 28 (3) (1967) 403-404. doi:[https://doi.org/10.1016/0022-3697\(67\)90305-8](https://doi.org/10.1016/0022-3697(67)90305-8).

- URL <https://www.sciencedirect.com/science/article/pii/S0022369767903058>
- [6] T. Harwig, F. Kellendonk, Some observations on the photoluminescence of doped  $\beta$ -galliumsesquioxide, *J. Solid State Chem.* 24 (3) (1978) 255 – 263. doi:[http://dx.doi.org/10.1016/0022-4596\(78\)90017-8](http://dx.doi.org/10.1016/0022-4596(78)90017-8).
- URL <http://www.sciencedirect.com/science/article/pii/S0022459678900178>
- [7] J. B. Varley, J. R. Weber, A. Janotti, C. G. Van de Walle, Oxygen vacancies and donor impurities in  $\beta$ -Ga<sub>2</sub>O<sub>3</sub>, *Applied Physics Letters* 97 (14) (2010) 142106. arXiv:<https://doi.org/10.1063/1.3499306>, doi:10.1063/1.3499306.
- URL <https://doi.org/10.1063/1.3499306>
- [8] A. J. Green, K. D. Chabak, E. R. Heller, R. C. Fitch, M. Baldini, A. Fiedler, K. Irmischer, G. Wagner, Z. Galazka, S. E. Tetlak, A. Crespo, K. Leedy, G. H. Jessen, 3.8-MV/cm Breakdown Strength of MOVPE-Grown Sn-Doped  $\beta$ -Ga<sub>2</sub>O<sub>3</sub> MOSFETs, *IEEE Electron Device Letters* 37 (7) (2016) 902–905. doi:10.1109/LED.2016.2568139.
- [9] K. Sasaki, M. Higashiwaki, A. Kuramata, T. Masui, S. Yamakoshi, MBE grown Ga<sub>2</sub>O<sub>3</sub> and its power device applications, *J. Cryst. Growth* 378 (2013) 591 – 595, the 17th International Conference on Molecular Beam Epitaxy. doi:<http://dx.doi.org/10.1016/j.jcrysgr.2013.02.015>.
- URL <http://www.sciencedirect.com/science/article/pii/S0022024813001280>
- [10] H. Peelaers, C. G. Van de Walle, Brillouin zone and band structure of  $\beta$ -Ga<sub>2</sub>O<sub>3</sub>, *Phys. Status Solidi (b)* 252 (4) (2015) 828–832. doi:10.1002/pssb.201451551.
- URL <http://dx.doi.org/10.1002/pssb.201451551>

- 
- [11] M. Orita, H. Ohta, M. Hirano, H. Hosono, Deep-ultraviolet transparent conductive  $\beta$ -Ga<sub>2</sub>O<sub>3</sub> thin films, *Applied Physics Letters* 77 (25) (2000) 4166–4168. arXiv:<https://doi.org/10.1063/1.1330559>, doi:10.1063/1.1330559.  
URL <https://doi.org/10.1063/1.1330559>
- [12] S. Geller, Crystal Structure of  $\beta$ -Ga<sub>2</sub>O<sub>3</sub>, *J. Chem. Phys.* 33 (3) (1960) 676–684. arXiv:<http://dx.doi.org/10.1063/1.1731237>, doi:10.1063/1.1731237.  
URL <http://dx.doi.org/10.1063/1.1731237>
- [13] J. B. Varley, A. Janotti, C. Franchini, C. G. Van de Walle, Role of self-trapping in luminescence and *p*-type conductivity of wide-band-gap oxides, *Phys. Rev. B* 85 (2012) 081109. doi:10.1103/PhysRevB.85.081109.  
URL <http://link.aps.org/doi/10.1103/PhysRevB.85.081109>
- [14] Y. Frodason, K. Johansen, L. Vines, J. Varley, Self-trapped hole and impurity-related broad luminescence in  $\beta$ -Ga<sub>2</sub>O<sub>3</sub>, *Journal of Applied Physics* 127 (7) (2020) 075701. doi:10.1063/1.5140742.  
URL <https://doi.org/10.1063/1.5140742>
- [15] <https://www.vasp.at/> (2011).
- [16] J. Furthmüller, F. Bechstedt, Quasiparticle bands and spectra of Ga<sub>2</sub>O<sub>3</sub> polymorphs, *Phys. Rev. B* 93 (2016) 115204. doi:10.1103/PhysRevB.93.115204.  
URL <http://link.aps.org/doi/10.1103/PhysRevB.93.115204>
- [17] K. A. Mengle, G. Shi, D. Bayerl, E. Kioupakis, First-principles calculations of the near-edge optical properties of  $\beta$ -Ga<sub>2</sub>O<sub>3</sub>, *Appl. Phys. Lett.* 109 (21) (2016) 212104. arXiv:<http://dx.doi.org/10.1063/1.4968822>, doi:10.1063/1.4968822.  
URL <http://dx.doi.org/10.1063/1.4968822>
- [18] <https://www.quantum-espresso.org/> (2010).

- [19] T. Matsumoto, M. Aoki, A. Kinoshita, T. Aono, Absorption and Reflection of Vapor Grown Single Crystal Platelets of  $\beta$ -Ga<sub>2</sub>O<sub>3</sub>, Jap. J. Appl. Phys. 13 (10) (1974) 1578.  
URL <http://stacks.iop.org/1347-4065/13/i=10/a=1578>
- [20] W. R. L. Lambrecht, A. Punya, III-Nitride Semiconductors and their Modern Devices, in: B. Gill (Ed.), The Oxford Handbook of Innovation, Oxford University Press, Oxford, 2013, Ch. 15, pp. 519–585.
- [21] S. Lyu, D. Skachkov, K. Kash, E. W. Blanton, W. R. L. Lambrecht, Band Gaps, Band-Offsets, Disorder, Stability Region, and Point Defects in II-IV-N<sub>2</sub> Semiconductors, physica status solidi (a) 216 (15) (2019) 1800875. arXiv: <https://onlinelibrary.wiley.com/doi/pdf/10.1002/pssa.201800875>, doi:<https://doi.org/10.1002/pssa.201800875>.  
URL <https://onlinelibrary.wiley.com/doi/abs/10.1002/pssa.201800875>
- [22] A. D. Martinez, A. N. Fioretti, E. S. Toberer, A. C. Tamboli, Synthesis, structure, and optoelectronic properties of II-IV-V<sub>2</sub> materials, J. Mater. Chem. A 5 (2017) 11418–11435. doi:[10.1039/C7TA00406K](https://doi.org/10.1039/C7TA00406K).  
URL <http://dx.doi.org/10.1039/C7TA00406K>
- [23] A. Punya, W. R. L. Lambrecht, Band offsets between ZnGeN<sub>2</sub>, GaN, ZnO, and ZnSnN<sub>2</sub> and their potential impact for solar cells, Phys. Rev. B 88 (2013) 075302. doi:[10.1103/PhysRevB.88.075302](https://doi.org/10.1103/PhysRevB.88.075302).  
URL <https://link.aps.org/doi/10.1103/PhysRevB.88.075302>
- [24] A. P. Jaroenjittichai, S. Lyu, W. R. L. Lambrecht, Erratum: Band offsets between ZnGeN<sub>2</sub>, GaN, ZnO, and ZnSnN<sub>2</sub> and their potential impact for solar cells [Phys. Rev. B 88, 075302 (2013)], Phys. Rev. B 96 (2017) 079907.

- doi:10.1103/PhysRevB.96.079907.  
URL <https://link.aps.org/doi/10.1103/PhysRevB.96.079907>
- [25] B. H. D. Jayatunga, S. Lyu, S. K. Radha, K. Kash, W. R. L. Lambrecht, Ordering in the mixed ZnGeN<sub>2</sub>-GaN alloy system: Crystal structures and band structures of ZnGeGa<sub>2</sub>N<sub>4</sub> from first principles, *Phys. Rev. Materials* 2 (2018) 114602. doi:10.1103/PhysRevMaterials.2.114602.  
URL <https://link.aps.org/doi/10.1103/PhysRevMaterials.2.114602>
- [26] T. Suehiro, M. Tansho, T. Shimizu, Quaternary Wurtzitic Nitrides in the System ZnGeN<sub>2</sub>-GaN: Powder Synthesis, Characterization, and Potentiality as a Photocatalyst, *The Journal of Physical Chemistry C* 121 (49) (2017) 27590–27596. doi:10.1021/acs.jpcc.7b09135.  
URL <https://doi.org/10.1021/acs.jpcc.7b09135>
- [27] B. H. D. Jayatunga, M. R. Karim, R. A. Lalk, O. Ohanaka, W. R. L. Lambrecht, H. Zhao, K. Kash, Metal-Organic Chemical Vapor Deposition of ZnGeGa<sub>2</sub>N<sub>4</sub>, *Crystal Growth & Design* 20 (1) (2019) 189. arXiv:<https://doi.org/10.1021/acs.cgd.9b00995>, doi:10.1021/acs.cgd.9b00995.  
URL <https://doi.org/10.1021/acs.cgd.9b00995>
- [28] L. Seguin, M. Figlarz, R. Cavagnat, J.-C. Lassgues, Infrared and Raman spectra of MoO<sub>3</sub> molybdenum trioxides and MoO<sub>3</sub> · xH<sub>2</sub>O molybdenum trioxide hydrates, *Spectrochimica Acta Part A: Molecular and Biomolecular Spectroscopy* 51 (8) (1995) 1323 – 1344. doi:[https://doi.org/10.1016/0584-8539\(94\)00247-9](https://doi.org/10.1016/0584-8539(94)00247-9).  
URL <http://www.sciencedirect.com/science/article/pii/S0584853994002479>
- [29] M.B. Rahmani and S.H. Keshmiri and J. Yu and A.Z. Sadek and L. Al-

- Mashat and A. Moafi and K. Latham and Y.X. Li and W. Wlodarski and K. Kalantar-zadeh, Gas sensing properties of thermally evaporated lamellar MoO<sub>3</sub>, *Sensors and Actuators B: Chemical* 145 (1) (2010) 13 – 19. doi:<https://doi.org/10.1016/j.snb.2009.11.007>.  
URL <http://www.sciencedirect.com/science/article/pii/S0925400509008727>
- [30] S. Balendhran, S. Walia, M. Alsaif, E. P. Nguyen, J. Z. Ou, S. Zhuiykov, S. Sriram, M. Bhaskaran, K. Kalantar-zadeh, Field Effect Biosensing Platform Based on 2D  $\alpha$ -MoO<sub>3</sub>, *ACS Nano* 7 (11) (2013) 9753–9760. doi:[10.1021/nn403241f](https://doi.org/10.1021/nn403241f).  
URL <https://doi.org/10.1021/nn403241f>
- [31] Y. Li, D. Wang, Q. An, B. Ren, Y. Rong, Y. Yao, Flexible electrode for long-life rechargeable sodium-ion batteries: effect of oxygen vacancy in MoO<sub>3-x</sub>, *J. Mater. Chem. A* 4 (2016) 5402–5405. doi:[10.1039/C6TA01342B](https://doi.org/10.1039/C6TA01342B).  
URL <http://dx.doi.org/10.1039/C6TA01342B>
- [32] D. Voiry, M. Salehi, R. Silva, T. Fujita, M. Chen, T. Asefa, V. B. Shenoy, G. Eda, M. Chhowalla, Conducting MoS<sub>2</sub> Nanosheets as Catalysts for Hydrogen Evolution Reaction, *Nano Letters* 13 (12) (2013) 6222–6227. doi:[10.1021/nl403661s](https://doi.org/10.1021/nl403661s).  
URL <https://doi.org/10.1021/nl403661s>
- [33] M. Kröger, S. Hamwi, J. Meyer, T. Riedl, W. Kowalsky, A. Kahn, Role of the deep-lying electronic states of MoO<sub>3</sub> in the enhancement of hole-injection in organic thin films, *Applied Physics Letters* 95 (12) (2009) 123301. doi:[10.1063/1.3231928](https://doi.org/10.1063/1.3231928).  
URL <https://doi.org/10.1063/1.3231928>
- [34] B. Holler, X. P. Gao, private communication (2020).

- [35] S. Balendhran, J. Deng, J. Z. Ou, S. Walia, J. Scott, J. Tang, K. L. Wang, M. R. Field, S. Russo, S. Zhuiykov, M. S. Strano, N. Medhekar, S. Sriram, M. Bhaskaran, K. Kalantar-zadeh, Enhanced Charge Carrier Mobility in Two-Dimensional High Dielectric Molybdenum Oxide, *Advanced Materials* 25 (1) (2013) 109–114. doi:10.1002/adma.201203346.  
URL <https://onlinelibrary.wiley.com/doi/abs/10.1002/adma.201203346>
- [36] G. Mestl, P. Ruiz, B. Delmon, H. Knozinger, Oxygen-Exchange Properties of MoO<sub>3</sub>: An in situ Raman Spectroscopy Study, *The Journal of Physical Chemistry* 98 (44) (1994) 11269–11275. doi:10.1021/j100095a007.  
URL <https://doi.org/10.1021/j100095a007>
- [37] M. Py, K. Maschke, Intra- and interlayer contributions to the lattice vibrations in MoO<sub>3</sub>, *Physica B+C* 105 (1) (1981) 370 – 374. doi:[https://doi.org/10.1016/0378-4363\(81\)90278-3](https://doi.org/10.1016/0378-4363(81)90278-3).  
URL <http://www.sciencedirect.com/science/article/pii/0378436381902783>
- [38] K. Eda, Longitudinal-transverse splitting effects in IR absorption spectra of MoO<sub>3</sub>, *Journal of Solid State Chemistry* 95 (1) (1991) 64 – 73. doi:[https://doi.org/10.1016/0022-4596\(91\)90376-S](https://doi.org/10.1016/0022-4596(91)90376-S).  
URL <http://www.sciencedirect.com/science/article/pii/002245969190376S>
- [39] X. Gonze, J. M. Beuken, R. Caracas, F. Detraux, M. Fuchs, G. M. Rignanese, L. Sindic, M. Verstraete, G. Zerah, F. Jollet, First-principles computation of material properties: the ABINIT software project, *Computational Materials Science* 25,3 (2002/11) 478–492.  
URL <http://www.abinit.org>

- 
- [40] P. Hohenberg, W. Kohn, Inhomogeneous Electron Gas, *Phys. Rev.* 136 (3B) (1964) B864–B871. doi:10.1103/PhysRev.136.B864.
- [41] R. M. Martin, *Electronic Structure: Basic Theory and Practical Methods*, Cambridge University Press, 2004. doi:10.1017/CB09780511805769.
- [42] W. Kohn, L. J. Sham, Self-consistent equations including exchange and correlation effects, *Phys. Rev.* 140 (4A) (1965) A1133–A1138. doi:10.1103/PhysRev.140.A1133.
- [43] M. Methfessel, M. van Schilfhaarde, R. A. Casali, A Full-Potential LMTO Method Based on Smooth Hankel Functions, in: H. Dreysse (Ed.), *Electronic Structure and Physical Properties of Solids. The Use of the LMTO Method*, Vol. 535 of *Lecture Notes in Physics*, Berlin Springer Verlag, 2000, p. 114.
- [44] T. Kotani, M. van Schilfhaarde, Fusion of the LAPW and LMTO methods: The augmented plane wave plus muffin-tin orbital method, *Phys. Rev. B* 81 (12) (2010) 125117. doi:10.1103/PhysRevB.81.125117.
- [45] M. van Schilfhaarde, T. Kotani, S. V. Faleev, Adequacy of approximations in *GW* theory, *Phys. Rev. B* 74 (24) (2006) 245125. doi:10.1103/PhysRevB.74.245125. URL <http://link.aps.org/abstract/PRB/v74/e245125>
- [46] T. Kotani, M. van Schilfhaarde, S. V. Faleev, Quasiparticle self-consistent *GW* method: A basis for the independent-particle approximation, *Phys. Rev. B* 76 (16) (2007) 165106. doi:10.1103/PhysRevB.76.165106. URL <http://link.aps.org/abstract/PRB/v76/e165106>
- [47] M. van Schilfhaarde, T. Kotani, S. Faleev, Quasiparticle Self-Consistent *GW* Theory, *Phys. Rev. Lett.* 96 (22) (2006) 226402. doi:10.1103/PhysRevLett.96.226402.

- [48] L. Hedin, New Method for Calculating the One-Particle Green's Function with Application to the Electron-Gas Problem, *Phys. Rev.* 139 (3A) (1965) A796–A823. doi:10.1103/PhysRev.139.A796.
- [49] L. Hedin, S. Lundqvist, Effects of Electron-Electron and Electron-Phonon Interactions on the One-Electron States of Solids, in: F. Seitz, D. Turnbull, H. Ehrenreich (Eds.), *Solid State Physics, Advanced in Research and Applications*, Vol. 23, Academic Press, New York, 1969, pp. 1–181.
- [50] <https://www.questaal.org/> (2007).
- [51] B. Cunningham, M. Grüning, P. Azarhoosh, D. Pashov, M. van Schilfgaarde, Effect of ladder diagrams on optical absorption spectra in a quasiparticle self-consistent *GW* framework, *Phys. Rev. Materials* 2 (2018) 034603. doi:10.1103/PhysRevMaterials.2.034603.  
URL <https://link.aps.org/doi/10.1103/PhysRevMaterials.2.034603>
- [52] A. N. Chantis, M. van Schilfgaarde, T. Kotani, Ab Initio Prediction of Conduction Band Spin Splitting in Zinc Blende Semiconductors, *Phys. Rev. Lett.* 96 (2006) 086405. doi:10.1103/PhysRevLett.96.086405.  
URL <https://link.aps.org/doi/10.1103/PhysRevLett.96.086405>
- [53] A. N. Chantis, M. Cardona, N. E. Christensen, D. L. Smith, M. van Schilfgaarde, T. Kotani, A. Svane, R. C. Albers, Strain-induced conduction-band spin splitting in GaAs from first-principles calculations, *Phys. Rev. B* 78 (2008) 075208. doi:10.1103/PhysRevB.78.075208.  
URL <https://link.aps.org/doi/10.1103/PhysRevB.78.075208>
- [54] D. Deguchi, K. Sato, H. Kino, T. Kotani, Accurate energy bands calculated by the hybrid quasiparticle self-consistent *GW* method implemented in the *ecalj* package, *Japanese Journal of Applied Physics* 55 (5) (2016) 051201. doi:10.

- 7567/jjap.55.051201.  
URL <https://doi.org/10.7567/jjap.55.051201>
- [55] C. Bhandari, M. van Schilfgaarde, T. Kotani, W. R. L. Lambrecht, All-electron quasiparticle self-consistent *GW* band structures for SrTiO<sub>3</sub> including lattice polarization corrections in different phases, *Phys. Rev. Materials* 2 (2018) 013807. doi:10.1103/PhysRevMaterials.2.013807.  
URL <https://link.aps.org/doi/10.1103/PhysRevMaterials.2.013807>
- [56] M. Shishkin, M. Marsman, G. Kresse, Accurate Quasiparticle Spectra from Self-Consistent *GW* Calculations with Vertex Corrections, *Phys. Rev. Lett.* 99 (2007) 246403. doi:10.1103/PhysRevLett.99.246403.  
URL <https://link.aps.org/doi/10.1103/PhysRevLett.99.246403>
- [57] W. Chen, A. Pasquarello, Accurate band gaps of extended systems via efficient vertex corrections in *GW*, *Phys. Rev. B* 92 (2015) 041115. doi:10.1103/PhysRevB.92.041115.  
URL <https://link.aps.org/doi/10.1103/PhysRevB.92.041115>
- [58] S. Baroni, P. Giannozzi, A. Testa, Green's-function approach to linear response in solids, *Phys. Rev. Lett.* 58 (1987) 1861–1864. doi:10.1103/PhysRevLett.58.1861.  
URL <https://link.aps.org/doi/10.1103/PhysRevLett.58.1861>
- [59] X. Gonze, First-principles responses of solids to atomic displacements and homogeneous electric fields: Implementation of a conjugate-gradient algorithm, *Phys. Rev. B* 55 (16) (1997) 10337–10354. doi:10.1103/PhysRevB.55.10337.
- [60] X. Gonze, C. Lee, Dynamical matrices, born effective charges, dielectric permittivity tensors, and interatomic force constants from density-functional perturba-

- tion theory, Phys. Rev. B 55 (16) (1997) 10355–10368. doi:10.1103/PhysRevB.55.10355.
- [61] M. Veithen, X. Gonze, P. Ghosez, Nonlinear optical susceptibilities, Raman efficiencies, and electro-optic tensors from first-principles density functional perturbation theory, Phys. Rev. B 71 (12) (2005) 125107. doi:10.1103/PhysRevB.71.125107.
- [62] P. Gopalan, S. Knight, A. Chanana, M. Stokey, P. Ranga, M. A. Scarpulla, S. Krishnamoorthy, V. Darakchieva, Z. Galazka, K. Irmscher, A. Fiedler, S. Blair, M. Schubert, B. Sensale-Rodriguez, The anisotropic quasi-static permittivity of single-crystal  $\beta$ -Ga<sub>2</sub>O<sub>3</sub> measured by terahertz spectroscopy, Applied Physics Letters 117 (25) (2020) 252103. arXiv:<https://doi.org/10.1063/5.0031464>, doi:10.1063/5.0031464.  
URL <https://doi.org/10.1063/5.0031464>
- [63] R. Korlacki, M. Stokey, A. Mock, S. Knight, A. Papamichail, V. Darakchieva, M. Schubert, Strain and stress relationships for optical phonon modes in monoclinic crystals with  $\beta$ -Ga<sub>2</sub>O<sub>3</sub> as an example, Phys. Rev. B 102 (2020) 180101. doi:10.1103/PhysRevB.102.180101.  
URL <https://link.aps.org/doi/10.1103/PhysRevB.102.180101>
- [64] F. K. Urban, D. Barton, M. Schubert, Numerical ellipsometry: Methods for selecting measurements and techniques for advanced analysis applied to  $\beta$ -Ga<sub>2</sub>O<sub>3</sub>, Journal of Vacuum Science & Technology A 38 (2) (2020) 023406. arXiv:<https://doi.org/10.1116/1.5134790>, doi:10.1116/1.5134790.  
URL <https://doi.org/10.1116/1.5134790>
- [65] S. Botti, M. A. L. Marques, Strong Renormalization of the Electronic Band Gap due to Lattice Polarization in the *GW* Formalism, Phys. Rev. Lett. 110 (2013)

226404. doi:10.1103/PhysRevLett.110.226404.  
URL <http://link.aps.org/doi/10.1103/PhysRevLett.110.226404>
- [66] W. R. L. Lambrecht, C. Bhandari, M. van Schilfgaarde, Lattice polarization effects on the screened Coulomb interaction  $W$  of the  $GW$  approximation, Phys. Rev. Materials 1 (2017) 043802. doi:10.1103/PhysRevMaterials.1.043802.  
URL <https://link.aps.org/doi/10.1103/PhysRevMaterials.1.043802>
- [67] T. Kotani, Quasiparticle self-consistent gw method based on the augmented plane-wave and muffin-tin orbital method, J. Phys. Soc. Japan 83 (9) (2014) 094711. arXiv:<http://dx.doi.org/10.7566/JPSJ.83.094711>, doi:10.7566/JPSJ.83.094711.  
URL <http://dx.doi.org/10.7566/JPSJ.83.094711>
- [68] C. Friedrich, S. Blügel, A. Schindlmayr, Efficient implementation of the  $GW$  approximation within the all-electron FLAPW method, Phys. Rev. B 81 (2010) 125102. doi:10.1103/PhysRevB.81.125102.  
URL <http://link.aps.org/doi/10.1103/PhysRevB.81.125102>
- [69] B. Liu, M. Gu, X. Liu, Lattice dynamical, dielectric, and thermodynamic properties of  $\beta$ -Ga<sub>2</sub>O<sub>3</sub> from first principles, Appl. Phys. Lett. 91 (17) (2007) 172102. arXiv:<http://aip.scitation.org/doi/pdf/10.1063/1.2800792>, doi:10.1063/1.2800792.  
URL <http://aip.scitation.org/doi/abs/10.1063/1.2800792>
- [70] D. Singh, Ground-state properties of lanthanum: Treatment of extended-core states, Phys. Rev. B 43 (1991) 6388–6392. doi:10.1103/PhysRevB.43.6388.  
URL <http://link.aps.org/doi/10.1103/PhysRevB.43.6388>
- [71] G. Antonius, S. Poncé, E. Lantagne-Hurtubise, G. Auclair, X. Gonze, M. Côté, Dynamical and anharmonic effects on the electron-phonon coupling and the zero-

- point renormalization of the electronic structure, Phys. Rev. B 92 (2015) 085137. doi:10.1103/PhysRevB.92.085137.  
URL <http://link.aps.org/doi/10.1103/PhysRevB.92.085137>
- [72] A. Marini, S. Ponc e, X. Gonze, Many-body perturbation theory approach to the electron-phonon interaction with density-functional theory as a starting point, Phys. Rev. B 91 (2015) 224310. doi:10.1103/PhysRevB.91.224310.  
URL <http://link.aps.org/doi/10.1103/PhysRevB.91.224310>
- [73] M. Cardona, M. L. W. Thewalt, Isotope effects on the optical spectra of semiconductors, Rev. Mod. Phys. 77 (4) (2005) 1173–1224. doi:10.1103/RevModPhys.77.1173.
- [74] A. Ratnaparkhe, W. R. L. Lambrecht, Quasiparticle self-consistent GW band structure of  $\beta$ -Ga<sub>2</sub>O<sub>3</sub> and the anisotropy of the absorption onset, Applied Physics Letters 110 (13) (2017) 132103. arXiv:<http://dx.doi.org/10.1063/1.4978668>, doi:10.1063/1.4978668.  
URL <http://dx.doi.org/10.1063/1.4978668>
- [75] S. L. Adler, Quantum theory of the dielectric constant in real solids, Phys. Rev. 126 (1962) 413–420. doi:10.1103/PhysRev.126.413.  
URL <http://link.aps.org/doi/10.1103/PhysRev.126.413>
- [76] N. Wiser, Dielectric constant with local field effects included, Phys. Rev. 129 (1963) 62–69. doi:10.1103/PhysRev.129.62.  
URL <http://link.aps.org/doi/10.1103/PhysRev.129.62>
- [77] C. Bhandari, W. R. L. Lambrecht, M. van Schilfgaarde, Quasiparticle self-consistent GW calculations of the electronic band structure of bulk and monolayer V<sub>2</sub>O<sub>5</sub>, Phys. Rev. B 91 (2015) 125116. doi:10.1103/PhysRevB.91.125116.  
URL <https://link.aps.org/doi/10.1103/PhysRevB.91.125116>

- [78] J. B. Varley, A. Schleife, BetheSalpeter calculation of optical-absorption spectra of  $\text{In}_2\text{O}_3$  and  $\text{Ga}_2\text{O}_3$ , *Semiconductor Science and Technology* 30 (2) (2015) 024010.  
URL <http://stacks.iop.org/0268-1242/30/i=2/a=024010>
- [79] H. Peelaers, J. B. Varley, J. S. Speck, C. G. Van de Walle, Structural and electronic properties of  $\text{Ga}_2\text{O}_3\text{-Al}_2\text{O}_3$  alloys, *Applied Physics Letters* 112 (24) (2018) 242101. arXiv:<https://doi.org/10.1063/1.5036991>, doi:10.1063/1.5036991.  
URL <https://doi.org/10.1063/1.5036991>
- [80] J. Heyd, G. E. Scuseria, M. Ernzerhof, Hybrid functionals based on a screened coulomb potential, *J. Chem. Phys.* 118 (18) (2003) 8207–8215. doi:10.1063/1.1564060.  
URL <http://link.aip.org/link/?JCP/118/8207/1>
- [81] J. Heyd, G. E. Scuseria, M. Ernzerhof, Erratum: “Hybrid functionals based on a screened Coulomb potential” [*J. Chem. Phys.* [bold 118], 8207 (2003)], *J. Chem. Phys.* 124 (21) (2006) 219906. doi:10.1063/1.2204597.  
URL <http://link.aip.org/link/?JCP/124/219906/1>
- [82] C. Hartwigsen, S. Goedecker, J. Hutter, Relativistic separable dual-space Gaussian pseudopotentials from H to Rn, *Phys. Rev. B* 58 (1998) 3641–3662. doi:10.1103/PhysRevB.58.3641.  
URL <http://link.aps.org/doi/10.1103/PhysRevB.58.3641>
- [83] A. Zunger, S.-H. Wei, L. G. Ferreira, J. E. Bernard, Special quasirandom structures, *Phys. Rev. Lett.* 65 (1990) 353–356. doi:10.1103/PhysRevLett.65.353.  
URL <https://link.aps.org/doi/10.1103/PhysRevLett.65.353>
- [84] I. P. Batra, Electronic structure of  $\alpha\text{-Al}_2\text{O}_3$ , *Journal of Physics C: Solid State*

- Physics 15 (26) (1982) 5399–5410. doi:10.1088/0022-3719/15/26/019.  
URL <https://doi.org/10.1088/0022-3719/15/26/019>
- [85] L. He, F. Liu, G. Hautier, M. J. T. Oliveira, M. A. L. Marques, F. D. Vila, J. J. Rehr, G.-M. Rignanese, A. Zhou, Accuracy of generalized gradient approximation functionals for density-functional perturbation theory calculations, Phys. Rev. B 89 (2014) 064305. doi:10.1103/PhysRevB.89.064305.  
URL <https://link.aps.org/doi/10.1103/PhysRevB.89.064305>
- [86] J. P. Perdew, K. Burke, M. Ernzerhof, Generalized Gradient Approximation Made Simple, Phys. Rev. Lett. 77 (18) (1996) 3865–3868. doi:10.1103/PhysRevLett.77.3865.
- [87] D. M. Ceperley, B. J. Alder, Ground State of the Electron Gas by a Stochastic Method, Phys. Rev. Lett. 45 (1980) 566–569. doi:10.1103/PhysRevLett.45.566.  
URL <http://link.aps.org/doi/10.1103/PhysRevLett.45.566>
- [88] M. Schubert, A. Mock, R. Korlacki, V. Darakchieva, Phonon order and reststrahlen bands of polar vibrations in crystals with monoclinic symmetry, Phys. Rev. B 99 (2019) 041201. doi:10.1103/PhysRevB.99.041201.  
URL <https://link.aps.org/doi/10.1103/PhysRevB.99.041201>
- [89] S. Lyu, Y. Liu, W. R. L. Lambrecht, First-principles calculations of phonon derived Raman and infrared spectra in Be-IV-N2 compounds, Journal of Physics D: Applied Physics 52 (38) (2019) 385106. doi:10.1088/1361-6463/ab2c90.  
URL <https://doi.org/10.1088/1361-6463/ab2c90>
- [90] <https://materialsproject.org/>, doi:10.1038/sdata.2018.65 (2011). doi:{10.1038/sdata.2018.65}.

- [91] E. W. Blanton, K. He, J. Shan, K. Kash, Characterization and control of ZnGeN<sub>2</sub> cation lattice ordering, *Journal of Crystal Growth* 461 (2017) 38 – 45.  
doi:<https://doi.org/10.1016/j.jcrysgr.2017.01.008>.  
URL <http://www.sciencedirect.com/science/article/pii/S0022024817300088>
- [92] P. C. Quayle, E. W. Blanton, A. Punya, G. T. Junno, K. He, L. Han, H. Zhao, J. Shan, W. R. L. Lambrecht, K. Kash, Charge-neutral disorder and polytypes in heterovalent wurtzite-based ternary semiconductors: The importance of the octet rule, *Phys. Rev. B* 91 (2015) 205207. doi:10.1103/PhysRevB.91.205207.  
URL <http://link.aps.org/doi/10.1103/PhysRevB.91.205207>
- [93] T. J. Peshek, T. R. Paudel, K. Kash, W. R. L. Lambrecht, Vibrational modes in ZnGeN<sub>2</sub>: Raman study and theory, *Phys. Rev. B* 77 (23) (2008) 235213.  
doi:10.1103/PhysRevB.77.235213.  
URL <http://link.aps.org/abstract/PRB/v77/e235213>